Scanning Tunneling and Atomic Force Microscopy of Molecular Switches

Dissertation

zur Erlangung des Doktorgrades der
Mathematisch-Naturwissenschaftlichen Fakultät der
Christian-Albrechts-Universität zu Kiel

vorgelegt von

Katharina Scheil

Kiel, 2017

Erster Gutachter:	Prof. Dr. Richard Berndt
Zweiter Gutachter:	Prof. Dr. Olaf Magnussen
Tag der mündlichen Prüfung:	16.01.2018
Zum Druck genehmigt:	16.01.2018

gez. Prof. Dr. Natascha Oppelt, Dekanin

Hiermit erkläre ich an Eides statt, diese Arbeit selbstständig unter der Beratung meiner wissenschaftlichen Lehrer angefertigt und keine weiteren Hilfsmittel, außer den im Text angegebenen sowie den bekannten Nachschlagewerken der Naturwissenschaften, verwendet zu haben. Diese Arbeit wurde weder ganz noch in Teilen an anderer Stelle im Rahmen eines Prüfungsverfahrens vorgelegt. Frühere Promotionsversuche wurden von mir nicht vorgenommen. Die Arbeit ist unter Einhaltung der Regeln guter wissenschafticher Praxis der Deutschen Forschungsgemeinschaft entstanden.

Folgende Teile der Arbeit wurden in wissenschaftlichen Fachzeitschriften veröffentlicht:

- Kapitel 3:
  Katharina Scheil, Thiruvancheril G. Gopakumar, Julia Bahrenburg, Friedrich Temps, Reinhard J. Maurer, Karsten Reuter and Richard Berndt,
  Switching of an Azobenzene-Tripod Molecule on Ag(111),
  J. Phys. Chem. Lett. **7**, 2080 (2016)

- Kapitel 4:
  Katharina Scheil, Nicolás Lorente, Marie-Laure Bocquet, Pascal C. Hess, Marcel Mayor and Richard Berndt,
  Adatom Coadsorption with Three-Dimensional Cyclophanes on Ag(111),
  J. Phys. Chem. C. **121**, 25303 (2017)

Katharina Scheil

Abstract

This thesis revolves around the investigation of molecules adsorbed on metallic surfaces using combined low temperature scanning tunneling microscopy (STM) and atomic force microscopy (AFM). The focus is on three studies addressing switching and adsorption phenomena as well as acting forces in molecular junctions:

Tris-[4-(phenylazo)-phenyl]-amine (TPAPA) molecules, composed of three azobenzene subunits, are investigated on a Ag(111) surface. Despite expectation for azobenzene containing molecules on Ag(111), surprisingly, switching of TPAPA is feasible. Controlled switching of the azobenzene subunits between two states can selectively and reversibly be achieved by injecting electrons in the azo bridges. Passing current through the center of a TPAPA molecule induces switching processes in the three azobenzene subunits. It is shown that the switching process is no *trans–cis* isomerisation but rather a reorientation of the N–N bond of an azobenzene unit using STM and AFM at sub-molecular resolution along with scanning tunneling spectroscopy (STS) and density functional theory (DFT) calculations. The reorientation proceeds through a twisting motion of the azo-bridge that leads to a lateral shift of a phenyl ring.

Two closely related cyclophane molecules with a three-dimensional double-decker structure are studied on a Ag(111) surface. Both molecules are designed to attach to the surface with a naphthalene diimide (NDI) subunit while either a stilbene or an azobenzene moiety is exposed to the vacuum. A striking change in corrugation and apparent height of STM images is observed at moderate bias voltages. Oval protrusions dominate the topographs at elevated voltage, but are absent at lower voltage in favor of features with submolecular dimensions. The submolecular structures are assigned to reflect the molecule's position by analyzing occasional defects in the islands using STM and AFM. Calculations suggest that the oval protrusions are due to the presence of two intermolecular Ag adatoms and their electronic state.

Force spectroscopy is performed on iron tetraphenylporphyrin molecules with and without an axial Cl ligands (FeTPPCl and FeTPP) on Au(111). The transfer of the Cl ligand between FeTPPCl molecules and the tip of the AFM is used to systematically change the charge configuration in the junction. The maximal forces and the curve shapes considerably depend on the position and number of charged ligands in the tip–molecule junction. A point charge model reproduces the essential features of the force curves. A non-monotonous variation of the force with two Cl ions in the junction is explained by a tilting of the Cl ion at the tip at sufficient small distances. It is shown that Cl ligand transfers between molecules and the tip occur at application of adequate forces.

Zusammenfassung

Die vorliegende Dissertation beschäftigt sich mit Molekülen auf Metalloberflächen, welche mittels kombinierter Rastertunnelmikroskopie (STM) und Rasterkraftmikroskopie (AFM) erforscht wurden. Drei Molekülsysteme wurden in Hinblick auf Schaltbarkeit und des zugrundeliegenden Schaltmechanismus, Adsorbtionsphänomene sowie dem Auftreten von Kräften zwischen Molekülen und der AFM Spitze untersucht:

Tris-[4-(phenylazo)-phenyl]-amin (TPAPA) Moleküle, aufgebaut aus drei Azobenzol Einheiten, werden auf Ag(111) Oberflächen untersucht. Entgegen der Erwartung für auf Azobenzol basierenden Molekülen auf Ag(111) lässt sich TPAPA schalten. Die Azobenzol Einheiten lassen sich kontrolliert und reversibel zwischen zwei Zuständen schalten, indem Elektronen in die Azobrücke injiziert werden. Stromfluss durch das Molekülzentrum führt zu Schaltvorgängen in allen drei Azobenzol Einheiten. Mit Hilfe von STM, AFM, Rastertunnelspektroskopie (STS) und Dichtefunktionaltheorie (DFT) Rechnungen wird gezeigt, dass es sich bei dem Schaltprozess nicht um eine *trans-cis* Isomerisierung, sondern vielmehr um eine Neuorientierung der N-N Bindung der Azobenzol Einheiten handelt. Die Neuorientierung geschieht durch eine Verdrillung der Azobrücke, die zu einer lateralen Verschiebung eines Phenylrings führt.

Zwei Cyclophan Moleküle mit dreidimensionaler Doppeldecker Struktur werden auf Ag(111) Oberflächen untersucht. Beide Moleküle wurden entwickelt um mit einer Naphthalin Diimid (NDI) Plattform an der Oberfläche zu adsorbieren während entweder Azobenzol oder Stilben als funktionelle Einheit der Vakuumseite zugewandt ist. STM Bilder weisen eine markante Änderung im Profil der scheinbaren Höhe auf, die bei moderaten Spannungen auftritt. Während bei niedrigen Spannungen submolekulare Strukturen auftreten, werden die STM Bilder bei höheren Spannungen von ovalen Erhebungen dominiert. Untersuchungen von gelegentlich auftretenden Defekten in der Inselstruktur ergeben, dass die submolekularen Strukturen die Molekülpositionen markieren. Rechnungen zeigen, dass die starken Erhöhungen durch zwei Silberatome, die sich zwischen benachbarten Molekülen befinden, und deren elektronischen Zustand zustande kommen.

An Eisen Tetraphenylporphyrin Molekülen mit und ohne axialen Cl Liganden auf Au(111) wird Kraftspektroskopie durchgeführt. Der Transfer von geladenen Cl Liganden zwischen Molekülen und der Spitze des AFM wird genutzt, um die Ladungsanordnung in der Messstrecke systematisch zu verändern. Die maximale attraktive Kraft sowie die Kurvenform hängen entschieden von der Anzahl und Position geladener Cl Liganden in der Messstrecke ab. Die charakteristischen Merkmale der Kraftkurven werden durch ein Punktladungsmodell reproduziert. Eine nicht monotone Variation der Kraftkurve, die mit zwei Cl Ionen in der Messstrecke auftritt, wird auf eine Seitwertsneigung des Cl Ions an der Spitze zurückgeführt. Es wird gezeigt, dass der Transfer von Cl Liganden von Molekülen zur Spitze durch das Aufbringen genügend großer Kräfte auftritt.

Contents

1 Introduction

Modern nanotechnology demands for ever smaller, faster and more efficient processors and higher data storage densities. However, the currently established silicon based technology encounters size limits due to power dissipation and quantum effects [1]. Thus, other concepts are considered such as the bottom-up approach. It involves the assembly of fundamental components from individual atoms and molecules rather then tailoring materials with lithographic processes. Thereby, functional molecules have attracted increasing attention. Their intrinsic small size on the order of 1 nm may increase the packing density of devices and intermolecular interaction can be used to yield self-assembled molecular structures. Advances in chemistry makes it feasible to design and synthesize molecules with precisely defined characteristics tailored for specific functions or applications. A huge diversity of properties has been achieved so far which often has no analog in conventional materials. Consequently, the potential use of molecules as building blocks in electrical circuits is an active field of research [2]. Molecules could be used, for example, as wires [3, 4], rectifiers [5–7] or transistors [8, 9].

One prominent example of functional molecules are molecular switches which can reversibly be changed between two or more states in response to external stimuli such as light, electric field or current. Switching may involve a change of conformation, such as the *cis–trans* isomerization of azobenzene molecules [10–14], dipole orientation [15, 16], spin state [17, 18], charge state [19–21] or bond formation [22]. Such molecules appear to be particularly promising for data storage devices [23, 24].

A key requirement for controlling and reading the switch states of molecules by electrical means is their embedding in suitable environments such as attachment

to a substrate. Metal surfaces are of special interest since they represent electrodes that are needed to contact the molecules [25]. However, interactions with a substrate can substantially modify the molecule's properties. The performance of an intrinsically switchable molecule is often diminished or its functionality can even be completely suppressed [26].

In order to develop reliable molecular electronic devices it is necessary to understand the switching mechanisms in more detail as well as adsorbate–substrate interactions that influence the molecular properties. The gained knowledge may help to adapt the chemical design of the molecules. One aspect is the identification of the molecule's adsorption geometry. Many molecular functionalities, such as the isomerization process, are directly linked to the structure of the adsorbed molecules and even a slight variation in the structure can lead to the suppression of bistability on the surface [27]. One promising strategy to retain molecular functionalities upon adsorption is the decoupling of the molecular switch from the surface with, for instance, ultrathin insulating layers [28] or by developing self-decoupled molecules using spacer groups [29], platforms [30, 31] or double-decker designs [32] to lift the functional unit from the substrate.

Aside from possible applications, molecular adsorbates represent interesting systems for fundamental research which offer the possibility to explore phenomena at the nanometer scale.

The investigation of molecular systems at interfaces is only possible due to the development of powerful experimental techniques. Scanning tunneling microscopy (STM) and atomic force microscopy (AFM) performed in ultra-high vacuum (UHV) and at low temperatures offer the unique possibility of investigating adsorbates on surfaces at the atomic scale. Used in combination, these techniques allow to gain a deep insight into the electronic, conformational and mechanical properties of the investigated systems.

Moreover, both techniques offer the possibility of manipulating single molecules and adatoms and thus to precisely probe their functions. Manipulation of adsorbates may involve a controlled change in their lateral [33–36] and vertical [37–47] positions, inducing chemical reactions [22, 48, 49] or switching between different conformations [26, 50–52].

In this thesis, a combination of low-temperature STM and AFM is used to study the structural and electronic properties of switchable molecules on metal surfaces with the aim to understand the properties of molecule–metal interfaces. Furthermore, the combination of the experimental data with calculations yield an accurate description of the properties of molecular systems that were investigated in this work.

The basic principles of the used measurement techniques are described briefly in the following chapter.

In Chapter 3, the switching of azobenzene based tripod molecule tris-[4-(phenylazo)-phenyl]-amine (TPAPA) on Ag(111) is studied. Structural information of the switched states are deduced from STM and AFM data as well as DFT calculations.

The focus of Chapter 4 is on two closely related cyclophane molecules with a three-dimensional double-decker structure on Ag(111). Combined STM and AFM investigations along with DFT calculations unravel the composition of molecular islands with coadsorbed Ag adatoms.

In Chapter 5, the force in AFM junctions containing iron tetraphenylporphyrin chloride (FeTPPCl) molecules is investigated. The charge configuration within the junction is systematically modified by transferring Cl ligands between molecules and the tip. A point charge model suggest that the relevant forces arise mainly from image interaction with the conducting tip and sample and electrostatic interaction between the ligands.

The following part of this thesis has been published in a peer-reviewed journals:

- Chapter 3:
  Katharina Scheil, Thiruvancheril G. Gopakumar, Julia Bahrenburg, Friedrich Temps, Reinhard J. Maurer, Karsten Reuter and Richard Berndt,
  Switching of an Azobenzene-Tripod Molecule on Ag(111),
  J. Phys. Chem. Lett. **7**, 2080 (2016)

- Chapter 4:
  Katharina Scheil, Nicolás Lorente, Marie-Laure Bocquet, Pascal C. Hess, Marcel Mayor and Richard Berndt,
  Adatom Coadsorption with Three-Dimensional Cyclophanes on Ag(111),
  J. Phys. Chem. C. **121**, 25303 (2017)

In Chapters 3 and 4 a few changes to the published manuscripts were carried out without changing the content.

2 Fundamentals

Since the invention of the scanning tunneling microscope (STM) in 1982 and the atomic force microscope (AFM) in 1985 both have become extremely powerful tools for experiments in surface science due to the ability of investigating and manipulating surfaces at the atomic scale.

Since all experiments in this thesis were performed with a combined low temperature STM/ AFM, the basic principles of both techniques are addressed in this chapter with the focus on certain aspects that are relevant to this thesis. Further detailed descriptions of STM and AFM can be found, for example, in Refs. [53–60].

2.1 Scanning Tunneling Microscopy

The STM allows to investigate adsorbates on conducting samples. The technique utilizes the quantum mechanical tunneling effect, a phenomenon where a particle passes a potential barrier that it classically could not overcome. In low temperature STM the potential barrier is formed by the vacuum gap between a sharp metallic tip and a conducting sample surface. At a temperature of $T = 0\,\mathrm{K}$ the energy bands of tip and sample are filled with electrons up to their Fermi energies. The two electrodes are connected to a voltage source. For $0\,\mathrm{V}$, the Fermi levels are aligned. By applying a voltage V between tip ans sample the Fermi levels can be energetically shifted by eV with respect to each other. For sufficiently small tip–sample distances, electrons can tunnel from one electrode to the other

with a probability T. The probability T can be approximated using the Wentzel-Kramers-Brillouin (WKB) model, which considers electrons tunneling through a one dimensional trapezoidal barrier of width z [61]:

$$T(z, V, E) \propto exp(-2\kappa z) \quad \text{with} \tag{2.1}$$

$$\kappa = \frac{\sqrt{2m}}{\hbar}\sqrt{\overline{\Phi} + \frac{eV}{2} - E}, \tag{2.2}$$

where m is the electron mass, e the elementary charge, $\hbar$ the reduced Planck constant, $\overline{\Phi}$ the mean work functions of sample and tip and E the electron's energy.

At 0 K the tunneling current can be expressed as [61]:

$$I(z, V) \propto \int_0^{eV} \rho_s(E)\rho_t(E - eV)T(z, V, E)dE, \tag{2.3}$$

where ρ_s and ρ_t are the local densities of states (LDOS) of the sample and tip and E is the energy of states participating in the tunneling process.

For metals $\kappa \approx 1\,\text{Å}^{-1}$, so the tunneling current decreases by roughly an order of magnitude when the the tip–sample separation is increased by 1 Å, and vice versa [54]. Consequently, STM measurements are highly sensitive to the tip displacement and most of the tunneling current is carried by the tip atom that is closest to the sample.

The exact shape of the tip and its LDOS is typically unknown in STM experiments. In the approach by Tersoff and Hamann the tip is modeled by one atom with only s-wave states. With this approximation, the current is proportional to the integrated LDOS of the sample at the position of the tip atom [62, 63].

STM images are acquired using two different operation modes both utilizing the tunneling current. In the constant-current mode the tip is scanned across the surface while the tunneling current is kept at a preset value. This is achieved by adjusting the distance of the tip to the surface with a feedback loop. The vertical tip displacement at all measurement positions provides a topographic image. A STM topograph not only depends on the geometry of the sample but also on its electric properties since the tunneling current depends on the LDOS of the sample (Eq. 2.3) which is a function of both position and energy [64, 65]. The interpretation of STM images may not always be straightforward, for example, topographs of decoupled adsorbates such as three-dimensional molecules (Chapter 4).

A second imaging possibility is to acquire current maps at a constant vertical tip displacement without an adjustment of the tip–sample distance. This method requires extra attention to surface structures, thermal drift and environmental vibrations to prevent tip crashes. In combined STM/AFM setups current maps can be acquired simultaneously to constant height AFM measurements of the frequency shift. The effect of an AFM measurement on the measured tunneling current is accounted for in Section 2.8.

2.2 Scanning Tunneling Spectroscopy

In order to gain the electric properties of the sample, the differential conductance dI/dV is usually determined as a function of the applied voltage. Within the WKB approximation (Eq. 2.3), the differential conductance is expressed as:

$$dI/dV \propto \rho_s(E)\rho_t(E-eV)T(z,V,E) \tag{2.4}$$

$$+\int_0^{eV} \rho_s(E)\frac{\rho_t(E-eV)}{dV}T(z,V,E)dE \tag{2.5}$$

$$+\int_0^{eV} \rho_s(E)\rho_t(E-eV)\frac{dT(z,V,E)}{dV}dE. \tag{2.6}$$

The last two terms are usually neglected under the assumption of a constant tip LDOS and minor changes in the tunneling transmission probability at small voltages [66]. Under these assumptions the differential conductance dI/dV is directly proportional to the sample LDOS:

$$dI/dV \propto \rho_s(E)T(z,V,E). \tag{2.7}$$

The differential conductance can be obtained experimentally in scanning tunneling spectroscopy (STS). For that purpose a voltage ramp superimposed with a modulation is applied to the sample and the current is measured as a function of the voltage. The differential conductance is obtained using lock-in techniques.

2.3 Atomic Force Microscopy

The AFM is closely related to the STM. Both share the key components except that the tunneling tip is replaced by a force sensor. The basic principles of the used measuring technique as well as the forces relevant during ultra-high vacuum (UHV) experiments in this thesis are presented in the following.

2.4 Dynamic Non-Contact AFM with Frequency Modulation

Initially, AFM force measurements were performed by observing the deflection q of a cantilever with stiffness k under interacting forces between tip and sample, so called static AFM. Since the deflection is directly linked to the force F acting on the tip via $q = F/k$ this relation makes the interpretation straightforward. However, when the interacting force gradient exceeds the cantilevers stiffness in non-contact AFM measurements, a jump-to-contact instability occurs which might damage the sample under investigation. While stiffer cantilevers can prevent this problem they lead to a reduction of the measurement sensitivity. This issues can be avoided using dynamic methods, which enable highly sensitive force measurements with stiff cantilevers [56].

The mode used in this thesis is dynamic non-contact AFM with frequency modulation (FM-AFM) where a cantilever is excited to oscillate at its resonance frequency f with constant amplitude A [67]. Typical frequencies and oscillation amplitudes within this method are between 20–200 kHz and between 0.05–5 nm. The force is measured indirectly, the main observable is the change in the cantilevers resonance frequency caused by forces between tip and sample. The cantilever oscillates at its eigenfrequency $f = f_0$ when no forces act on it. Interacting tip–sample forces F_{ts} cause the resonance frequency to shift by Δf so that the cantilever oscillates at a frequency $f = f_0 + \Delta f$.

When the force gradient $k_{ts} = -\partial F_{ts}/\partial z$ is constant over the range of oscillation the frequency shift follows [56]:

$$\Delta f = f_0 \frac{k_{ts}}{2k}, \tag{2.8}$$

where k is the cantilevers spring constant. A more general expression for the relation between the measured frequency shift Δf and the force F_{ts} may be used when the force gradient k_{ts} varies over the oscillation range [68]:

$$\Delta f = -\frac{f_0}{\pi k A} \int_{-1}^{1} F_{ts}(z + A(1+u)) \frac{u}{\sqrt{1-u^2}} du, \tag{2.9}$$

where z is the distance of closest tip approach to the surface. The frequency shift is a weighted average of the force over one oscillation period.

The experimental implementation for obtaining the frequency shift in FM-AFM is sketched in Fig. 2.1. A cantilever with sharp tip attached to it is mechanically excited at its resonance frequency f by a piezo actuator. The oscillation deflection $q(t)$ is usually detected via optical beam deflection or, as in this thesis, via a self sensing cantilever [56] (see Section 2.11). The deflection signal is first amplified and bandpass filtered for noise reduction and then enters an amplitude control circuit and a phase locked loop (PLL).

The amplitude controller keeps the cantilevers oscillation amplitude A constant. For that purpose the dc-converted deflection signal is compared to an amplitude setpoint A_0 and the excitation amplitude V_{exc} is adjusted by a feedback controller. V_{exc} is related to the energy dissipation in the system due to tip–sample interactions (cf. Section 2.9).

In order to maintain excitation on resonance, a phase difference of 90° between the excitation and response signal of the sensor is needed. This can either be done by driving the sensor with the phase shifted deflection signal or, as in this thesis, by using a PLL to supply the excitation signal which can lock to a specific phase. The advantage of using the excitation signal from the PLL is that it usually has a higher spectral purity than the sensor deflection signal.

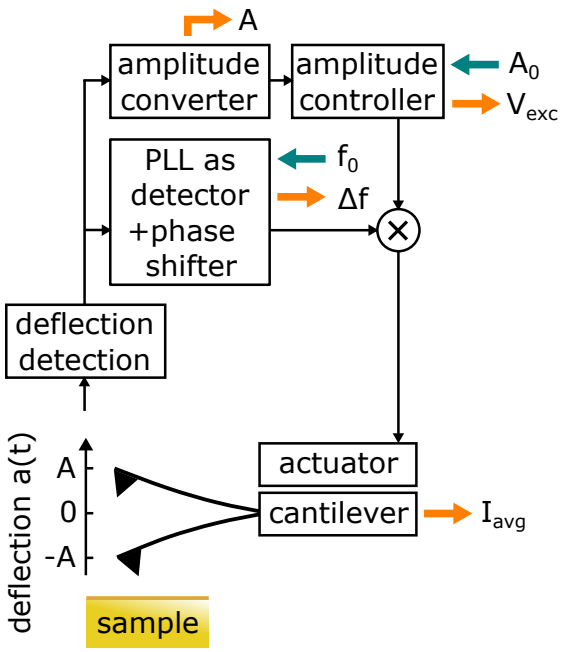

Figure 2.1: Schematic diagram of the AFM feedback loop for constant amplitude control and frequency shift measurement with a phase locked loop (PLL) adapted from Refs. [56, 69]. f_0 is the cantilevers eigenfrequency and A_0 is the amplitude setpoint. The frequency shift Δf, the excitation signal V_{exc}, the oscillation amplitude A and the averaged tunneling current I_{avg} are usually the recorded signals.

In addition, the PLL provides a signal proportional to the frequency shift $\Delta f = f - f_0$ of the response signal to a set reference frequency, i.e. the cantilevers eigenfrequency f_0. The Δf signal can be used as feedback parameter for obtaining topographs of constant frequency shift, for acquiring frequency shift maps at constant height or for performing force spectroscopy, i.e. measuring the frequency shift as a function of the tip–sample distance. However, for practical usage, the frequency shift should be converted to a force.

2.5 Force Extraction

In frequency-modulation AFM the quantity to be measured is the frequency shift which is not a direct measure of the force (cf. Eq. (2.9)). To get the force, deconvolution methods are necessary. Several attempts to convert the frequency shift to a force have been performed such as iterative methods [70, 71], the analysis of higher harmonics of the oscillation [72] or the use of amplitude dependence of the frequency shift [73].

However, direct deconvolution methods proposed by Giessibl [74] (numerical matrix method) and Sader and Jarvis [75] (analytical Sader-Jarvis formula) are favored. These methods where found to be most robust against the presence of

experimental noise [55] and extract forces with similar accuracy [76]. However, the matrix method is very sensitive to the ratio A/d of the oscillation amplitude A and the vertical step width d of $\Delta f(z)$ data points. Often a data interpolation is necessary to optimize the deconvolution and the matrix method requires powerful mathematical routines [55]. Therefore, the most commonly used method is the deconvolution formalism by Sader and Jarvis, which is given by:

$$F(z) = 2k \int_z^\infty \left[1 + \frac{A^{1/2}}{8\sqrt{\pi(t-z)}} \right] \Omega(t) - \frac{A^{3/2}}{\sqrt{2(t-z)}} \frac{d\Omega(t)}{dt} dt, \tag{2.10}$$

where $\Omega(t) = \Delta f(t)/f_0$ and z is the closest distance between the oscillating tip and the sample. The formalism is applicable for any force law and is valid for arbitrary oscillation amplitudes.

For the formalism itself a worst case error of 7 % at the force minimum was found [76]. The error comes from a approximation made in the derivation of the formalism [75].

In addition the uncertainty of k, A and z have to be taken in to account. The main contribution to the uncertainty of the force comes from the uncertainties of k. We estimate the uncertainty of the force to be around 30 % with the force sensor and amplitude calibration used in this thesis. The tuning fork used in this thesis as well as the amplitude calibration are described in Section 2.11 and 2.12, respectively. Nevertheless, the uncertainty of the force does not affect the comparison of force curves acquired with the same cantilever and tip.

It has to be noted that the Sader-Jarvis method is only valid for constant oscillation amplitudes. In the formalism the integration is performed from z to ∞ but measurements provide finite data points. Therefore, the method requires data acquisition over a adequate tip–sample distance range from the region of interest and distances large enough such that the force converges to zero. If the force has nevertheless force contributions at the largest acquired distance, an extrapolation may be applied. The implementation of the force deconvolution used in this thesis is described in detail in Ref. [77].

2.6 Interacting Forces

AFM allows to probe interacting forces between a sample and a tip. In contrast to STM, where mainly the last tip atom contributes to the measured tunneling current, the overall force is composed of different contributions which differ in strength and distance range. In the following the most important forces for this thesis are discussed. The two main long-range interactions are the van der Walls (vdW) and capacitance forces with a range up to 100 nN [56].

The attractive van der Waals forces originate from electromagnetic interaction of fluctuating dipoles of tip and sample atoms. The vdW potential between two atoms has a distance dependance of $\propto z^{-6}$, which suggest a short range character. However, in AFM experiments the vdW interaction of many atoms in tip and sample contribute to a resulting total force. Hamaker calculated the vdW interaction between continuous macroscopic objects assuming additivity of individual pairwise contributions and uniform material properties [78]. With the tip–sample AFM junction simplified as a sphere with radius R at a distance z from a flat infinite surface the vdW potential and force are:

$$V_{vdW} = -\frac{HR}{6z}, \qquad F_{vdW} = -\frac{HR}{6z^2}, \tag{2.11}$$

where H is the material dependent Hamaker constant [79].[1] The resulting vdW forces due to the macroscopic part of the tip features a long range character and can become significant. A typical Hamaker constant in the order of $H = 1\,\text{eV}$ [59] and a tip with radius of $R = 10\,\text{nm}$ at a distance $z = 1\,\text{nm}$ result in a vdW force of $F_{vdW} \approx 0.3\,\text{nN}$, which is a major force contribution at the nanometer scale. In order to interpret force versus distance curves, independent of the macroscopic tip shape, a background correction is usually performed (Section 2.7).

A strong attractive force may also lead to experimental problems. If the attraction becomes to strong, the tip may be pulled into contact, molecules under investigation may be picked up by the tip or the frequency shift may exceed the bandwidth of the AFM feedback loop. For this reason, a very sharp tip is crucial for AFM experiments.

In a tunneling junction attractive capacitance forces usually occur between the tip and the sample due to a potential difference ΔV between both electrodes [59]. The capacitance force can be written as

$$F_C(V) = \frac{1}{2}\frac{\partial C(z)}{\partial z}\Delta V^2, \tag{2.12}$$

where z is the tip–sample distance and $C(z)$ is the tip–sample geometry dependent capacitance [57, 58]. The potential difference is $\Delta V = V + V_{CPD}$ where V is an external applied sample voltage and V_{CPD} the contact potential difference with respect to the sample. The contact potential difference is caused by different tip and sample work functions, W_t and W_s, respectively [80]:

$$V_{CPD} = \frac{W_t - W_s}{e}, \tag{2.13}$$

where e is the elementary charge. When the electrodes are contacted, electrons flow from the electrode with lower to the one with higher work function. This results in charges on both sides of the junction and leads to an electrostatic attractive force between the electrodes. Figures 2.2 (a) and (b) show the electronic energy levels of tip and sample with and without contacted electrodes.

[1] Expressions for conical, pyramidal and more complex tip shapes can be found in Ref. [57].

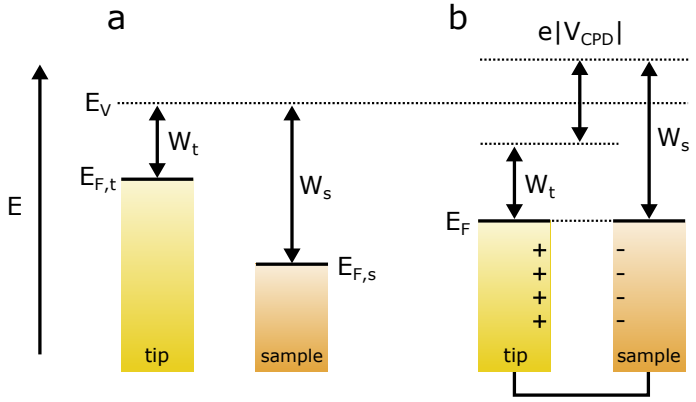

FIGURE 2.2: (a) Tip and sample represent two electrodes with different work functions W_t and W_s ($E_{F,t}$ and $E_{F,s}$ are the Fermi levels of tip and sample, E_V is the vacuum level). (b) When brought into electrical contact, electrons flow from the electrode with lower into the one with higher work function and the Fermi levels align (E_F), which leads to a contact potential difference V_{CPD}. Adapted from Ref. [81].

The capacitance force follows a parabolic behavior as a function of the applied voltage. At the parabola's apex the applied voltage has the same magnitude as the contact potential difference but opposite sign. Thereby, the applied voltage is such that the surface charge in the contact area and the capacitance force are nullified ($\Delta V = V + V_{CPD} = 0$). Kelvin probe force microscopy (KPFM) uses this relation to determine the contact potential difference experimentally.[2]

The effect of the capacitance force can therefore be nullified by applying adequate voltages to compensate the contact potential difference. However, in practice a complete compensation is not feasible since the work function is very sensitive to the local geometry of the surface [57, 83]. Moreover, typical values of the contact potential difference in the systems used in this thesis, i.e. molecules on Ag(111) and Au(111) surfaces, are in the order of $\approx$ 500–600 mV. AFM experiments in this thesis, however, are performed at smaller voltages to prevent damages of the molecular systems due to increased currents at small tip–sample separations close to the contact.

The focus in this thesis is on the side specific short range component of the force. At small tip–sample distances below 1 nm, additional attractive interactions can be found such as covalent or metallic bonding forces as well as repulsive

[2] An introduction into KPFM can be found in Refs. [80, 82].

forces due to the Pauli exclusion principle [57, 58]. A commonly used model potential to describe the interaction between two neutral atoms at distance r is the Lennard-Jones potential [79]:

$$V_{LJ}(r) = \epsilon \left[\left(\frac{r_m}{r} \right)^{12} - 2 \left(\frac{r_m}{r} \right)^{6} \right] \text{and} \tag{2.14}$$

$$F_{LJ}(r) = -\frac{\partial V_{LJ}(r)}{\partial r}, \tag{2.15}$$

where ϵ is the depth of the potential well, r_m position of the potentials minimum and F_{LJ} the resulting force. The r^{-12} term describes the Pauli repulsion at short distance ranges and the r^{-6} term the vdW attraction at long ranges. The Lennard-Jones potential is a good approximation in many cases with, at the same time, computational simplicity compared to other methods based on quantum mechanical modeling.

Electrical charges may be found in the STM/AFM junction. Many processes can introduce charges into a tip–sample junction, for example during the surface preparation [58]. Charges can be trapped on insulating layers [21, 83] and in turn commonly used polar thin insulating layers form a periodic charge arrangement [84–86]. Beyond that, molecules may provide charged ligands as shown in Chapter 5. The interaction between charged particles can be described by Coulomb's law.

Since in combined STM/AFM tip and sample are conducting electrodes, the presence of charges can lead to image forces. The image force is the interaction due to polarization of a metal electrode by the charges [57]. The resulting force can be described classically with the method of image charges [87–89] (Chapter 5). In this method the force is described by Coulomb's law between the charged particle, simplified as point charge, and an image charge of opposite sign in the conducting electrode.

2.7 Extraction of the Short Range Force

Generally, the AFM measures a signal related to the total tip–sample force, which is composed of different force contributions acting between tip and sample. The quantity of interest in AFM experiments is usually the site specific short range component of the force between the tip apex and the surface. However, in most cases the measured total tip–sample force has significant non-site-specific long range force contributions such as van der Waals and electrostatic forces from the underlying substrate.

In order to extract the short range force, different attempts to remove the long range components have been made. One approach is to fit a model to the long range background and extrapolate the fit to the short range regime. However, the result of the extrapolation highly depends on the fitting regime and the chosen model. In Ref. [90] several models are compared and criteria for the selection of the transition point between the long- and short-range interaction regime are discussed.

One of the most common method is the 'on-minus-off' method [91–93]. This method uses two experimental force curves both acquired over the same range of tip–sample separations. One curve is obtained at the relevant sample site and a second curve serves as reference. The reference curve has to be acquired at a region of the surface that excludes any relevant short-range interaction and ideally only contains the long range force contribution. A subtraction of both curves removes the long range force components.

2.8 Current Measurement in Frequency Modulated Non-Contact AFM

The use of conducting samples and cantilever tips makes it possible to measure the tunneling current simultaneously to the frequency shift. Since the cantilever typically oscillates at frequencies that are higher than the bandwidth of the current-to-voltage converter, a time averaged value is measured. The time averaged tunneling current I_{av} can be expressed as [71, 94, 95]:

$$I_{av}(z) = \frac{1}{\pi}\int_{-1}^{1} I(z + A(1+u))\frac{1}{\sqrt{1-u^2}}du, \tag{2.16}$$

where z is the closest distance between the oscillating tip and the sample, A is the tip oscillation amplitude and I the instantaneous current value. The tunneling current at the closest separation between tip and sample can be extracted from the measured averaged current with the formalism of Sader and Sugimoto [95]:

$$I(z) = I_{av}(z+A) - \int_{z}^{\infty}\sqrt{\frac{2A}{\tau - z}}\left[\frac{dI_{av}(\tau)}{d\tau} - \sqrt{\frac{2}{\pi}}\frac{dI_{av}(\tau + A)}{d\tau}\right]d\tau. \tag{2.17}$$

This formula is valid for arbitrary oscillation amplitudes. A constant amplitude is required. Approximations made in the derivation of the formalism lead to an uncertainty which is similar to the one of Eq. (2.10) (5 %) [95]. The implementation of the integration formula is described in Ref. [77].

2.9 Dissipation

The formalisms of Sader and Jarvis (Eq. (2.10) and (2.17)) are only valid for constant oscillation amplitudes. In the experimental setup a feedback controller is used to adjust the oscillation amplitude. The excitation amplitude (V_{exc}) needed in order to maintain a constant oscillation amplitude A, is a measure related to the energy loss in the motion of the cantilever. The cantilever itself dissipates energy due to internal friction. This energy dissipation D_0 per oscillation cycle is given by [96]:

$$D_0 = \frac{2\pi E}{Q}, \tag{2.18}$$

where $E = kA^2/2$ is the energy of the cantilever, Q is the quality factor and k the spring constant of the cantilever.

Nonconservative forces between tip and sample lead to additional energy loss in the motion of the cantilever. The resulting damping D_{ts} can be extracted from the driving amplitudes far away ($V_{exc,0}$) and close to the sample (V_{exc}) [70, 96]:

$$D_{ts} = D_0 \left(\frac{V_{exc}}{V_{exc,0}} - \frac{f}{f_0} \right), \tag{2.19}$$

where f_0 is the cantilevers eigenfrequency and f the resonance frequency close to the sample. In our experiments $f/f_0 \approx 1$ since the frequency shifts are very small compared to the cantilevers eigenfrequency ($\Delta f < 10^{-3} f_0$). Force versus distance curves, shown in this thesis, all exhibit constant amplitudes and relations $V_{exc}/V_{exc,0} < 1.3$.

2.10 Experimental Setup

All experiments presented in this thesis were performed with a commercial combined low-temperature beetle-type STM/AFM operating at ultra-high vacuum (UHV) conditions at $\approx$ 5 K with transferable samples and sensors. The sensor used for STM/AFM measurements is described in Section 2.11. The system comprises three separable chambers, a measuring chamber containing the microscope connected to a cryostat, a preparation chamber and a chamber used as a load-lock to transfer samples and sensors in and out of the vacuum. Samples can be prepared by noble gas ion bombardment and heating with button heaters. Molecules can be evaporated from heatable crucibles onto the sample at adjustable temperature (Liquid nitrogen temperature up to several 100°C) in the preparation chamber. For a more detailed description of the experimental setup the reader is referred to Ref. [77]. The preparation procedures for the investigated molecules presented in this thesis are explained in the respective chapters.

2.11 The AFM Sensor

A cantilever used for AFM experiments is characterized by its stiffness or spring constant k, its eigenfrequency f_0 and its quality factor Q, which indicates how sharp the resonance is. In the experiments performed in this thesis a self sensing cantilever in the qPlus design was used [97–99].

The qPlus sensor consists of a quartz tuning fork with eigenfrequency $f_0 = 32768\,\mathrm{Hz}$ and with a spring constant of approximately $1800\,\mathrm{N/m}$ found in previous investigations [100]. The spring constant of stiff cantilevers can be obtained with different methods such as from the bending of the sensor as a function of the applied force [101], the change in eigenfrequency due to adding small masses to the cantilever [102], by analysis of the thermal noise spectrum [103, 104] or calculation from the sensors elastic properties [105]. A study comparing these methods obtained uncertainties of 10 % to 14 % for the cantilever stiffness of qPlus sensors used in this thesis [100]. However, larger deviations of the stiffness were reported by several authors therefore we allow for an uncertainty of 30 % [106, 107].

One prong of the tuning fork is glued to a mount, the other is free to oscillate when mechanically excited (**1** in Fig. 2.3 (a)). A tungsten tip wire with a diameter of $50\,\mu m$ is attached to the free prong and serves as probe tip (**2** in Fig. 2.3 (a)). Tips were prepared by electrochemical etching with NaOH solution. The tips were further prepared in UHV by indenting them into metallic surfaces.

The sensors eigenfrequency f_0 is obtained from resonance curves where the oscillation amplitude is measured as a function of the excitation frequency for a constant excitation amplitude. Eigenfrequencies in the range of $f_0 = 20$–$27\,\mathrm{kHz}$ were obtained for sensors used in this thesis depending on the dimensions of the attached tip wire and the mass of glue used for its fixation. In Fig. 2.3 (b) a typical resonance curve is shown with a resonance of 23.022 kHz.

Single crystal quartz tuning forks have the benefit of a low internal dissipation and a high quality factor Q. With qPlus sensors quality factors in the range of 10^4 in low temperature UHV conditions can be achieved [97, 99, 108]. The quality factor is defined as $Q = f_0/B_{-3dB}$ where B_{-3dB} is the full width of the amplitude resonance curve at $-3\,\mathrm{dB}$ [109]. The resonance curve in Fig. 2.4 (b) features $B_{-3dB} = (0.5 \pm 0.1)\,\mathrm{Hz}$ which results in a quality factors of $Q \approx 45000$.

To avoid crosstalk between the STM and AFM signals, the tip wire is electrically isolated from the prong but connected with a gold wire with a diameter of $\approx 10\,\mu m$ (**3** in Fig. 2.3 (a)) to measure the tunneling current independently of the AFM signal. The AFM signal is detected via cables connected to the tuning fork contacts (**4** in Fig. 2.3 (a)).

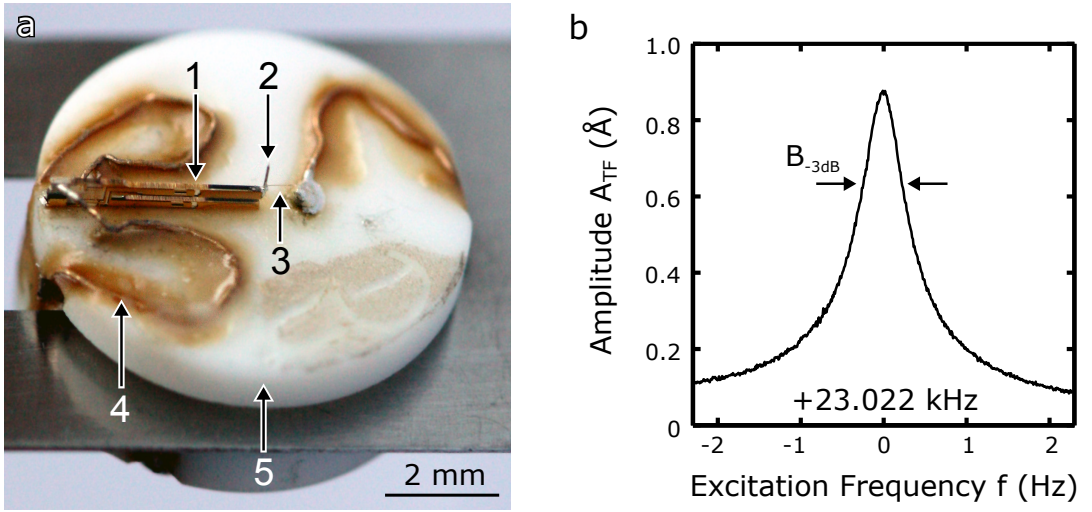

Figure 2.3: (a) The qPlus sensor (adapted from Ref. [110]). A quartz tuning fork (1) features a tungsten tip wire (2) at the face side of a prong. The tip wire is connected with a $\approx 10\ \mu m$ gold wire (3). The tuning fork electrodes are connected with gold wires (4). All components are glued to a ceramic (Macor) body (5). (b) Oscillation amplitude A_{TF} as a function of the excitation frequency f centered around the sensors resonance $f_0 = 23.022\,\text{kHz}$ (Amplitude of the driving signal: $V_{exc} = 0.2\,\text{mV}$, cantilever stiffness: $k = 1800\,\text{N/m}$). The bandwidth is $B_{-3dB} = (0.5 \pm 0.1)\,\text{Hz}$ resulting in a quality factor of $Q \approx 45000$.

2.12 Amplitude Calibration

The oscillation of the free prong with amplitude A_{TF} results in a piezo electric voltage at the electrodes of the tuning fork and a small current which is amplified by a current-to-voltage amplifier. After filtering for noise reduction and further amplification, a voltage signal with amplitude A_V is obtained that is proportional to the actual sensor deflection:

$$A_{TF} = \alpha A_V \tag{2.20}$$

A calibration is necessary to find out the actual sensor deflection. For the oscillation amplitude calibration we make use of the capability to measure the tunneling current simultaneously to AFM measurements [56, 111]. The force sensor is driven at constant oscillation amplitudes. The measured tunneling current is an average value due to the small bandwidth of the current-to-voltage converter. The vertical tip displacement Δz is controlled by the STM feedback loop to maintain a constant current. The relationship between A_V and the tip–sample distance is recorded (Fig. 2.4).

For the calibration we utilize the fact that for high enough oscillation amplitudes (in the nanometer range [111]) a change in oscillation amplitude ΔA is

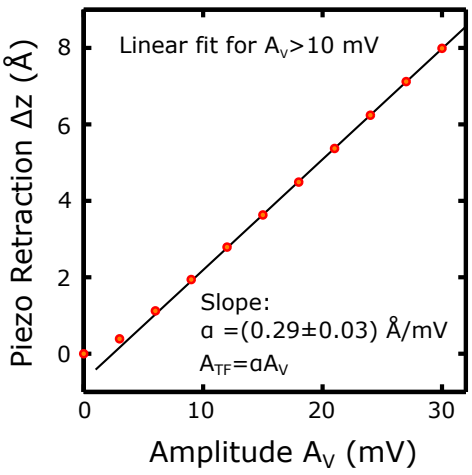

FIGURE 2.4: Relation between the tip retraction Δz and readout oscillation amplitude A_V at constant average tunneling current ($U = 100\,\mathrm{mV}$, $I = 30\,\mathrm{pA}$). The slope in the linear part corresponds to the calibration factor in Eq. (2.20) $\alpha = (0.29 \pm 0.03)\,\text{Å/mV}$.

proportional to the change in tip retraction Δz in order to maintain a constant current [56, 111].

The calibration factor α is extracted from the curves slope of the experimental data for sufficiently large amplitudes. One can then calibrate the whole amplitude range down to very small values. The uncertainty of the amplitude mainly depends on the calibration of the piezo constants, performed at atomic step edges, which is about 10 %.

Figure 2.4 shows an amplitude calibration curve recorded during this thesis. The piezo retraction Δz increases linearly for readout amplitudes A_V larger than 10 mV. From the slope a calibration factor of $\alpha = (0.29 \pm 0.03)\,\text{Å/mV}$ was extracted.

2.13 Definition of the Tip–Sample Distance

In this thesis, frequency shift curves and therefore the extracted force curves (Eq. (2.10)) are acquired as a function of the vertical piezo displacement Δz. The piezo displacement Δz is given with respect to a reference point defined by the current and voltage set points when the feedback loop is opened. The absolute tip–sample distance of force curves is linked to the piezo displacement by an offset. To determine the offset, contact curves are acquired with a non oscillating tip. Figure 2.5 (a) shows a typical contact curve measured with a gold covered tip on a Au(111) substrate. When the tip–sample distance decreases (negative Δz) a sudden jump in the tunneling current occurs at a certain piezo displacement Δz_c (arrow in Fig. 2.5 (a)) followed by a plateau in the current. This

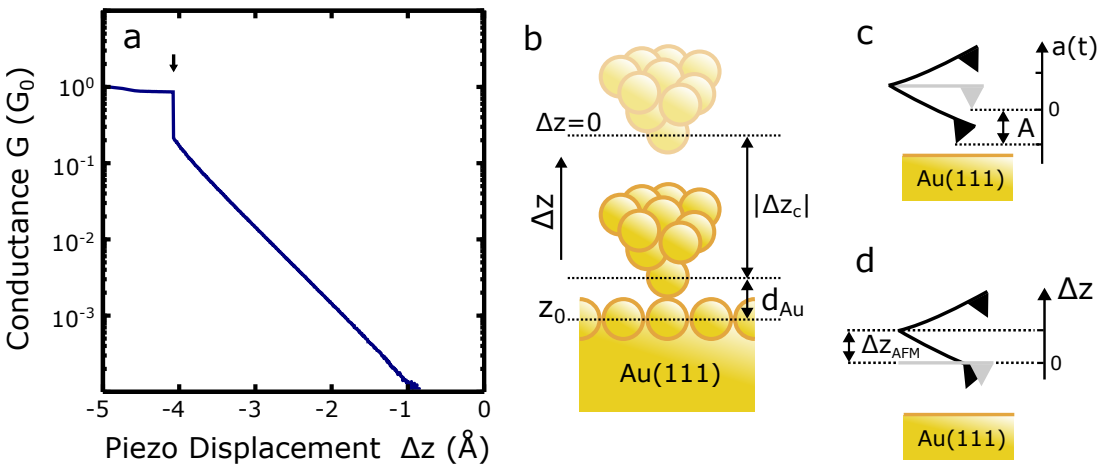

Figure 2.5: (a) Conductance G in units of the quantum of conductance G_0 as a function of the tip displacement Δz measured with a gold tip over Au(111). $\Delta z = 0$ Å is defined by the feedback parameters ($V = 100$ mV, $I = 1.3$ nA). A sudden jump (arrow) indicates the point of mechanical tip–sample contact. (b) Definition of the tip height of a non oscillating tip. The outermost atomic layer is defined as zero height z_0. The feedback loop is opened at $\Delta z = 0$ Å, $|\Delta z_c|$ is the piezo displacement at which mechanical contact is formed and $d_{Au} = 2.88$ Å is the distance between nearest neighbors in a Au crystal [112]. (c, d) Sketches of an oscillating (black) and non oscillating cantilever (gray). (c) The closest tip–sample separation of an oscillating cantilever is smaller by the oscillation amplitude A compared to a non oscillating cantilever at the same piezo displacement. (d) In constant current mode a piezo retraction Δz_{AFM} occurs for an oscillating cantilever compared to a non oscillating cantilever.

sudden jump is interpreted as the point of mechanical contact between the tip and the sample surface.

We define the position of the outermost atomic layer as the point of zero height (z_0 in Fig. 2.5 (b)). When a mechanical contact is formed, the distance of the outermost atomic layer and the last tip atom is assumed to be $d_{Au} = 2.88$ Å, the distance between nearest neighbors in a Au crystal [112].

Forces curves are measured as a function of the closest separation between the oscillating tip and the sample [56, 75]. Therefore, the closest tip–sample separation for an oscillating tip (black in Fig. 2.5 (c)) is smaller by the oscillation amplitude A compared to the tip–sample distance of a non oscillating tip at the same piezo displacement (gray in Fig. 2.5 (c)). In addition a piezo retraction Δz_{AFM} occurs in constant current mode when the tip starts to oscillate compared to a non oscillating tip (Fig. 2.5 (d), cf. Section 2.12).

The investigation of a system other than the bare metal tip over the substrate may lead to an additional tip displacement Δz_{sys}. Positioning the tip over molecules involve a tip retraction by the apparent height of the molecule with respect to the surface. A functionalization of the tip, such as a Cl-termination of

a gold tip in Chapter 5, leads to an additional displacement compared to a bare metal tip.

In total, the offsets to gain the absolute height z_{offset} of an oscillating tip is:

$$z_{offset} = |\Delta z_c| + d_{Au} + \Delta z_{AFM} - A + \Delta z_{sys}. \tag{2.21}$$

3

Switching of an Azobenzene-Tripod Molecule on Ag(111)

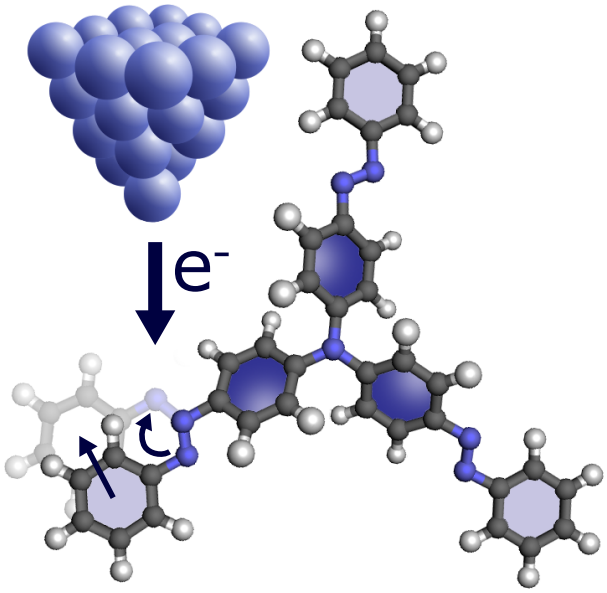

3.1 Introduction

The *trans–cis* isomerization of azobenzene (AB) and its derivatives has been investigated in detail, partially because AB may be modified with various substituents and still exhibits robust light-driven switching [113, 114]. Unfortunately, this robustness does not extend to the adsorption on metal substrates. Drastically reduced efficiencies of light-induced switching of AB when adsorbed to Au have been reported and attributed to rapid excited-state quenching [12, 14, 115–118]. Dispersion-corrected density functional theory (DFT) calculations have recently identified an additional factor that may be involved in reducing efficiency [119]. Once adsorbed on Au(111) or Ag(111), the barrier that prevents the *cis* isomer to return to the *trans* ground state via a rotation is drastically reduced. This effect, which may effectively eliminate *trans–cis* bistability, was predicted to be particularly significant on Ag(111) and more reactive substrates. An increase of the rate of thermal *cis–trans* isomerization of azobenzene-containing molecules has been reported from gold nanoparticles [120, 121].

Using a scanning tunneling microscope (STM) extreme current densities may be achieved through a single molecule [26, 45, 122, 123]. Using this approach, electron-induced switching of AB derivatives on Au remains possible although efficiencies scatter widely [10, 12, 124–127]. Despite expectations for azobenzene (AB)-containing molecules on Ag(111) [119], we find that switching of tris-[4-(phenylazo)-phenyl]-amine (TPAPA) on Ag(111) is feasible.

TPAPA comprises three AB units connected via an amino linker in a three-fold symmetric fashion [128–130]. We demonstrate that each of the AB subunits may be reversibly and selectively switched between two states by injecting electrons. Switching may also be triggered by passing current through the central amino nitrogen atom. From scanning tunneling spectroscopy and atomic force microscopy (AFM) along with extensive density functional theory (DFT) calculations we find that the switching is not due to a *trans–cis* isomerisation. Rather, it involves a reorientation of the N–N bond of AB, which we suggest to proceed through a twisting motion of the azo-bridge that leads to a shift of a phenyl ring. The AB subunit is transformed between two chiral configurations that are distinct and metastable on the Ag(111) surface.

Beyond double-bond isomerization a variety of electron-induced reactions have been observed from adsorbed molecules, which encompass ring closing/opening [131], charge transfer [132, 133], conformational isomerization [134–137], changes of spin-state [17, 18], and ligand transfer [47]. Recent reviews may be found in Refs. [25, 138, 139].

3.2 Experimental Details

The Ag(111) substrate and etched W tips were cleaned by Ar^+ sputtering and annealing. The tips were further coated with silver by indenting them into the substrate. TPAPA molecules in a Ta crucible were repeatedly degassed before sublimating them at ≈ 150°C onto clean Ag(111) surfaces kept at ambient temperature in ultra high vacuum (UHV). The experiments were then performed with a STM and an AFM/STM operated in UHV at ≈ 5 K. Differential conductance (dI/dV) spectra were measured with a lock-in amplifier by superimposing a modulation ($5 - 10\mathrm{mV_{rms}}$, 7 kHz) onto the sample voltage V.

3.3 Results and Discussion

Figure 3.1 (a) shows the structure of TPAPA on Ag(111) as predicted using dispersion-corrected DFT calculations (PBE+vdW$^{\mathrm{surf}}$ [140, 141] using the CASTEP [142] package). Below, we denote the phenyl groups connected via the amino nitrogen as inner (dark blue in Fig. 3.1 (a)) and the other ones as outer groups (light blue). Steric repulsion between the hydrogen atoms of the inner phenyls induces a propeller-like twist of the AB ligands from the molecular plane of $\approx 40°$ in gas phase and $\approx 30°$ on Ag(111) [129, 130]. Viewed from the center of an adsorbed molecule, the twist may be clockwise or anticlockwise, leading to a chirality of the molecule. The energetically most favorable configuration is thereby an all-*trans* form with the outer phenyl rings lying flat on the surface to maximize dispersion interaction.

A STM topograph of a part of a TPAPA island on Ag(111) is shown in Fig. 3.1 (b). Each molecule exhibits three main protrusions (≈ 220 pm apparent height with respect to the Ag substrate) near its center, which we attribute to the inner phenyl rings. Models are overlaid over some molecules to show their orientations, which are similar to TPAPA on Au(111) [130]. In the interior of the island it is *a priori* not clear which set of protrusions belongs to a given molecule. The molecules at island edges, however, provide clear indication of the position of the outer phenyl rings. The outer phenyls lead to three lower protrusions of ≈ 170 pm apparent height. The height at the approximate positions of the azo groups between the phenyl rings is lower by ≈ 20 pm. This distinct depression at the position of the N–N azo-bridge is in qualitative agreement with previous STM data from AB on metal substrates [10–12, 14, 130, 134]. The average intermolecular distance extracted from STM images is (1.7 ± 0.2) nm and the molecular lattice is rotated by $(8 \pm 2)°$ with respect to the compact directions of Ag(111). We note in passing that most islands observed were almost enantiopure.

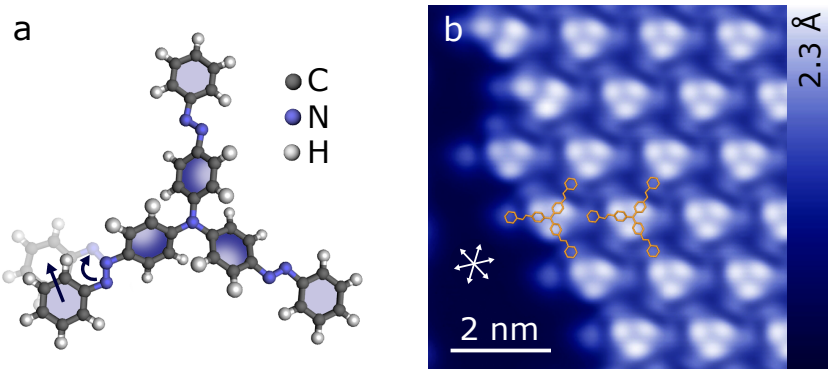

FIGURE 3.1: (a) Top-view of the minimum energy structure of TPAPA on Ag(111) from DFT calculations.Light and dark blue indicate the outer and inner phenyl rings, respectively. The shading of the inner rings shows their $\approx 30°$ anticlockwise out-of-plane twist. The outer phenyl groups are located on the left-hand side of the plane defined by the azobenzene (AB) molecular axis and the surface normal. This handedness of the adsorbed AB subunits is denoted S. Switching of an AB subunit leads to modified structure (gray). It involves a lateral shift (arrow) of the outer phenyl ring and a twirling motion of the N–N bond (curved arrow). (b) STM topograph (1.0 V, 100 pA) of an island of TPAPA molecules on Ag(111). Scaled models are overlaid. Double headed arrows indicate the compact directions of the Ag(111) surface.

Next, switching of TPAPA in islands was investigated. Placing the tip over an azo bridge (dot in Fig. 3.2 (a)) and increasing the sample voltage beyond ≈ 1.1 V leads to a clear change of the addressed AB subunit as shown in Fig. 3.2 (b). Currents of ≈ 1.1 nA were used to obtain a convenient rate of switching events. By successively repeating this procedure all three AB units were switched (Fig. 3.2 (c), (d)). To highlight the changes in the topographs Fig. 3.2 (e–g) display difference images. They reveal little change at the molecular center and the inner phenyl rings but a drastic modification of the area of the azo bridges. Subsequently, the changes were reversed (Fig. 3.2 (h–m)).

Topographic changes of the outer phenyl rings are most obvious at island edges. Figure 3.3 shows (a, b) models of molecules at an island edge (c, d) before and (e, f) after switching. The corresponding changes are displayed in Fig. 3.3 (g) and (h). The data confirm the apparent height change at the azo bridge and also reveal a lateral motion of the maximum due to the outer phenyl ring by ≈ 1.5 Å. Within islands, the phenyl rings are surrounded by the tallest features of neighboring molecules. This renders a quantitative determination of the lateral shift from constant-current images more difficult. At first glance, the shift actually appears to be smaller. However, when the superposition of the currents to the relevant phenyl ring and the neighbor is taken into account, a consistent shift is found (see Supplementary Information A.1.2).

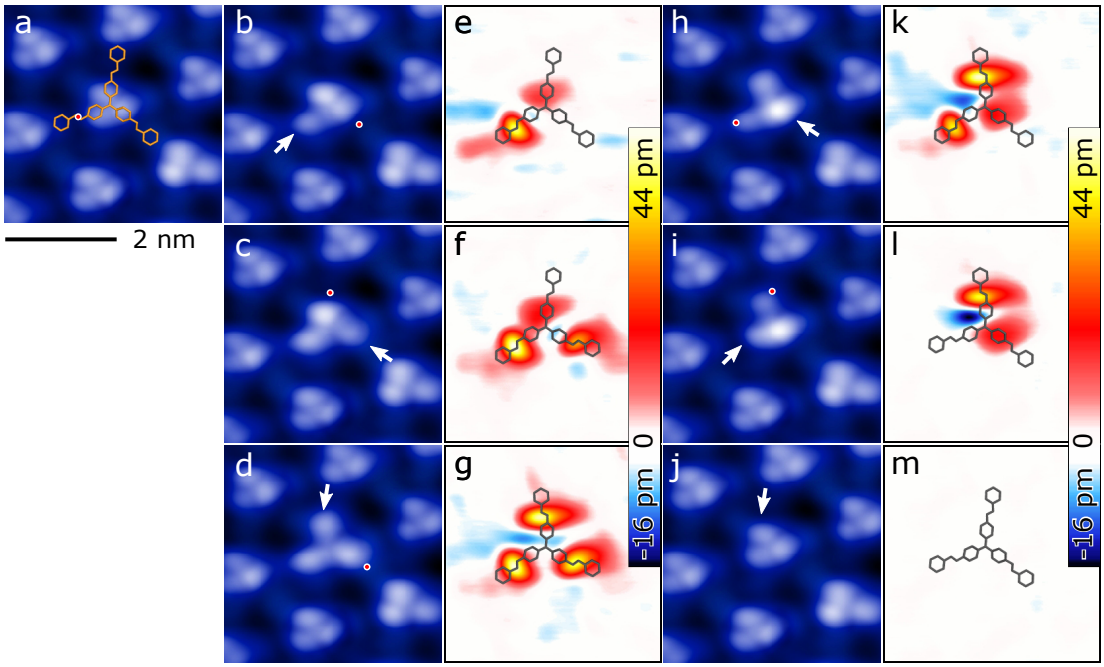

Figure 3.2: (a – d, h – j) Constant current topographs (1.0 V, 100 pA) from a TPAPA island. Dots indicates points of current injection for switching ($V = 1.3\,\mathrm{V}, I = 1.1\,\mathrm{nA}$). Arrows indicate switched AB subunits. (a) Initially the molecule at the center is in an all-*trans* state. (b) New state induced by passing current through the azo bridge of the AB subunit on the lower left. (c, d) New states obtained through current-induced of the remaining AB subunits. (h – j) Stepwise reversal of the switching until the original state is reached. (e – g, k – m) Difference images obtained by subtracting image (a) from (b – d) and (h – j). Scaled models of the molecule in (a) are overlaid. The largest changes in the images are localized to the positions of the azo bridges.

Switching may also be induced by passing current through the center of a TPAPA molecule. Time series of the current (Fig. 3.4) reveal abrupt current fluctuations between four levels, which (in a sequence of increasing currents) correspond to the pristine molecule and the states with 1, 2, or 3 switched AB units. The data demonstrate that the switching is reversible. However, since current is injected at the center of the TPAPA molecule, there is no preference for a specific AB subunit. Selectivity for a specific AB subunit is achieved by injection into a N–N bond as demonstrated in Fig. 3.2.

Switching occurs at both bias polarities with yields varying from $Y \approx 10^{-13}$ (at $V = 0.8$ and $-1.8\,\mathrm{V}$) to $Y \sim 10^{-11}$ at elevated currents and voltages (see Supplementary Information A.1.1 for details). At positive sample voltage, the switching rate approximately follows a power law $\sim I^2$, which may indicate a two-electron process.

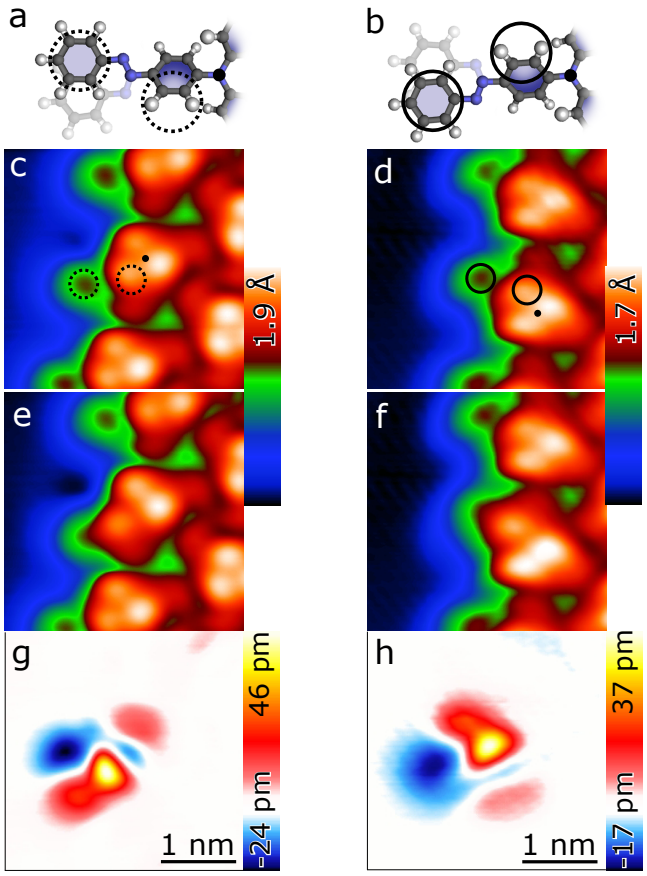

FIGURE 3.3: Switching of molecules at the edges of two islands with different molecular chiralities. Viewed from the center of a molecule, the inner phenyl rings are twisted by $\approx 30°$ (a) clockwise and (b) anticlockwise. (a, b) Models show *trans*-configurations of one AB unit. Circles indicate the positions of protrusions observed in constant current topographs. Dots mark the N center of molecules. (c, d) Topographs ($V = 1.0\,\mathrm{V}, I = 100\,\mathrm{pA}$) of TPAPA at island edges corresponding to the models in (a) and (b). (e, f) Topographs obtained after switching of the AB units at the island rim. (g, h) Difference images (e)–(c) and (f)–(d).

The most obvious switching process to consider for AB and its derivatives is *trans–cis* isomerisation. However, we exclude this possibility in the present case for two reasons. First, *trans–cis* isomerisation significantly modifies the electronic states of AB in the gas phase and also on surfaces [11, 12, 14, 134, 143]. dI/dV spectra of pristine and switched TPAPA measured at characteristic positions (Fig. 3.5), however, reveal merely minor differences between the switched and pristine states. Second, our DFT calculations revealed a number of stable *cis* states (three shown in the Supplementary Information A.1.3, Fig. A.5) all of which involve significant geometrical and electronic changes compared to the *trans* state. As detailed below, none of these changes are consistent with our

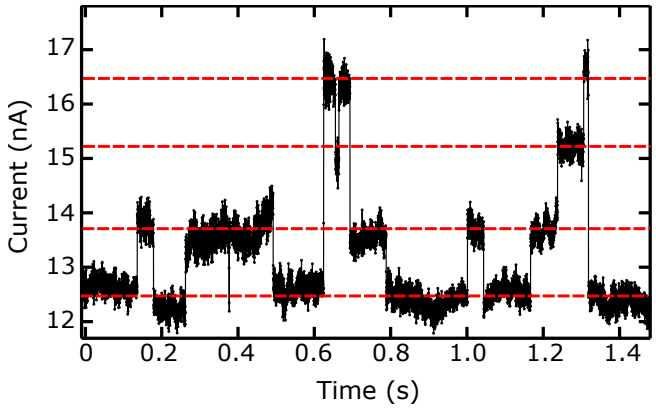

Figure 3.4: After placing the tip over the center of a TPAPA molecule, the current feedback was disabled and time series of the current were measured at selected sample voltages. Abrupt current fluctuations occured. The example shown was recorded at $V = 1.5\,\mathrm{V}$ and reveals four distinct current levels indicated by dashed lines. The lowest level is observed on all-*trans* TPAPA. Increasing levels reflect 1, 2, and 3 switched azobenzene subunits.

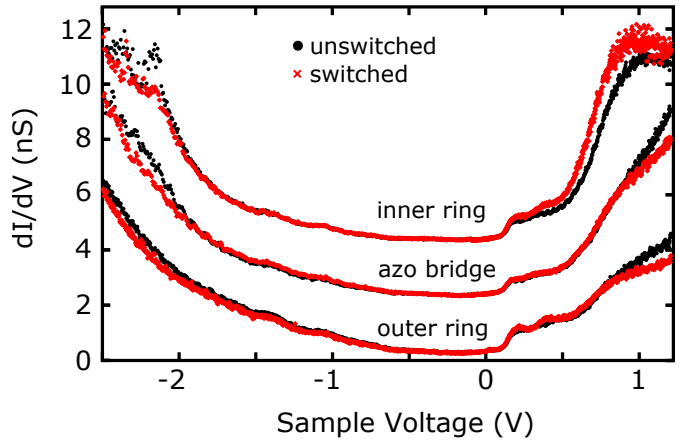

Figure 3.5: Differential conductance (dI/dV) spectra acquired above the inner and outer phenyl rings and the azo bridge of an AB subunit of TPAPA. Data was recorded from a pristine all-*trans* molecules and a switched isomer. Current feedback was opened at $V = -0.1\,\mathrm{V}$ and $I = 500\,\mathrm{pA}$. The spectra are vertically offset by 0, 2, 4 nS for clarity. The data indicate positive and negative ion resonances that vary little between the isomers.

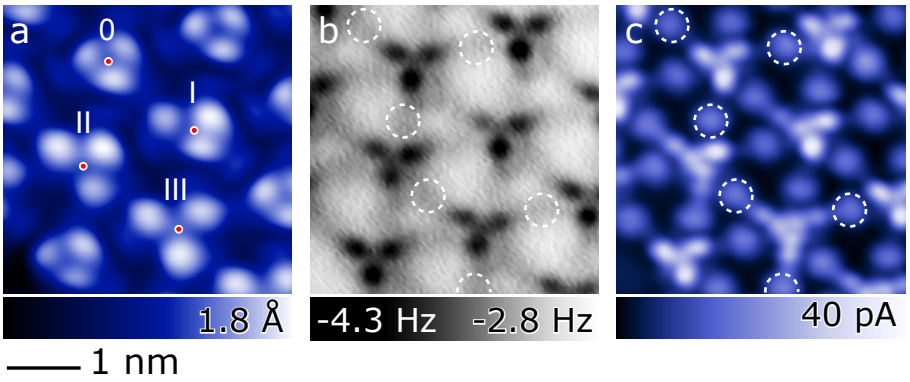

FIGURE 3.6: (a) Constant-current topograph (1 V, 100 pA). Molecules labeled **0** to **III** exhibit zero, one, two, and three switched AB subunits. (b) AFM frequency shift data from the same area measured at constant tip height. (Amplitude of cantilever oscillation 1 Å.) The positions of the outer rings are marked with dashed circles. While a significant frequency shift is found above inner pheny rings the outer rings and the azo bridge cause hardly any contrast. (c) Current map recorded at constant tip height from the same area.

experimental data, which suggests a much more subtle structural and electronic change upon switching.

Figure 3.6 (a) shows a constant-current STM image of molecules with varying numbers of switched AB subunits. Since constant-current STM images may be affected by electronic effects we performed additional measurements combining STM and non-contact AFM at sub-molecular resolution. Figures 3.6 (b) and (c) display AFM frequency shift data and a current map measured at constant tip height above the substrate. In the stable *cis* conformations identified via DFT (see Supplementary Information A.1.3), the outer phenyl rings are either strongly laterally displaced or switched to a tilted or almost vertical arrangement on the surface. These geometries are incompatible with the low contrast of the outer phenyl rings in the AFM data of Fig. 3.6 (b). Rather, these data indicate that the inner rings protrude farthest from the surface whereas the outer ones appear to lie rather flat. Based on the current map of Fig. 3.6 (c), where the outer rings, the inner rings, and the central amino linker form a straight line, this scenario can be excluded.

Another possible switching mechanism is a lateral shift of an outer phenyl ring. The outer phenyl rings can be either situated to the left or to the right of the plane defined by the azobenzene molecular axis and the surface normal. This reflects a handedness (denoted S and R, respectively) of the adsorbed AB subunits. DFT calculations yield metastable surface geometries for R and S conformers of an AB subunit of TPAPA. When the inner phenyl rings are twisted anticlockwise, the S configuration is minimally more stable. This higher stability is associated with a change in height of almost 0.6 Å of the N atom in the azo-bridge which is bound

to the inner phenyl ring. The corresponding isomerization reaction requires a torsional motion of the nitrogen atoms in the azo-bridge. We propose that this rearrangement involves a twisting motion of the central Nitrogen atoms around each other coupled with a lateral shift of the outer phenyl ring rather than a rotation that lifts the outer phenyl ring out of the surface plane. The calculated energy barrier height for this process is 0.47 eV. This value is consistent with the experiments where significant switching rates were observed at bias voltages of 0.8 V and above.

An out-of-plane rotation of a single phenyl ring has been reported from 3,3'-dicyanobenzene (di-meta-cyanobenzene, DMC) on Au(111) [134]. We do not favor this mechanism in the present case of TPAPA on Ag(111). According to our DFT+vdW$^{\mathrm{surf}}$ calculations it exhibits a significantly higher barrier due to the additional energy penalty of loosing the dispersion interactions between phenyl ring and surface.

The localized change in apparent height and tunneling conductance as observed in the STM can therefore be understood as a conformational switching from an S to an R state and a corresponding uplifting of the central azo-bridge at almost minimal lateral displacement of the phenyl groups. Much in accordance with the measured dI/dV curves, this conformational switching occurs with minimal modification of the energetic position of the molecular orbitals with respect to the Fermi level.

3.4 Conclusion

In summary, the three azobenzene units of the compound TPAPA on Ag(111) may each reversibly be switched between two distinct states. Switching is triggered by passing current through the center of a molecule or, to achieve selectivity, through the azo bridges. The efficiency of the process is comparable to molecular switching of AB derivatives that were decoupled from a Au substrate by spacer groups [11, 14, 125]. However, the switching does not involve the *trans* and *cis* isomers of AB that were predicted to lack of bistability on Ag(111). It rather involves a lateral motion of a phenyl ring and a twisting motion of the azo bridges. Thus the role of the Ag substrate is ambivalent. While it suppresses the original bistability of azobenzene it creates a new switching function that is based on surface-induced chirality.

Funding by the Deutsche Forschungsgemeinschaft through SFB 677 (K. Scheil, T. Gopakumar, J. Bahrenburg, F. Temps, and R. Berndt) and RE1509/16-2 (R. Maurer and K. Reuter) is acknowledged. Computing resources were provided by the Leibniz Supercomputing Center (LRZ), grant no. pr94sa. The authors furthermore thank Tugba Davran-Candan for support with initial electronic structure calculations. R. Maurer is grateful for discussions with Alessandro de Vita.

4

Adatom Coadsorption with Three-Dimensional Cyclophanes on Ag(111)

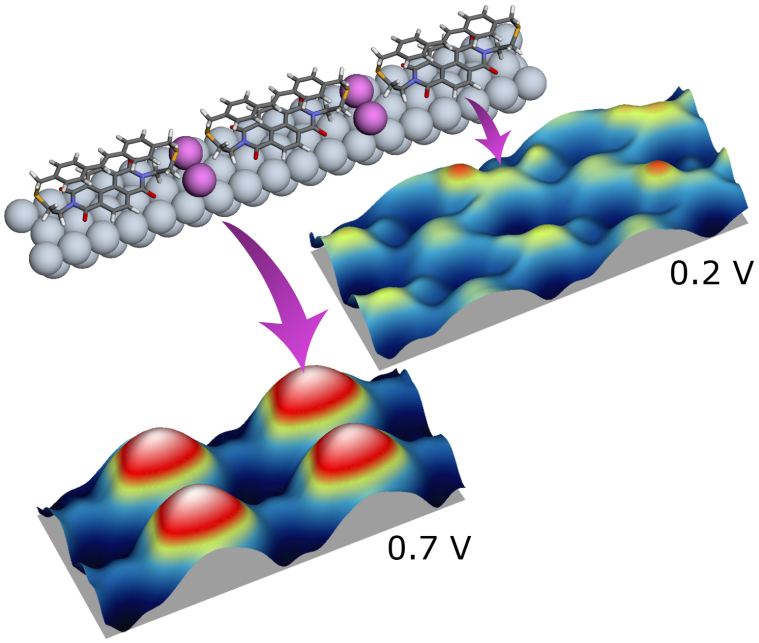

4.1 Introduction

The delicate balance among surface-adsorbate interactions leads to chemical properties of increasing complexity as new molecules on solid surfaces are explored [144–146]. An important aspect of surface functionalization is the effect of the adsorbed molecules on the surface structure of the substrate. Surprisingly profound modifications of the substrate may occur. For example, Cu-phthalocyanine induces facetting of Ag(110) surfaces [147]. The rather inert C_{60} fullerene can drastically affect the surfaces of coinage metals, which themselves are not very reactive. On Au(110), Ag(100), Au(111) and Cu(111), C_{60} removes substrate atoms and thus increases its coordination with metallic atoms [148–151]. Adsorbed molecules can bind to metallic atoms thus creating complexes. For example, thiols have been shown to be able to bind Au adatoms at gold substrates [152, 153]. Another example are the metal organic networks induced by surface adatoms [154–162]. Such effects are not limited to molecules with reactive end groups such as thiols. For example, ethylidyne (C_2H_3) is capable of producing a significant reconstruction of the Ru (0001) substrate [163], insulin alters the flat landscape of gold terraces [164], which also does pentacene [165].

The above examples highlight the important role of metal adatoms in the creation of adsorbed molecular networks. These adatoms are naturally present on the surface and minimize the system's free energy by coordinating with the molecules in a hierarchy of structures. Unfortunately, it can be very difficult to actually detect the presence of the adatoms themselves. Careful analysis of the structures is usually the only way to conclude on the presence of molecular-adatom interactions. Recent experiments [158] showed that the scanning tunneling microscope (STM) can help to reveal the presence of metallic adatoms. In Ref. [158], an adatom-related electronic state appeared in STM images recorded at elevated bias voltages. However, large biases are often not suitable when working with molecular structures because of the many undesirable processes that can be induced. Here, we show that changes of contrasts at a moderate bias can actually be the sign of the presence of adatoms.

We designed two similar molecules with a double-decker structure. The lower deck is the same in both molecules, and contains a naphthalene diimide (NDI) phane that generally adsorbs on noble-metal surface via dispersion interactions, and an upper deck, with either a stilbene or an azobenzene moiety. The two subunits are linked via alkyl sulfide groups, creating a three-dimensional building block. Due to this structure, the upper deck experiences little interaction with the surface. This type of molecule thus limits the interaction with the substrate to one of its subunits and is expected to preserve the functional properties of the other subunit. Dialkyl sulfides only physisorb on Au while thiols chemisorb [166] and

consequently the sulfide functions are not expected to cause the main molecule-substrate interaction. The molecules were adsorbed on a Ag(111) surface and a striking bias-dependent change of STM images was observed. By performing density functional theory (DFT) calculations and evaluating the adatom-induced changes of Gibbs free energy, we concluded that two Ag adatoms are coadsorbed between adjacent double decker molecules. These adatoms are responsible for the unusual image contrasts.

4.2 Methods

Both NDI-cyclophanes have been obtained by high-dillution macrocyclization conditions as displayed in Fig. 4.1. The precursor bis-*N*,*N*'-(2-(methyldisulfanyl)-ethyl)naphthalenediimide **1** was obtained by condensing naphthalene-tetra-carboxylic dianhydride with a fivefold excess of 2-(methyldisulfanyl)ethan-1-amine, which was synthesized according to a reported procedure [167]. Reducing the disulfides of **1** with tributylphosphine in a methanol/THF mixture provided the bis-*N*,*N*'-(2-mercaptoethyl)naphthalene-diimide **2**, which was used as crude compound without separation from the tributylphosphine oxide. The stilbene and the azobenzene subunits functionalized with terminal benzylic bromides **3** [168] and **4** [169] have both been reported. For the high dilution cyclization reaction, a 500 μM solution of **2** and **3** in 1,3-dimethyl-2-imidazolidinone (DMI) was treated with an excess of potassium carbonate (K_2CO_3) and heated to 60°C for 17 h. The desired NDI-stilbenophane was isolated by column chromatography (CC) and subsequent gel permeation chromatography (GPC) as an orange solid in 9 % yield. Applying a similar strategy, a 332 μM solution of **2** and **3** in *N*,*N*-dimethylformamide (DMF) was prepared, treated with an excess of K_2CO_3, and heated to 75°C for 16 h. Again, isolation by CC and GPC provided the NDI-azobenzenophane as a yellow solid in 17 %. Both cyclophanes were fully characterized by ^{1}H and ^{13}C NMR spectroscopy, high-resolution mass spectrometry, infrared and UV/Vis spectrometry and melting points.

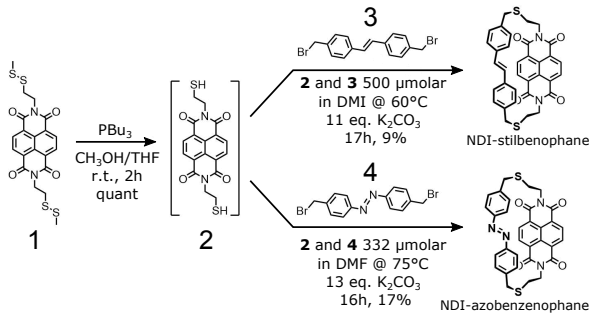

Figure 4.1: Syntheses of the two target structures NDI-stilbenophane and NDI-azobenzenophane.

The experiments were carried out with a combined scanning tunneling microscope (STM) and atomic force microscope (AFM) operated in ultrahigh vacuum at $\approx 5\,\mathrm{K}$. Ag(111) surfaces were cleaned by alternating cycles of Ar^+ ion bombardment and annealing. Both types of NDI-cyclophane were degassed and subsequently sublimated at $\approx 200°\mathrm{C}$ in ultrahigh vacuum from a Ta crucible onto the Ag(111) substrate, which was kept at ambient temperature. Submonolayer coverages of $\approx 10\,\%$ were typically used. Tips were etched from W wire and prepared in-situ by repeatedly indenting them into the clean areas of the substrate. To measure dI/dV spectra with a lock-in amplifier a sinusoidal modulation of $5 - 10\,\mathrm{mV_{rms}}$ at $4\,\mathrm{kHz}$ was added to the sample voltage.

Ab initio calculations have been performed in the framework of density functional theory as implemented in the VASP code [170]. We have used the PBE form of the generalized gradient approximation for the exchange and correlation functional [140]. Dispersion interactions have been treated using the method by Tkachenko and Scheffler [171]. The atomic position of the two topmost layers, the adatoms, and the molecules were relaxed until forces were smaller than $0.02\,\mathrm{eV/Å}$. The STM images were simulated using isocontours of the electronic local density of states [62, 172].

4.3 Results and Discussion

Figures 4.2 (a) and (b) show schemes of the molecules synthesized for this work, NDI-stilbenophane ((*E*)-1((2,7)-benzo[*lmn*][3,8]phenanthroline-1,3,6,8-(2*H*,7*H*)-tetraona)-6((4,4')-1,2-diphenylethena)-4,8-dithiadecanodane) and NDI-azobenzenophane ((*E*)-1((2,7)-benzo[*lmn*][3,8]phenanthroline1,3,6,8-(2*H*,7*H*)-tetraona)-6((4,4')-1,2-diphenyldiazena)-4,8-dithiadecanodane) [173]. Their syntheses are detailed in the *Methods* section. Densely packed islands of these molecules were prepared by sublimation onto Ag(111) surfaces at ambient temperature. STM data recorded at low temperature (5 K) reveal NDI-stilbenophane and NDI-azobenzenophane islands with similar electronic and geometric properties on the Ag(111) surface. The molecules arrange in a nearly rectangular ($86° \pm 5°$) unit cell, the long axis of which is aligned along a compact direction of the Ag(111) substrate as can be seen in constant-current STM images in Fig. 4.2 (c,d). The measured unit cell dimensions of $(1.8 \pm 0.2)\,\mathrm{nm}$ and $(1.0 \pm 0.2\,\mathrm{nm})$ are compatible with a commensurate $(6 \times 2\sqrt{3})R30°$ molecular lattice on the Ag (111) substrate.

STM topographs recorded at sample voltage V exceeding $\approx 0.6\,\mathrm{V}$ exhibit rows of oval protrusions (Fig. 4.2 (c,d)). At first glance, these predominant features seem to correspond to the bulky NDI-stilbenophane and NDI-azobenzenophane molecules. However, the appearance of the islands in topographs critically depends on V. For V below $\approx 0.4\,\mathrm{V}$ the topographs reveal features of submolecular dimensions (Fig. 4.2 (e,f)). Cross-sectional profiles of the NDI-stilbenophane

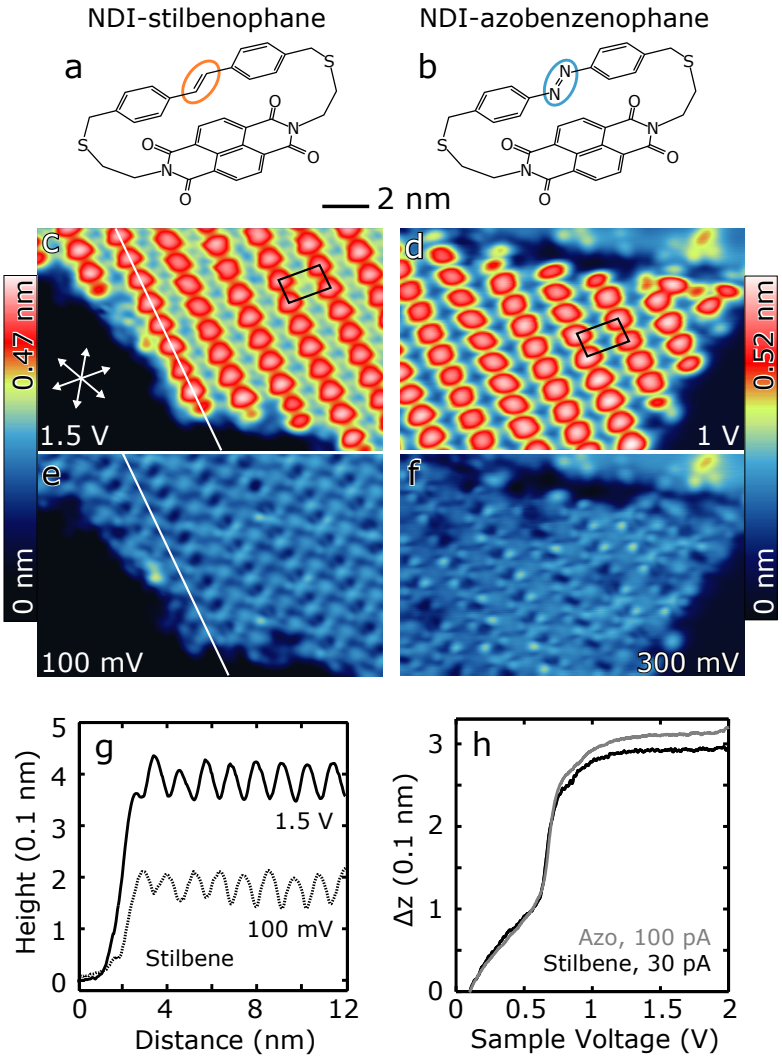

Figure 4.2: Lewis structures of (a) NDI-stilbenophane and (b) NDI-azobenzenophane. Constant-current topographs of (c, e) NDI-stilbenophane ($I = 70\,\mathrm{pA}$) and (d, f) NDI-azobenzenophane islands ($I = 20\,\mathrm{pA}$) on Ag(111) measured at characteristic sample voltages indicated on the images. While the topographs are very similar for NDI-stilbenophane and NDI-azobenzenophane, they vary drastically with the sample voltage. Rectangles mark unit cells. Arrows indicate the compact directions of the substrate, which are identical in all topographs. (g) Cross-sectional profiles along the lines in (c) and (e). (h) Retraction Δz of the tip with sample voltage V at constant-current. Black and gray lines show data from NDI-stilbenophane and NDI-azobenzenophane, respectively, measured above a corner of the unit cells.

data show that the apparent height maxima at low bias fall onto minima at high bias (Fig. 4.2 (g)). The same effect occurs for NDI-azobenzenophane (not shown). Moreover, a drastic change in apparent height by approximately 0.2 nm occurs as the bias is increased from 0.5 to 1.5 V. Figure 4.2 (h) shows this effect in more detail. The retraction Δz of the tip was measured as a function of V in constant-current mode. The abrupt rise of Δz signals that an additional state is accessible for tunneling as V increases beyond ≈ 0.6 V. Below that voltage, the molecules contribute little to the tunneling current despite their significant dimensions.

Changes of intralayer corrugation with bias have been reported in different situations [174, 175]. For single molecules, a corrugation change with bias was reported that disappeared when molecules dimerized [174]. This is clearly not the case here, where the corrugation change happens for the high-coverage case. Another case was due to picking-up oxygen atoms by the STM tip [175]. In our case, the tips are metallic and no change of the tip composition was detected. Moreover, all changes were reversible and exhibited no hysteresis with respect to changes of V. The above facts raise two intriguing questions: (*i*) Where are the molecules in these images? (*ii*) What is the origin of the change of contrast?

To address the first question, Fig. 4.3 (a–d) show the voltage-dependent patterns in more detail. Oval protrusions dominate the topographs at elevated voltage, but are absent at lower voltage in favor of submolecular features. We suggest that the low-bias structures reflect the position of the molecules whereas the oval observed at higher V is located between the molecules. This counterintuitive interpretation was initially motivated by the image contrast at occasional defects in the islands. Figure 4.3 (e) shows a typical example with the defect appearing as a hole (dashed ellipse). This one and all other hole-type defects were found at equivalent positions in the molecular pattern, where they replace topographic maxima of the low-bias pattern.

Non-contact atomic force microscopy (AFM) further corroborates this assignment. Figure 4.3 (f) shows AFM frequency-shift data measured at constant tip height above the same area as in Fig. 4.3 (e). Pairs of well-defined dots with a negative frequency shift are observed on a submolecular scale. These features occur at the positions of the low-bias maximum in constant current topographs. At the defect (dashed), no significant frequency shift is observed. In addition, the distance between the dots matches the separation of the phenyl rings of stilbene as indicated by the overlaid sketch.

The above observations lead to the conclusion that the low-bias protrusions mark the position of the molecules. Comparison with previous experiments [32, 176] of a molecule comprising two identical NDI subunits shows constant current images distinctly different from the present ones; see the Supplementary Information A.2. With respect to present cases of NDI-stilbenophane and NDI-azobenzenophane, this additional piece of information shows that the NDI subunit is indeed adsorbed to the substrate rather than facing the STM tip.

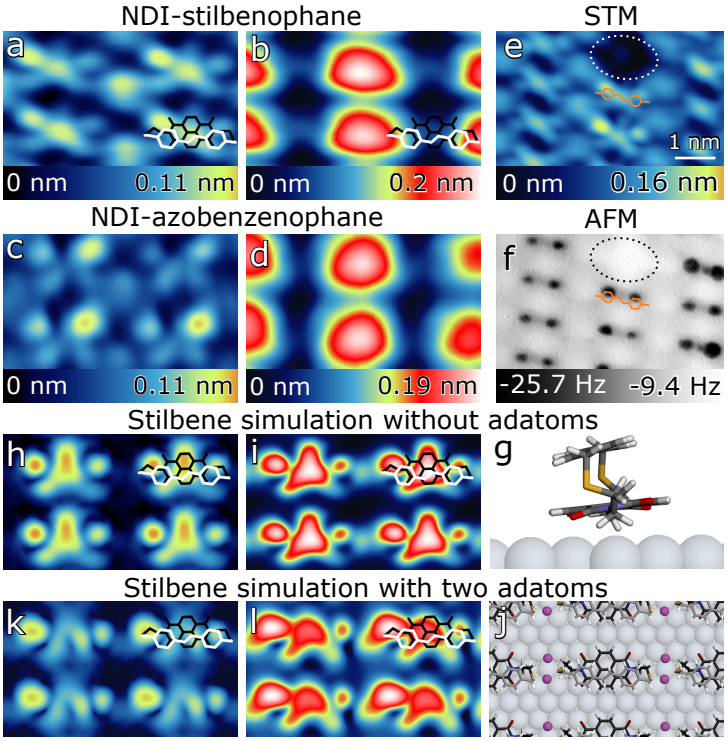

Figure 4.3: (a, b) Constant-current topographs of an NDI-stilbenophane island recorded at (a) $V = 0.2\,\mathrm{V}$, $I = 30\,\mathrm{pA}$ and (b) $V = 0.7\,\mathrm{V}$, $I = 109\,\mathrm{pA}$. Models of the calculated molecular structure are overlaid. (c, d) Topographs of an NDI-azobenzenophane island measured at (c) $V = 0.2\,\mathrm{V}$, $I = 59\,\mathrm{pA}$ and (d) $V = 0.6\,\mathrm{V}$, $I = 57\,\mathrm{pA}$. (e) Topograph of an NDI-stilbenophane island with a defect indicated by a dashed ellipse. $V = 0.1\,\mathrm{V}$, $I = 30\,\mathrm{pA}$. (f) AFM frequency shift measured at constant height over the same area as (e) with an oscillation amplitude of $A = 0.11\,\mathrm{nm}$. From the initial tip–sample distance defined by the set point $V = 100\,\mathrm{mV}$ and $I = 30\,\mathrm{pA}$, the tip was brought closer to the sample by 80 pm. Phenyl rings cause circular areas of more negative frequency shift. A minor shift is observed from the defect area. (g) Side view of the optimized geometry of NDI-stilbenophane with the NDI platform toward Ag(111). (h, i) Simulated topographs of NDI-stilbenophane at low and high bias without adatoms. (j) Top view of the optimized geometry of NDI-stilbenophane layer intercalated with two adatoms per molecules. (k, l) Like (h) and (i) but with adatoms between adjacent molecules.

To confirm this interpretation and to conclude on the origin of the bias-dependent contrast, density functional theory (DFT) calculations were performed (see Methods Section 4.2 and Supplementary Information A.2).

We obtained the optimized molecular-surface geometry displayed in Fig. 4.3 (g). The NDI subunit binds to the surface mainly via dispersion interactions with some *dative* contribution from local interactions [177]. Indeed, among the many possibilities to orient the molecule on the surface, an alignment along the high-symmetry direction is preferred due to a minimization of the four O–Ag

separations. Figure 4.3 (g) also shows that the O atoms are slightly bent out of the NDI plane to approach the Ag surface.

This configuration is further validated by comparison with the experimental STM images. We approximate the constant-current images by isocontours of local density of states (LDOS) at finite energies [62, 172]. Our simulated images compare well with the experimental ones at low bias (below 0.4 V) when the conformation depicted in Fig. 4.3 (g) is used. However, as the LDOS are plotted at larger bias (i.e., energy from the Fermi level), the agreement deteriorates (Fig. 4.3 (i)). Moreover, the change in corrugation from the molecules to the interstitial region at ≈ 0.6 V is not reproduced.

Careful examination of the experimental images (Fig. 4.3 (a–d)) shows some structure between the molecules whose apparent height increases as V is ramped up. This may suggest the presence of adatoms between the molecules.

Our total energy calculations predict that adatoms stably coexist with the molecular layer. We performed a thermodynamic study of the Gibbs free energy as a function of the chemical potential of metallic atoms. To that end, we assumed that Ag adatoms can exist on some part of the surface and that they are in equilibrium with the molecular layer. Hence, the adatoms will enter the molecular layer for chemical potentials comparable to that of the adatom. We considered three distinct phases: (*i*) the molecular layer corresponding to no adatoms, (*ii*) the molecular layer with one adatom between the two S atoms of adjacent molecules, (*iii*) a second adatom, close to the previous one (see Fig. 4.3 (j)).

Figure 4.4 shows the resulting phase diagram. For a large set of chemical potentials around the adatom free energy, the Gibbs free energy of the system is minimal for a phase with two adatoms. In other words, our calculations predict that the phase with two adatoms is the most likely one to be found under the experimental conditions. Adding a third adatom leads to considerable molecular distortion, and hence, it is not favorable for a large range of chemical potentials. Ag ions are known to form complexes with macrocyclic thio crown ethers [178–180]. The present case of dialkyl-sulfides appears to be related. On a Ag(111) substrate, the charges of the substrate and a Ag adatom are redistributed to enhance the bonding of the adatom [181]. As a result, the adatom carries a positive charge mimicking a Ag(I) ion. This scenario is different from the adatom–thiol binding on gold surfaces [152, 153] where the thiol ending presents a radical S atom due to the loss of the apical H atom from the molecule.

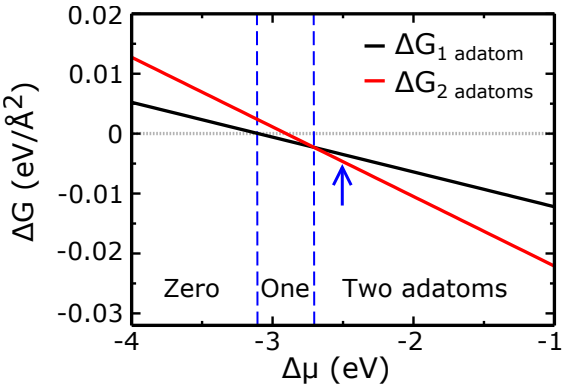

Figure 4.4: Change in Gibbs free energy ΔG as a function of the change in the Ag chemical potential $\Delta\mu$. Black and red lines correspond to the Gibbs free energy for one and two adatoms coadsorbed with the molecular layer. Three regions, which are separated by dashed lines, can be discerned in this graph: Zero adatoms are expected where the change in Gibbs free energy becomes positive if adatoms are added, a one-adatom region where the change in free energy minimizes for one adatom, and the two-adatom region where the free energy minimizes for two adatoms. If we assume that the source of adatoms is single adatoms on the clean surface, the equilibrium will be reached close to $\Delta\mu \approx -2.52\,\mathrm{eV}$ (blue arrow) as corresponds to the adsorption energy of single adatoms. However, the chemical potential will shift to lower (absolute value) energies as soon as the source of adatoms is instead edges of steps or islands. Hence, the graph shows that the minimun free energy at the system's chemical potential corresponds to the two-adatom phase.

Our calculations thus lead us to conclude that the studied molecular layer is a hybrid system comprising adatoms and molecules. The driving force for the integration of adatoms is the affinity of the S-terminated edges of the molecule for electrons that enables a directional, *dative*-like bond and the adatom–atom interaction that facilitates the adsorption of the second adatom.

Finally, we address the peculiar voltage-dependent changes of contrast in constant-current STM images. More detailed experimental information is available from spectra of the differential conductance dI/dV, Fig. 4.5 (a) and (b) for NDI-stilbenophane and NDI-azobenzenophane, respectively. Spectra were recorded on (orange) and between (black) molecules. Overall, the results from both molecules are very similar. This is not naively expected because the calculated HOMO-LUMO gap for NDI-azobenzenophane is 340 meV wider compared to the gap of NDI-stilbenophane. This suggests that the predominant contribution to the current is carried by a structural element that is common to both molecules. The on-molecule spectra reproduce the main features of the off-molecule data, namely, a sequence of equidistant peaks starting with a sharp rise at 0.5 V. We attribute these features mainly to vibronic excitations [32]. The

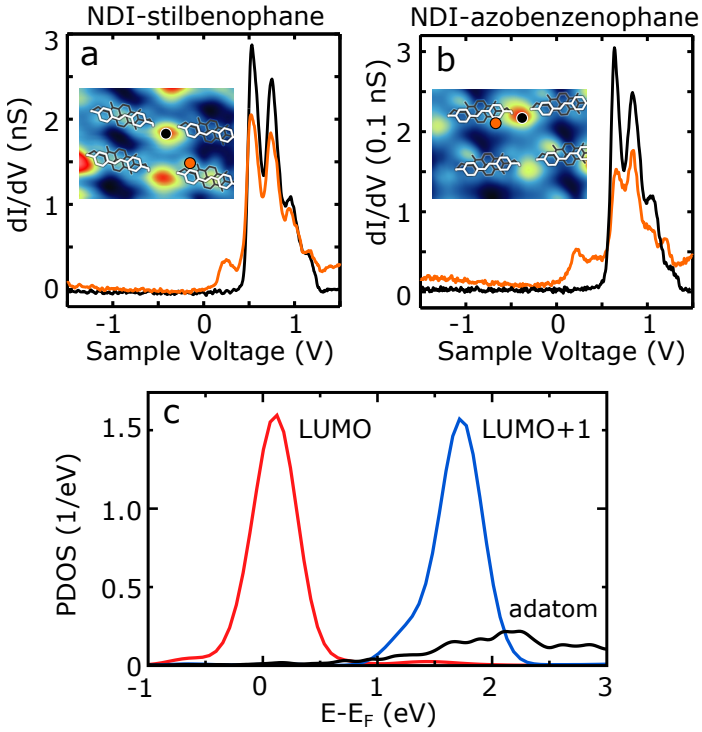

FIGURE 4.5: (a) dI/dV spectra of an NDI-stilbenophane molecule. Current feedback was opened at $V = 1.5\,\mathrm{V}$ and $I = 1\,\mathrm{nA}$. Colored dots in the topograph shown as an inset indicate the positions of measurement. (b) The same type of data as in (a), measured on NDI-azobenzenophane with the feedback opened at $V = 1.5\,\mathrm{V}$ and $I = 0.1\,\mathrm{nA}$. Above the molecules (orange curves), a rapid rise of dI/dV the onset starts near zero bias in agreement with the calculated energy of the LUMO. At interstial sites (black curves), the rise occurs at larger voltages that match the adatom-induced states displayed in (c). All spectra exhibit a series of approximately equidistant vibronic excitations, which are particularly clear at the interstitial sites. This signal is attributed to the excitation of wagging CH_2 modes. (c) Density of states projected on the indicated molecular orbitals of NDI-stilbenophane (red and blue) and on two adatoms (black).

sharp rise is consistent with the rapid increase of apparent height at this voltage (Fig. 4.2 (h)).

For further analysis, it is important to keep in mind that the area between molecules appears $\approx 0.1\,\mathrm{nm}$ higher in constant-current images. On molecules, the tip consequently has to be brought closer by this distance to obtain a comparable conductance. In other words, the amplitudes of all features observed on the molecules are approximately 10 times smaller than those between molecules. The fact that the molecular spectrum essentially reproduces the data from interstitial positions may therefore simply reflect the strength and corresponding lateral extent of the latter signal. The only molecular feature that is not observed between the molecules is a small peak at $\approx 0.3\,\mathrm{eV}$.

The experimental observations are only partially reproduced by our calculations. This is largely a consequence of using the LDOS instead of a proper transport calculation to simulate the STM images. A direct comparison of the calculated density of states reproduces some of the observed features; however, transport effects, e.g., a weak electronic coupling of the upper subunit to the substrate, are not included in the numerical LDOS. According to the calculated projected density of states (PDOS), the LUMO is centered slightly above the Fermi level (Fig. 4.5 (c), red), in good agreement with the molecular feature observed at 0.3 eV in the dI/dV data. The LUMO is localized to the lower subunit of the molecule, which is consistent with its low conductance. By contrast, the LUMO+1 (blue) is localized to the upper subunit. Its energy matches the dominant spectral features in Fig. 4.5 (a) and (b) well. By contrast, the p_z states of the adatoms (black), which also extend far into vacuum, are directly coupled to the Ag(111) surface, and become the main conductance channel.

A simulated low-bias STM image of the structure with two Ag adatoms between the S atoms of adjacent molecules is shown in Fig. 4.3 (k). It reproduces the observed features (Fig. 4.3 (a) and (c)) quite well. A comparison of the image calculated for elevated bias (Fig. 4.3 (l)) with the corresponding experimental data (Fig. 4.3 (b) and (d)) is less favorable. Although features develop in the interstitial region, they are much less dominant than in the experimental images. The contrast in the calculated images is mainly due to the LUMO+1. It is localized to the upper molecular subunit and thus dominates the current in a Tersoff–Hamann description of the tunneling current. The lack of coupling to the substrate, however, is likely to drastically reduce its conductance.

4.4 Conclusion

In summary, adatom dimers are intercalated between NDI-stilbenophane and NDI-azobenzenophanemolecules adsorbed on Ag(111). Two adatoms are compatible with the balance of free energies on the surface, whereas three adatoms are unfavorable. The intermolecular location of these adatoms together with an adatom induced electronic state leads to a fairly sharp onset at 0.5 V in dI/dV spectra. At this voltage the corrugation maximum shifts from on top of the molecules to an interstitial position. The enhanced apparent height of the interstitial area is due to the presence of these intermolecular adatoms and their localized electronic state.

K. Scheil and R. Berndt acknowledge Deutsche Forschungsgemeinschaft for support via SFB 677. M.-L. Bocquet thanks the national computational center CINES, and TGCC (Grant 2016- [GENCI project: A0010807364]) for a computer grant. N. Lorente gratefully acknowledges support from the MINECO (Grant No. MAT2015-66888-C3-2-R) and FEDER funds. P. Hess and M. Mayor acknowledge financial support by the Swiss National Science Foundation, grant number 200020-159730.

5

Force Spectroscopy on Iron Tetraphenylporphyrin Molecules and Transfer of Cl Ligands

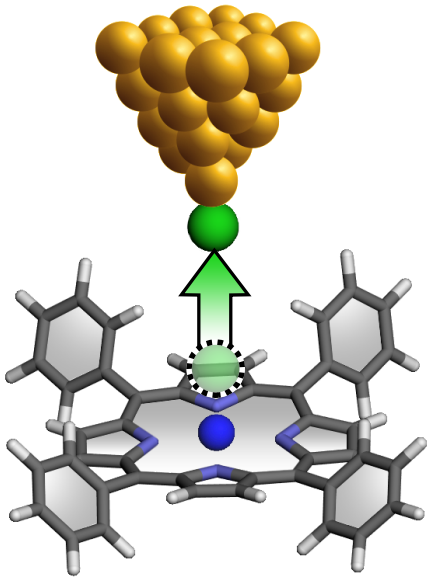

5.1 Introduction

The scanning tunneling microscope (STM) and atomic force microscope (AFM) have become powerful tools for the study of surface properties as well as manipulating structures on the atomic scale. Among various interactions between surface atoms and the probing tip, electrostatic interactions are important in scanning probe microscopy studies especially when charges are present. The role of electrostatic forces was demonstrated in the investigation of charged adatoms [83], quantum dots [182], defects [86, 183], and molecules [21]. In ionic systems atomic resolution is dominated by the electrostatic interaction between tip and surface ions [184–187]. Alternatively, the influence of charges in a junction with metal tip was accounted for in theoretical models [88, 89, 188–190]. Not only the ionic species at surfaces but also the tip termination was found to strongly influence the electrostatic interaction [85, 86]. Motivated by these findings it would be desirable to investigate the electrostatic interaction in a well defined junction with an experimentally adjustable charge configuration at the surface and the tip.

We chose iron tetraphenylporphyrin chloride (FeTPPCl) for the present study as it represents a model system composed of a platform (FeTPP) adsorbed on a surface, exposing a charged ligand (Cl) on its top. As demonstrated previously we can selectively transfer the charged ligand between the molecules and the tip of an STM by applying a proper voltage which is accompanied by a change of the molecule's oxidation state [47]. Here a combined STM/AFM was used to transfer the Cl ion from molecules to the tip and vice versa by performing force spectroscopy i.e. by approaching the tip towards the molecule while measuring the force. Thereby, four different well defined tip–molecule junctions were realized each offering a different charge configuration. Force spectroscopy data show strong dependance of the force on the position and number of charged ligands in the junction. The force is analyzed and compared with density functional theory (DFT) calculations and an electrostatic model.

5.2 Experimental Details

The experiments were performed with a combined scanning tunneling microscope (STM) and atomic force microscope (AFM) operated in ultra-high vacuum at $\approx 5\,\mathrm{K}$. Au(111) surfaces were prepared by Ar^+ ion bombardment and annealing. Tips were etched from W wire and prepared in-situ by repeatedly indenting them into the substrate. Therefore the tip apex was presumably coated with gold. Iron tetraphenylporphyrin chloride (FeTPPCl) (Fig. 5.1 (a)) was degassed and subsequently sublimated at $\approx 350\,^{\circ}\mathrm{C}$ from a Ta crucible onto the Au(111) substrate, which was kept at room temperature. Coverages of $\approx 10\,\%$ were achieved.

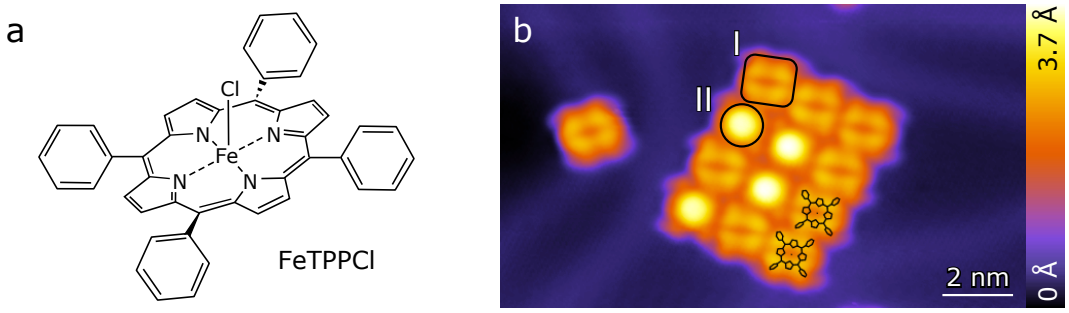

Figure 5.1: (a) Structural formula of FeTPPCl. (b) Constant current topograph (1.5 V, 26 pA) of a single FeTPP molecule and an island formed of FeTPP (**I**) and FeTPPCl (**II**) molecules. Scaled models of FeTPP are overlaid.

5.3 Transfer of a Cl Ion with the Tip of an AFM

When adsorbed to the surface, the molecules arrange in islands with a rectangular unit cell ($90° \pm 5°$) with the dimensions (1.4 ± 0.1) nm and (1.5 ± 0.1) nm. The long axis of the unit cell enclose an angle of $20° \pm 5°$ to a compact direction of the Au(111) substrate. Within the islands a mixture of FeTPPCl and iron tetraphenylporphyrin (FeTPP) occur (Fig. 5.1 (b)). The largest part of the islands is composed of FeTPP molecules (shape **I** in Fig. 5.1 (b)). The presence of FeTPP is due to a detachment of the Cl ligand occurring for parts of the porphyrin molecules during the preparation procedure [47, 191, 192]. Nevertheless, about one third of the molecules can be identified as FeTPPCl which appear as round protrusions (shape **II** in Fig. 5.1 (b)).

The sequence of constant current topographs shown in Fig. 5.2 (a–c) demonstrates the Cl ion removal and a subsequent redeposition to another molecule. After Fig. 5.2 (a) was acquired, the Au-tip was positioned at the center of FeTPPCl molecule **A** (dashed circle). The sample bias was lowered to a few millivolts and the oscillating tip was moved towards the molecule while the frequency shift and current were measured. A jump in the current and frequency shift suggested a change in the tip–molecule configuration. The detachment of the Cl ligand from the porphyrin was verified by a new STM topograph of the same area (Fig. 5.2 (b)). The molecule **A** now appears as the other FeTPP molecules. A slight change in contrast of the STM topograph and a tip retraction of 1 Å suggests the adsorption of the Cl ion at the tip. The procedure was then repeated with the Cl-decorated tip at the center of the FeTPP molecule **B** (solid circle). The appearance of a protrusion (Fig. 5.2 (c) position **B**) shows the redeposition of the Cl ion from the tip to a FeTPP molecule. The successful redeposition of the Cl ion to a molecule is further confirmed by restored contrast and a z displacement of the tip towards the surface by ≈ 1 Å.

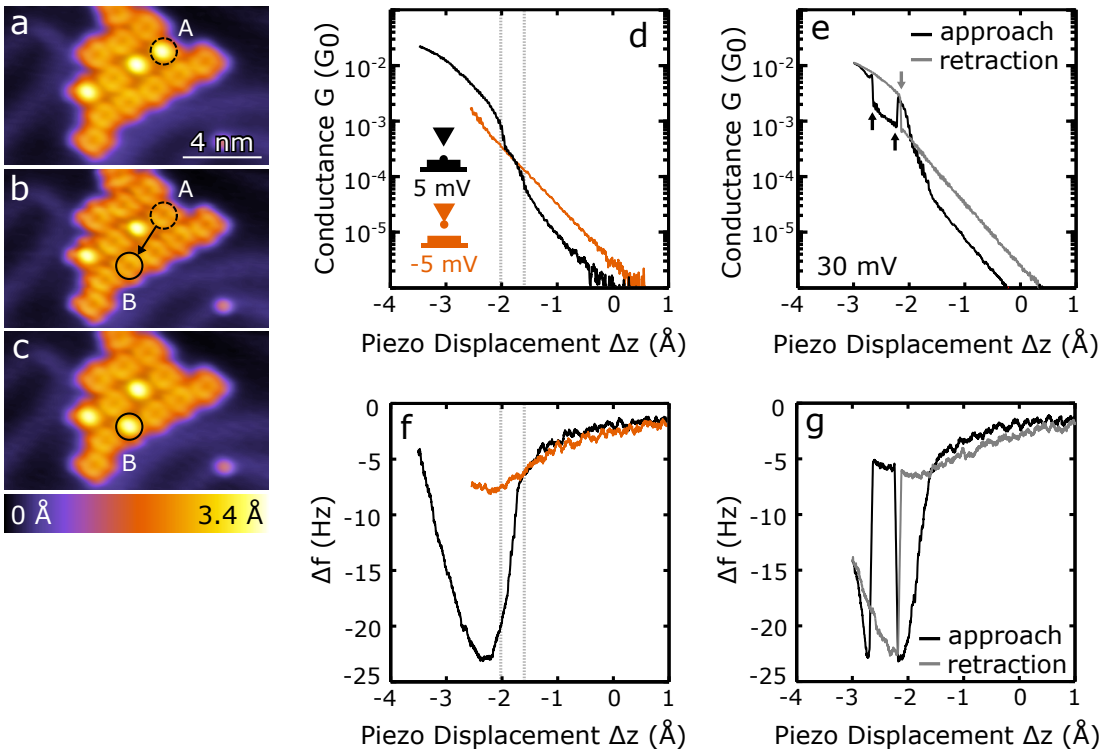

Figure 5.2: (a – c) Series of constant current topographs (1.5 V, 15 pA) of an FeTPP/FeTPPCl island. (a) The dashed circle labeled **A** indicates a FeTPPCl molecule. The tip was positioned at its center and the procedure to transfer the Cl ligand to the tip was performed. (b) Subsequently measured topograph of the same area. The dashed circle indicates the same molecule which has changed its appearance to a FeTPP molecule. The image contrast is slightly different compared to (a) which is attributed to the change of the tip apex which went along with the Cl ion transfer. To transfer the Cl ion from the tip to a molecule, the tip was positioned over the molecule marked by a full circle. The tip–molecule distance was progressively decreased and a jump in the current signal occurred. (c) The Cl ion was deposited to the marked molecule which therefore appears as a protrusion. (d) Averaged conductance (oscillation amplitude $A = 1.4\,\text{Å}$) as a function of the piezo displacement measured with the Cl ion located at the molecule (black, $V = 5\,\text{mV}$) and at the tip (orange, $V = -5\,\text{mV}$). The orange curve is shifted such that, at the same piezo displacement, the gold part of the Cl-terminated tip is at the same height over the substrate as that for the Au-tip. Sketches in matching colors illustrate the tunneling junction. Configuration $\Delta z = 0\,\text{Å}$ is defined by the STM set point $V = 250\,\text{mV}$ and $I = 15\,\text{pA}$ with a Au-tip over FeTPPCl. (e) Conductance measured during three Cl ion transfers (jumps indicated by arrows) at a sample voltage of $V = 30\,\text{mV}$. (f) and (g) Frequency shift measured simultaneously to (d) and (e), respectively.

Figure 5.2 (d) shows the conductance measured as a function of the piezo displacement during force spectroscopy with a Cl ion in the tunneling junction either adsorbed at a molecule (Cl_{mol}, black curve) or at the tip (Cl_{tip}, orange curve). Both configurations are illustrated by sketches in matching colors.

The conductance data differ depending on whether the Cl ion is located at the tip or the molecule. In both cases the conductance curves decay exponentially in the tunneling regime (for Δz close to 0) with increasing distance but the amplitudes differ. For the Cl ion on the molecule (black curve in Fig. 5.2 (d)) a deviation from the exponential dependence was observed at $\Delta z \approx -1.6\,\text{Å}$. A second jump in the conductance occurred at $\Delta z \approx -2\,\text{Å}$. These conductance jumps presumably originate from a displacement of the Cl_{mol} ion, when the tip gets close to the molecule. The detailed description of the mechanism is out of the scope of the present study. For the Cl-terminated tip (orange curve in Fig. 5.2 (d)) the conductance increases exponentially during tip approach almost over the entire investigated piezo displacement range. Indeed, a deviation starts to be visible only at $\Delta z \approx -2.4\,\text{Å}$. Furthermore, the deviation is smoother than that observed for the case of the Cl ion at the molecule. The comparison of the two cases suggests that the presence of a Cl ion at the tip lowers the attractive force between the tip and the molecule (see discussion below) as it leads to less abrupt changes in the conductance over distance curves (Fig. 5.2 (d)).

For the following discussion it is important to keep in mind that the conductance versus piezo displacement curves are specific to the considered systems configuration (Cl ion at the tip or at the molecule). These curves are highly reproducible. Nevertheless, occasionally measurements lead to curves depicted in Fig. 5.2 (e). The Cl ion was initially attached to the molecule. During the approach (black), the conductance curve exhibits two sharp jumps for piezo displacements of $\Delta z = -2.2\,\text{Å}$ and $\Delta z = -2.6\,\text{Å}$. In the retraction curve (gray), one jump is observed in the conductance for $\Delta z = -2.1\,\text{Å}$. Interestingly, the jumps are from a conductance characteristic of one configuration (e.g. Cl ion at the molecule) to a conductance characteristic of the other configuration (e.g. Cl ion at the tip). These jumps therefore indicate transfer events where the Cl ion switches from the molecule to the tip and vice versa. The Cl ion was at the molecule (tip) before (after) the measurement presented in Fig. 5.2 (e) as verified by STM topographs before and after the curves were recorded. During the conductance measurement a voltage of 30 mV was applied to the sample. The transfers from/to the tip are therefore observed at the same sample bias polarity. In a previous report by Gopakumar et al. [47] Cl ion transfers occurred at sample voltages above $\approx 0.85\,\text{V}$ and the transfer direction was found to be bias polarity dependent. A comparison of the present study with the one performed by Gopakumar et al. is discussed later in the text.

In the present study, the frequency shift (linked to the vertical force) was simultaneously measured as it provides further information. The position of the Cl ion in the junction has a large influence on the measured frequency shift.

Figure 5.2 (f) shows the frequency shift measured simultaneously to (d). The minimum of the curves develop at the same Au-tip height above the substrate. When the Cl ion is located at the molecule (black curve) the minimum shows a more negative frequency shift of $\approx 15\,\mathrm{Hz}$ and a steeper shape compared to the curve measured with the Cl ion attached to the tip (orange curve). A Cl ion transfer involves a jump between the two curve types as it can be seen in Fig. 5.2 (g) which was measured simultaneous to (e).

5.4 Characterization of the Cl-Terminated Tip

Since the interaction between the tip and the sample strongly depends on the Cl ion position in the junction, the short range forces of a Cl-terminated tip are considered first without the molecule. To remove the long-range forces, the often employed 'on-minus-off' method was used [91, 92]. The method consists of performing force measurements over two surface areas. One area is above the atom or molecule of interest. The other area is similar to the first one except for the absence of the atom or molecule. Since the substrate and the macroscopic part of the tip are the same in both cases a subtraction of both curves provides the short-range forces.

In order to retrieve the short-range electrostatic properties of the Cl_{tip} ion, curves with and without a Cl-termination were measured on pristine Au(111) substrate and subtracted. The resulting force (extracted from Δf versus Δz measurements following Ref. [75]) is shown in Fig. 5.3 (a) as a function of the tip height z. We used a spring constant of $1800\,\mathrm{N/m}$, as found in previous investigations for the qPlus-sensor [98, 100] and take into account an uncertainty of the force of 30 %. This uncertainty does not affect the comparison of force curves discussed later. The tip height z is defined as the center-to-center distance between the samples outermost atomic layer and the Au-tip apex atom (Fig. 5.3 (c)).

The relative variation of the height z is given by the piezo displacement. The absolute calibration is inferred from contact measurements of Au-tips over the gold substrate. The contact is assumed to occur at a height of $(2.88 \pm 0.3)\,\text{Å}$, corresponding to the distance between nearest neighbors in a Au crystal and the uncertainty of the contact determination.

The force characteristic of the Cl-terminated tip can be described by a point charge q in front of a conducting plate. In this scenario the force F_{img} on q follows Coulomb's law with an image charge $q' = -q$ in the conductor:

$$F_{img} = \frac{1}{4\pi\epsilon_0}\frac{qq'}{d^2}, \tag{5.1}$$

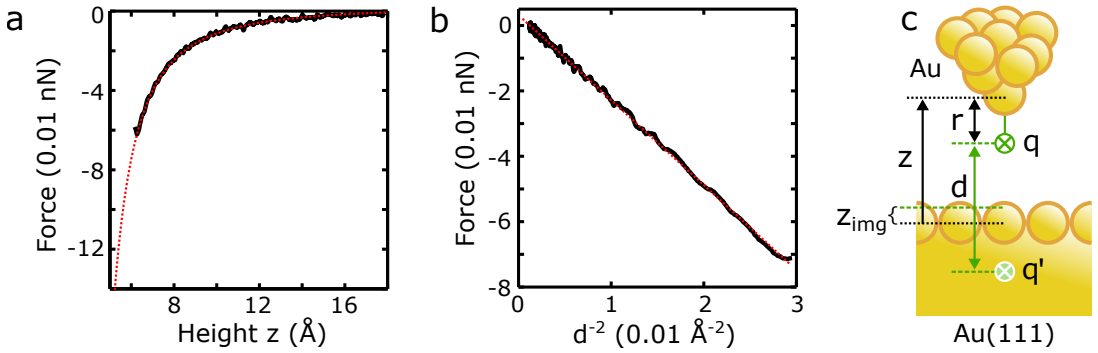

Figure 5.3: (a, b) Extracted force contribution of a Cl ion attached to the tip (black) as a function of (a) the height z of the gold part of the tip and (b) d^{-2} where d is twice the distance of the Cl ion to an electrostatic image plane depicted in (c). The red curves show the calculated force F_{img} (Eq. 5.1) due to a point charge of $q = 0.32\,\mathrm{e}$ positioned 2.3 Å underneath the tip. (c) Sketch of the Cl ion point charge q and its image q' in the tip–surface junction. $z_{img} = 1.0\,\text{Å}$ (from fit) above the outer most atomic layer, $r = 2.3\,\text{Å}$ (from DFT optimizations).

where d is the distance between q and q' or twice the distance of q towards the image plane (Fig. 5.3 (c)). The Cl ion is assumed to be at a distance of $r = 2.3\,\text{Å}$ under the last tip atom (from DFT calculations). Figure 5.3 (b) shows the linear curve progression of the measured short range force as a function d^{-2} for an electrostatic image plane located at $z_{img} = (1.0 \pm 0.3)\,\text{Å}$ outside of the outermost atomic layer (Fig. 5.3 (c)) in agreement with Refs. [193, 194].

A charge of $(0.32 \pm 0.05)\,\mathrm{e}$ is extracted from the slope. The charge uncertainty results from the uncertainty in force. A negative sign of the charge is assumed due to the high electronegativity of the Cl ion. The value is remarkably close to the charge obtained from a Bader charge analysis of a Cl-terminated gold tip of $-0.29\,\mathrm{e}$. The agreement between the measured force and the linear dependence of the force from the image charge model with d^{-2} is remarkable. It suggests that the simplified model considered here is enough to describe the physics of the system.[1]

5.5 Influence of the Cl Ion on the Tip–Molecule Force

With the reliable definition of the tip apex atom, i.e. a Cl- or Au-terminated tip, we consider FeTPP and FeTPPCl in the junction. The presence of two different molecules enables us to investigate four different tip–molecule configurations

[1]The force due to the interaction of the metal tips dipole with its image in the surface appears to be negligible. We estimated it to be at least a factor of 10 smaller in the region of interest than the force due to the Cl ion point charge for reasonable tip dipoles of 1 to 3 D [195].

which differ in the number and position of charged Cl atoms. The resulting vertical short-range forces are shown in Fig. 5.4 (a) as a function of the Au-tip height z. Sketches in matching colors indicate the tip–molecule configurations.

The tip height at which the maximal attractive force occurs is linked to the number of Cl ions in the tip–molecule junction. They change the effective distance from the molecule to the tip apex at a given height z. Without a Cl ion in the junction the effective tip–molecule distance is the largest of all four configurations. For this case, the maximal attraction occurs at the smallest tip height of the four curves (gray curve in Fig. 5.4 (a)). Unfortunately, for this specific configuration the force could not be measured to and beyond the maximal attraction since FeTPP was easily picked up by a Au-tip. Therefore the exact position of the maximal attraction is unknown.

When one Cl ion is located in a tip–molecule junction, either adsorbed at the molecule or at the tip, the maximal attraction occurs at the same tip height. The characteristics and magnitude of the force curves, however, differ drastically. A Cl-terminated tip leads to a maximal attraction of 0.24 nN. For the Cl ion located at the molecule the force is larger by a factor of ≈ 2.5 with 0.62 nN. In addition, the curve exhibits a steep progression of 0.4 nN in an interval of 0.4 Å (vertical lines in Fig. 5.4 (a)). When two Cl ions are located in the junction both at the tip and at the molecule a maximal attractive force of 0.19 nN is measured. The maximum of attraction develops at a ≈ 0.9 Å larger tip height compared to the configurations with one Cl ion in the junction. The shape of the force curve with two Cl ions in the junction differs significantly from the previously described cases since it exhibits a shoulder of reduced attraction ≈ 0.9 Å apart from the position of maximal attraction.

5.6 Density Functional Theory Calculations and Electrostatic Model

Density functional theory (DFT) calculations were performed by Dr. Martin Ondráček to describe the experimental findings. Details can be found in the Supplement A.3. The resulting force curves are shown in Fig. 5.4 (b). The difference in attraction for one Cl ion in the junction either at the molecule or at the tip is qualitative reproduced (compare black and orange curve in Fig. 5.4 (a) and (b)). However, the attraction is overestimated by a factor of two. Furthermore, the calculated force for two Cl ions in the junction is, in contrast to the experiment, purely repulsive. This might be caused by a restriction which was made in the calculation. Indeed, to reduce the computational cost, the geometries of FeTPP and FeTPPCl were first optimized at the surface in absence of a tip. The optimized geometries were then kept fixed and only Fe in the case of FeTPP and the Cl ligand for FeTPPCl could relax during the approach of the tip. At the

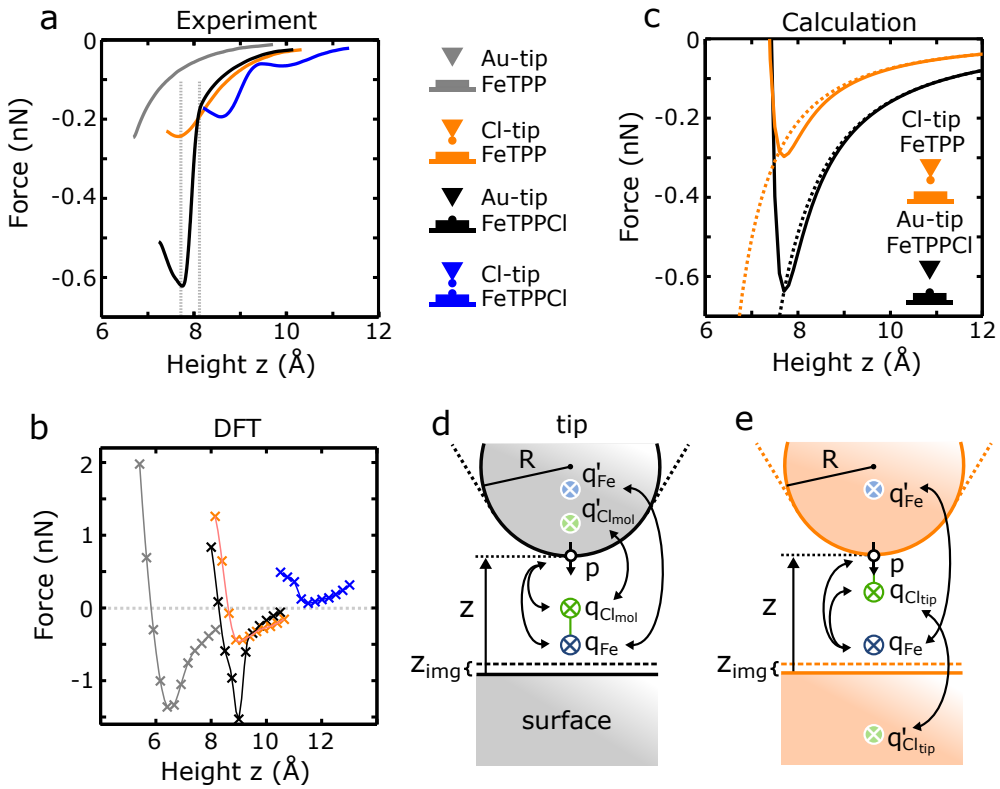

Figure 5.4: (a) Short-range force measured with the four tip–molecule configurations depicted by sketches in matching colors ($V = 10\,\mathrm{mV}$, $A = 0.85\,\text{Å}$) as a function of the tip height z. (b) Force extracted from DFT calculations. (c) Force calculated with a point charge model for one Cl ion in the tip molecule junction. The dashed curves contain the force components depicted by arrows in (d) and (e). For the solid curves a Lennard-Jones potential was added ($\epsilon = 4 \cdot 10^{-21}\,\mathrm{J}$, $r_m = 2.1\,\text{Å}$ for a Cl ion at the tip, $r_m = 2.3\,\text{Å}$ for a Cl ion at the molecule). (d, e) Model for one Cl ion in the tip–molecule junction ($R = 10\,\mathrm{nm}$, $p = 2\,\mathrm{D}$, $z_{img} = 1.0\,\text{Å}$) with the Cl ion at the molecule ($q_{Fe} = 0.65\,\mathrm{e}$, $q_{Cl_{mol}} = -0.56\,\mathrm{e}$) and at the tip ($q_{Fe} = 0.2\,\mathrm{e}$, $q_{Cl_{tip}} = -0.32\,\mathrm{e}$). Arrows indicate the electrostatic interactions that were taken in to account in (c).

pyramidal tip only the gold atom at the apex as well as the Cl termination were allowed to move.

Motivated by the point charge behavior of the Cl ion at the tip apex, we propose a simplified electrostatic model which reproduces the drastic difference of the force depending on the Cl ion position in the junction (solid curves in Fig. 5.4 (c) and sketches in Fig. 5.4 (d) and (e)). We modeled the tip–substrate junction with a conducting sphere and a plane surface. Point charges were positioned vertically aligned in the junctions to represent the porphyrin and the Cl ion. A Bader charge analysis of the adsorbed molecules [47] as well as dimensions of DFT optimized geometries were taken into account for the values and positions

of the point charges. FeTPPCl is represented by the averaged charge of the porphyrin base at the position of the Fe ($q_{Fe} = 0.65\,\mathrm{e}$, $z = 3.5\,\text{Å}$) and the Cl_{mol} ions ($q_{Cl_{mol}} = -0.56\,\mathrm{e}$, $z = 5.6\,\text{Å}$). The FeTPP molecule is modeled by one positive point charge ($q_{Fe} = 0.2\,\mathrm{e}$, $z = 3\,\text{Å}$). For the Cl-terminated tip we considered the experimentally determined negative point charge of $q_{Cl_{tip}} = -0.32\,\mathrm{e}$ positioned 2.3 Å under the sphere.

Furthermore a point dipole p oriented towards the surface is considered as it was shown that the tip apex of a metallic tip develops a small intrinsic dipole [84–86, 196–198]. A dipole value of 2 D (Debye) provides a good agreement of the total force with the experimental findings in accordance with Ref. [195].

Finally, both electrodes are assumed to be at the same potential in the model. During the experiments a voltage in the range of -30 to 30 mV was typically applied but variations of the voltage within this regime did not influence the measured frequency shift signal and were estimated to affect the calculated forces by less then 5 %.

The interactions indicated by arrows in Fig. 5.4 (d) and (e) are taken in to account in order to calculate the vertical force acting on the tip. The force between the Cl_{tip} ion and the molecule's point charge follow Coulombs law (analog to Eq. (5.1)). The interaction of the tip's dipole with the molecular point charges separated by the distance d results in a force [199]

$$F_p = \frac{1}{4\pi\epsilon_0}\frac{2qp}{d^3}. \tag{5.2}$$

When charges are located close to metals there is an image interaction due to charges induced in the conducting surface. In the present configuration both the tip and substrate were considered for the interaction with the introduced point charges [88, 89]. Only the direct interaction of a point charge q with its image charge q' located in the counter electrode was taken in to account. For a point charge located at the tip, F_{img} results as described in Eq. (5.1). The molecular point charges q induce images $q' = -qR/a$ in the spherical tip at the distance $b = R^2/a$ from the sphere's center towards the real charge, where a is the distance from the spheres center with radius $R = 10\,\text{nm}$. With this expressions we calculated the image force F_{img} due to a spherical electrode.

The sum of the enumerated force components are displayed as dashed lines in Fig. 5.4 (c). The tip is more attracted when the Cl ion is adsorbed at the molecule (black) compared to an adsorption at the tip (orange), which fits the experimental findings. This accordance suggest that electrostatic interaction plays a major role for the development of the force. In addition to the electrostatic force components

the force F_{LJ} due to a Lennard-Jones potential V_{LJ} between the closest tip and molecule atom at distance r was modeled and added with

$$V_{LJ}(r) = \epsilon \left[\left(\frac{r_m}{r} \right)^{12} - 2 \left(\frac{r_m}{r} \right)^{6} \right] \quad \text{and} \tag{5.3}$$

$$F_{LJ}(r) = -\frac{\partial V_{LJ}(r)}{\partial r}. \tag{5.4}$$

The depth of the potential well is modeled with $\epsilon = 4 \cdot 10^{-21}$ J in agreement with values found for Cl_2 molecules [200]. The position of the potentials minimum is $r_m = 2.1$ Å ($r_m = 2.3$ Å) for the Au-tip over FeTPPCl (Cl-tip over FeTPP) extracted from the Cl bond length in DFT optimized geometries of the Cl-tip (FeTPPCl).

The resulting total force curves are shown in Fig. 5.4 (c) (solid lines). A maximal attractive force of 0.29 nN for the Cl ion at the tip and 0.63 nN for the Cl ligand at the molecule are obtained, which is in relatively good agreement with the values found experimentally (deviation of 20 % and 3 %). However, the steep slope found experimentally for a Au-tip over Cl_{mol} ions (black curve, indicated by vertical lines in Fig. 5.4 (4)) is not reproduced by the model. The steep slope might be due to a displacement of the Cl_{mol} ion towards the tip during the approach [195]. The movement of the Cl_{mol} ion during the approach is corroborated by jumps in the conductance curves (compare black curve, indicated by vertical lines in Fig. 5.2 (d)). In addition, the Cl anion might be polarised during the tip approach [84]. Both effects may enhance the attractive interaction between the molecule and the tip and are not included in the model. Despite the rough approximation of the model, it nevertheless reproduces the experimental findings surprisingly well (Fig. 5.4 (c)).

However, the model does not reproduce the experimental findings for the configuration with two Cl ions (Fig. 5.5 (a)). The resulting total force (solid blue line), inferred from the model, is solely repulsive in contrast to the experimental findings (blue curve in Fig. 5.4 (a)). The force due to the Cl-Cl interaction (dashed green) leads to a very strong repulsive component compared to the attractive contributions (dashed blue). This raises the questions what causes the attraction of the tip and the development of the shoulder found in the experimental data.

A similar observation of an additional force minimum was made for force curves measured on platform mounted Zn-porphyrin molecules. It is explained by a slight bending of the molecule from an upright orientation in the junction under the influence of the tip [201, 202]. Furthermore, the CO functionalized tip apex is known to bend under the influence of lateral forces [203, 204]. Therefore a deformation of the Cl-terminated tip apex in the Cl-Cl configuration is likely. The data recorded here shows no hysteresis during approach and retraction of the tip.Thus an elastic deformation of the junction may occur. DFT optimizations of the Cl-terminated tip over FeTPPCl indeed suggest a sidewards displacement of the Cl ion at the tip during the approach as it can be seen in Fig. 5.5 (b).

Actually, the vertical Cl-Cl force component is lowered drastically when the Cl_{tip} ion performs a circular sidewards motion at small tip–sample separations (solid green line in Fig. 5.5 (a)).

Starting from these observations, we introduce a extended model which qualitatively reproduces the occurrence of a shoulder in the force curve for a Cl-terminated tip over FeTPPCl surprisingly well (solid blue curve in Fig. 5.5 (c)). The key point of the model is that the Cl_{tip} ion is allowed to rotate around the last gold atom of the tip while working against a spring as it is shown in the sketch in Fig. 5.5 (d). The energy U_{rot} stored in this rotation is modeled by

$$U_{rot}(\theta) = \frac{k_1\theta^2}{2} + \frac{k_2|\theta|^3}{3} \tag{5.5}$$

where θ is the angle of the rotation. The spring constants $k_1 = 463\,\mathrm{meV\,rad^{-2}}$ and $k_2 = 307\,\mathrm{meV\,rad^{-3}}$ are extracted from a fit to the change in energy ΔE obtained by DFT calculations of the deflected Cl_{tip} ion (Fig. 5.5 (e)). The DFT optimizations suggest only minor deflections of the Cl_{mol} ligand compared to Cl_{tip}, therefore its position was kept fixed in the model.

The energy due to the Coulomb interaction of the point charges at the tip $q_{Cl_{tip}}$ with the molecule $q_{Cl_{mol}}$ and q_{Fe} is considered with the potential

$$U_C(\theta) = \frac{q_{Cl_{tip}}}{4\pi\epsilon_0}\left[\frac{q_{Cl_{mol}}}{d_{Cl_{mol}}(\theta)} + \frac{q_{Fe}}{d_{Fe}(\theta)}\right], \tag{5.6}$$

where $d_{Cl_{mol}}$ (d_{Fe}) is the distance between the Cl_{tip} and Cl_{mol} (Fe) atoms. For each tip height the total potential energy $U_{total}(\theta) = U_{rot} + U_C$ was minimized as a function of the deflection angle θ. The angle with minimal energy is denoted θ_{min}. With the resulting deflection angles $\theta_{min}(z)$ (Fig. 5.5 (c), dashed gray curve) the vertical components of the force contributions depicted by arrows in Fig. 5.5 (d) were calculated. For a given tip height, the bending of the Cl_{tip} ion allows the repulsive Cl-Cl force component (green) to decrease, which brings it to the same order of magnitude as the attractive force components (dashed blue). In addition a Lennard-Jones potential was included ($\epsilon = 4 \cdot 10^{-21}\,\mathrm{J}$ and $r_m = 2.9\,\text{Å}$).

The force curve resulting from the model exhibits a shoulder at a tip height of $z \approx 11\,\text{Å}$ with a repulsion of $\approx 0.06\,\mathrm{nN}$. In the experiment the shoulder occurs at a tip height of $z \approx 10\,\text{Å}$ and features an attraction of $\approx 0.06\,\mathrm{nN}$. Even though the model is simple the resulting force curve matches the experimental findings surprisingly well. The main features in the shape of the curve are reproduced due to the included sidewards movement of the Cl_{tip} ion.

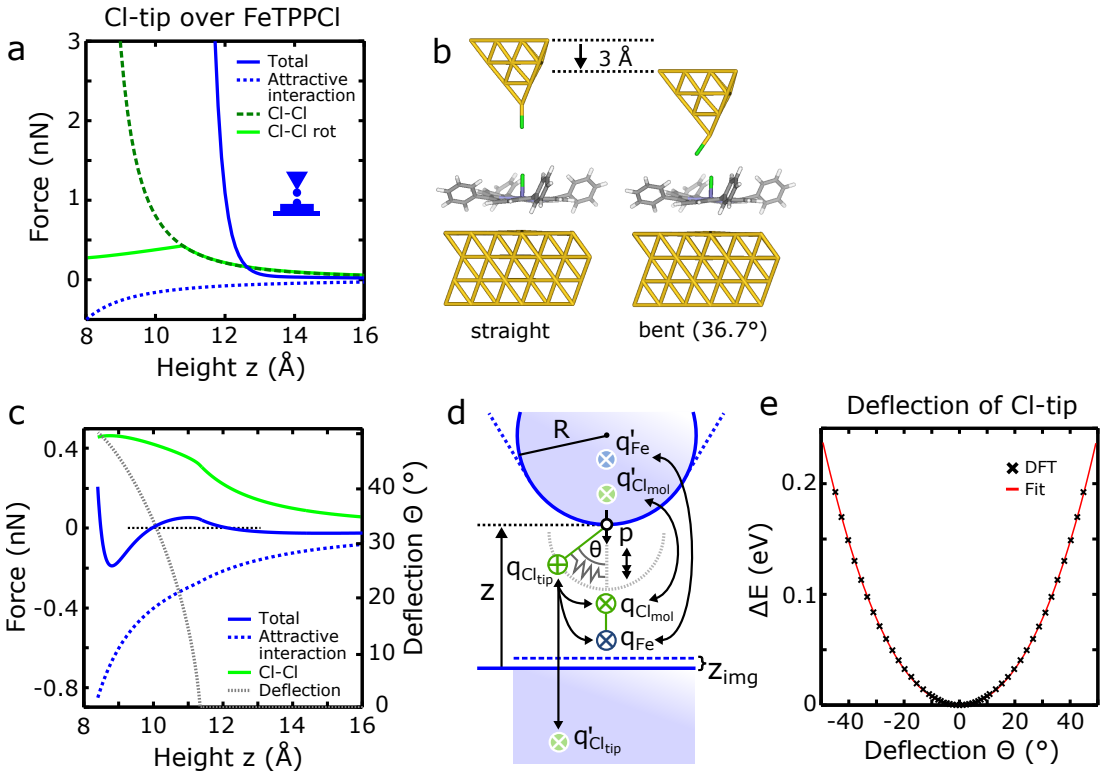

Figure 5.5: (a) Force components calculated for a Cl-terminated tip approaching FeTPPCl. In the total force (blue) the attractive (dashed blue), repulsive Cl-Cl (dashed green) and a Lennard-Jones potential describing Cl_2 molecules was included ($\epsilon = 4 \cdot 10^{-21}$ J, $r_m = 5.02$ Å) [200]. A rotation of the Cl_{tip} ion in order to follow a Cl-Cl distance of 2.9 Å at small tip–sample separations reduces the repulsive component (green). (b) DFT optimized geometries of a Cl-terminated pyramid-shaped Au tip over FeTPPCl with a straight and a bent Cl_{tip} ion (36.7°) at a tip height of 13 Å and 3 Å closer. (c) Calculated vertical force components and deflection angle for a free to rotate Cl_{tip} ion during the approach to FeTPPCl in a spring model (d). The attractive (dashed blue) and repulsive Cl-Cl (green) as well as a Lennard-Jones Potential ($\epsilon = 4 \cdot 10^{-21}$ J, $r_m = 2.9$ Å) is included in the total force (blue). (d) Sketch of the spring model. Arrows indicate the force contributions that were taken in to account in (c) ($R = 10$ nm, $z_{img} = 1.0$ Å, $p = 2$ D, $q_{Fe} = 0.65$ e, $q_{Cl_{mol}} = -0.56$ e, $q_{Cl_{tip}} = -0.32$ e). (e) Calculated change of energy as a function of the Cl_{tip} ion deflection angle θ from its equilibrium position and fit of $U_{rot} = k_1\theta^2/2 + k_2|\theta|^3/3$.

5.7 Estimation of the Force on the Cl Ligand upon Transfer

The STM induced Cl ion transfer experiments performed by Gopakumar et al. required a threshold voltage and the transfer direction was linked to the bias polarity [47]. To bring this observation in line with our findings we estimated and compared the electrostatic force components on the Cl_{mol} ligand upon transfer for both experiments. The short range forces are estimated using the previously described model (F_{SR}^{trans}). The Cl_{mol} ligand is further affected by the electric field developing between the tip and the sample. This electric field originates from the applied sample voltage V and the contact potential difference ($V_{CPD} \approx -650\,\mathrm{mV}$ with respect to the sample according to Δf vs V measurements). In a plate-capacitor model of the junction the force on the Cl_{mol} ligand is

$$F_E^{trans} = \frac{q_{Cl_{mol}}(V_{CPD} + V)}{z_{trans} - z_{img}}, \tag{5.7}$$

where z_{trans} is the tip–sample distance during the transfer. The total electrostatic force F^{trans} considered for the transfer of a Cl ion is the sum of F_{SR}^{trans} and F_E^{trans}. Upon Cl ion transfers from molecules to the tip, a total electrostatic force of ≈ 0.36–$0.61\,\mathrm{nN}$ is inferred for the present study and a force of $\approx 0.4\,\mathrm{nN}$ for the study of Gopakumar et al.

These similar forces suggest that the transfer mechanisms are similar. However the compositions of the total electrostatic forces are different due to different tip heights and sample voltages in the experiments.[2] Indeed, force components of $F_{SR}^{trans} \approx 0.28$–$0.56\,\mathrm{nN}$ and $F_E^{trans} \approx 0.08\,\mathrm{nN}$ were extracted in the present study whereas $F_{SR}^{trans} \approx 0.15\,\mathrm{nN}$ and $F_E^{trans} \approx 0.25\,\mathrm{nN}$ were inferred for the study of Gopakumar et al. Yet, if we consider that the Cl ion transfer occurs when a force threshold is exceeded, we have a common picture explaining the two experiments. In the present AFM study F_{SR}^{trans}, reached by an adequate tip–sample distance, is the relevant force component to induce the Cl ion transfer whereas a proper voltage strength and polarity is needed in Ref. [47].

5.8 Conclusion

In conclusion, we used force spectroscopy to induce the transfer of Cl ions back and forth between FeTPP molecules and the tip. With the Cl-functionalized tip, force spectroscopy was successfully performed. We showed that electrostatic interaction between the differently terminated tip and the sample plays a major role for the characteristic of the measured forces. In addition, the data suggests

[2] In the present study the tip was ≈ 1–$2\,\text{Å}$ closer during transfers and voltages of $\pm 10\,\mathrm{mV}$ were applied compared to ≈ -1.6 to $-1.8\,\mathrm{V}$ in Ref. [47].

the need of a minimal rupture force for the transfer of Cl ions. Additionally, it would be interesting to retrieve dynamic aspect e.g., by approaching/retracting the tip at different speeds or, at further tip–surface distance, to sweep the sample voltage at different speed. In the future, similar transfer experiments via force spectroscopy might be applied to other systems.

6

Summary and Outlook

In this thesis, three molecular systems on noble metal surfaces were investigated by means of combined low-temperature STM and AFM. The studies focus on switching, structural and electronic properties as well as forces in the molecular junctions. The outcome of these investigations contribute to a better understanding of atomic-scale processes in molecular systems on metallic surfaces. Such fundamental understanding is essential for chemical design of molecules with improved functionality.

In the first experiment, presented in Chapter 3, azobenzene based tris-[4-(phenylazo)-phenyl]-amine (TPAPA) molecules were found to be efficient switches on Ag(111). It was demonstrated that each of its three azobenzene subunits can be switched reversibly between two states by passing current through the molecule's center and even selectively by addressing the azo bridges. The adsorption geometry and electronic structure of the TPAPA isomers were investigated. STM topographs, constant height frequency shift maps, STS along with DFT calculations evidence that the switching process is no *trans–cis* isomerisation but rather a reorientation of the N–N bond of an azobenzene unit. It proceeds through a twisting motion of the azo bridge that leads to a lateral shift of a phenyl ring. This study shows the influence of molecule–substrate interaction on the molecule's functionality. The Ag substrate suppresses the original bistability of the azobenzene subunits but creates a new one based on surface-induced chirality. The role of the substrate on the switching behavior of TPAPA could be further investigated in future experiments by choosing more and less reactive surfaces than Ag(111) such as Cu(111) and Au(111).

In a second experiment (Chapter 4), two cyclophane molecules with a three-dimensional double-decker structure were investigated on Ag(111). Both molecules are designed to adsorb on the surface via a naphthalene diimide (NDI) platform and exhibit either a stilbene or an azobenzene moiety. Combined STM, AFM and DFT calculations yield complementary information from which the structure of self-assembled islands is deduced. STM topographs exhibit a drastic change in corrugation with the sample voltages similar for both types of molecules. Submolecular features, visible at low bias, reflect the molecule's position as inferred from investigations of occasional hole-type defects in the molecular pattern. Oval protrusions, dominating the topographs at elevated voltages, originate from coadsorbed Ag adatoms at interstitial positions. The study shows that the NDI-cyclophane double-decker structure can be employed to lift a functional unit from the substrate. This result motivates the investigation of further NDI-cyclophane molecules with varied functional moieties in order to achieve functionalized surfaces. Beside that, in future experiments the influence of intermolecular adatoms on the molecule's self-assembly and switching capability could be investigated. For that purpose, the hybrid network could be altered by changing the adatoms which connect the molecules either by choosing other surfaces or by depositing other atomic species onto the sample during the preparation process.

In a third experiment, presented in Chapter 5, iron tetraphenylporphyrin chloride (FeTPPCl) on Au(111) is used as a model system to investigate the electrostatic interaction in a well defined junction with an experimentally adjustable charge configuration at the surface and the tip. Four different tip–molecule junctions are realized by transferring the Cl ligand between FeTPPCl molecules and the tip of an AFM. The shape of force versus distance curves crucially depends on the position and number of charged ligands in the junction. In particular, the insertion of two charged ligands leads to an unusual non-monotonic force curve shape due to a tilting of the Cl ion at the tip. The force curves are reproduced by a model considering point charges in the tip–sample junction. From the model, we infer that the relevant forces arise mainly from electrostatic interactions. Finally, the analysis of several ligand transfer events suggests that the Cl ion is transferred to the tip by application of adequate electrostatic forces. In future experiments force spectroscopy in combination with a systematic change of the junction could be extended to other metalloporphyrin molecules. Beside changing the metal center also other ligands such as other halogens could be used to vary the charge composition in the junction. Porphyrin molecules with diatomic or other small ligands could also be utilized to investigate bond breaking and bond forming using force spectroscopy.

A Supplementary Information

A.1 Switching of an Azobenzene-Tripod Molecule on Ag(111)

A.1.1 Current Dependency of Switching Rate

Switching of the azobenzene (AB) subunits can be induced by passing current through the center of TPAPA molecules. Therefore, first the tip was positioned at the center of a molecule. Then current and voltage setpoints were chosen and the feedback loop was enabled. Time series of the current were acquired over a period of 5 min. The recorded series show abrupt current fluctuations between four levels (see Fig. 3.4 in Chapter 3) which correspond to the pristine molecule and the states with 1 to 3 switched AB subunits. Resulting switching rates are shown in Figs. A.1 (a) and (b) for several voltages as a function of the current setpoint.

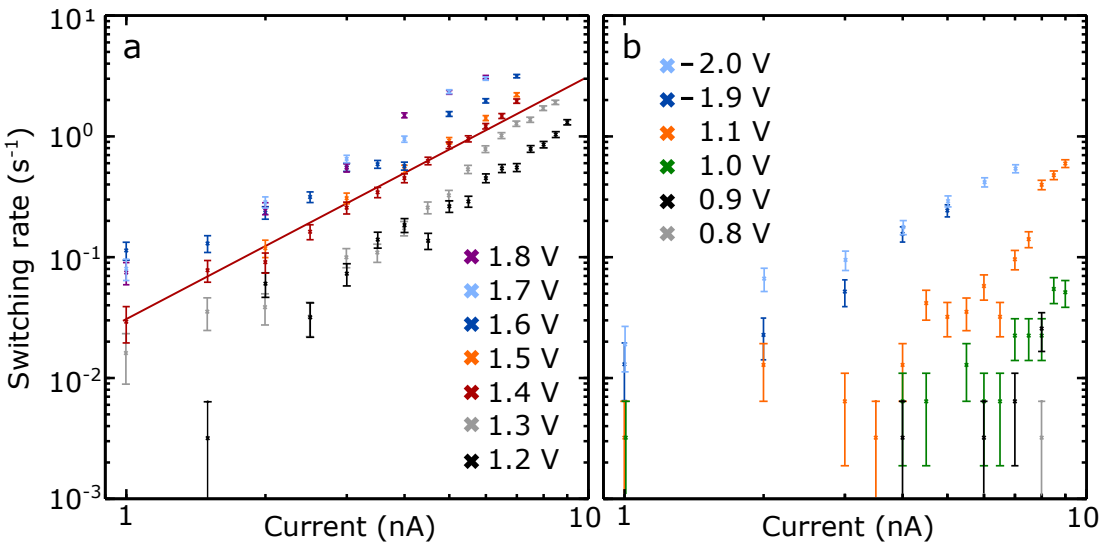

FIGURE A.1: Switching rate vs. tunneling current recorded over the center of TPAPA molecules with current feedback enabled. (a) At positive sample voltages exceeding 1.2 V the switching rate approximately follows a power law $\sim I^2$ (indicated by a line). (b) Switching also occurs at negative bias polarity ($V = -1.9$ and -2 V) with a similar power law. For low voltages no fitting has been attempted because of low numbers of switching events. However, apparently the rate varies more steeply with the current.

A.1.2 Lateral Shift of Phenyl within Islands

Switching the AB units results in a lateral shift of the topographic maxima due to the outer phenyl rings. At the island edges the shift is ≈ 1.5 Å. Inside islands, it is smaller as shown in Fig. A.2. Figures A.2 (a) and (b) show constant-current topographs of a molecule in an island before and after switching (dashed ovals). A difference image is displayed in Fig. A.2 (c) along with a model of the switched molecule. The lateral shift of the maximum related outer phenyl ring is only ≈ 1.0 Å.

At first glance, the different shifts of maxima seem to indicate different lateral motions of the phenyl rings. However, a more detailed analysis has to take into account the contribution of neighboring molecules to the tunneling current and, as a consequence, to the apparent heights in the topograph. To estimate this effect Figs. A.2 (d–f) from an island edge are used. Switching the molecule that has been overlaid with a white model in Fig. A.2 (e) leads to the state shown in Fig. A.2 (f). The orange models in e and f indicate where an additional molecule would be located if the image was taken within an island. The topographic contribution of such a molecule is estimated from Fig. A.2 (d), which shows a molecule in the proper orientation (orange model overlaid). Figure A.2 (g) presents cross-sectional profiles taken along the colored arrows in Figs. A.2 (d–f). The blue and red profiles show a shift of ≈ 1.5 Å. The orange one displays the expected background. Figure A.2 (h) is obtained by adding the background profile to the

red and blue data sets. As a result, the distance between the relevant maxima is reduced to ≈ 1.5 Å, which matches the result obtained from molecules within islands. In other words, the experimental data do not indicate different switching characteristics at edges compared to island centers.

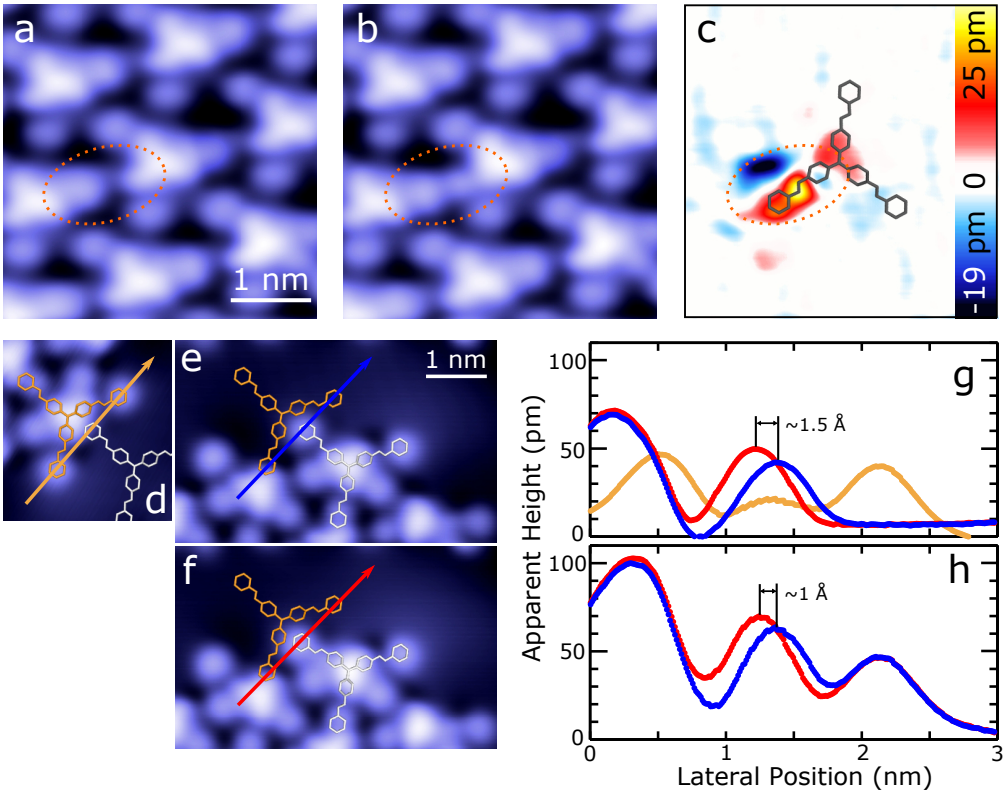

Figure A.2: (a, b) Constant current topographs (50 mV, 100 pA) of a TPAPA island. The molecule marked by dashed oval is switched. (c) Difference image obtained by subtracting image (a) from (b). A model of the switched molecule is overlaid. (d – f) Constant current topographs (20 mV, 100 pA) of molecules at island edges. Colored lines mark the positions where cross-sectional profiles were made. Models indicate the positions of molecules according to the packing within islands. (g) Profiles across the outer phenyl ring of an AB unit in the unswitched (blue) and switched (red) states. The orange profile was measured where an outer phenyl ring of a neighboring molecule would be located. (h) Profiles across the unswitched (blue) and switched (red) phenyl ring with background profile (orange in (g)) added.

A.1.3 Dispersion-corrected Density Functional Theory Calculations

Computational Details

Calculations were performed using the pseudopotential plane-wave code CASTEP 6.0.1 [142] with standard library ultrasoft pseudopotentials. We employ the exchange-correlation functional by Perdew, Burke and Ernzerhof [140] and the dispersion-correction scheme of Ruiz et al. (PBE+vdW$^{\mathrm{surf}}$) [116, 141].

Gas-phase geometries of TPAPA have been modeled in a rectangular (40 Å x 40 Å x 40 Å) supercell. For the adsorbed molecule a (6 x 6) surface unit cell containing four layers of Ag atoms with the optimal PBE lattice constant of 4.14 Å was used with a vacuum region that exceeds 20 Å. The corresponding lattice constants ($a = b = c = 1.76\,\mathrm{nm}$, $\alpha = \beta = 60°$) of this unit cell are close to the incommensurate surface unit cell found in experiment ($a = 1.8\,\mathrm{nm}$, $b = 1.6\,\mathrm{nm}$, $c = 1.7\,\mathrm{nm}$, $\alpha = 60°$, $\beta = 65°$). During all structure optimizations the Ag substrate was kept frozen in its bulk truncated structure.

A plane-wave cut-off value of 450 eV was employed in the surface calculations together with a Monkhorst-Pack 2 x 2 x 1 k-point grid, respectively. Geometry optimizations have been performed with a maximal force criterion of 25 meV/Å. Transition barriers have been calculated using the Nudged Elastic Band (NEB) method [205] using a maximum force tolerance of 50 meV/Å.

Molecular orbital projected density-of-states (MOpDOS) plots were generated by projecting the wavefunctions of the free molecule onto the wavefunctions of the substrate-adsorbate system. The eigenstate positions as reported in Table A.2 and Table A.3 are calculated as the average energy of each MO projected frontier orbital. Details can be found in works by Gopakumar et al. [130], Maurer and Reuter [119].

Results

We assume the experimentally observed "unswitched" TPAPA molecules (all-*trans*-TPAPA) on Ag(111) to arrange in symmetric islands with the Azobenzene-legs in *trans* configurations as it was also done for TPAPA adsorbed on Au(111) in a previous study [130]. Initial optimizations of all-*trans*-TPAPA on Ag(111) at different adsorption sites show that for the most stable geometry the central nitrogen atom is situated at the fcc-hollow site. All subsequent calculations have been performed with the molecule adsorbed at this site.

Figure A.3 shows the adsorption geometry of all-*trans*-TPAPA from the top and the side. The central N atom is positioned at the fcc-hollow site of the Ag(111) surface and the azo-bridges of the three AB legs are situated close to a bridge position, which is the most favorable adsorption site for single azobenzene

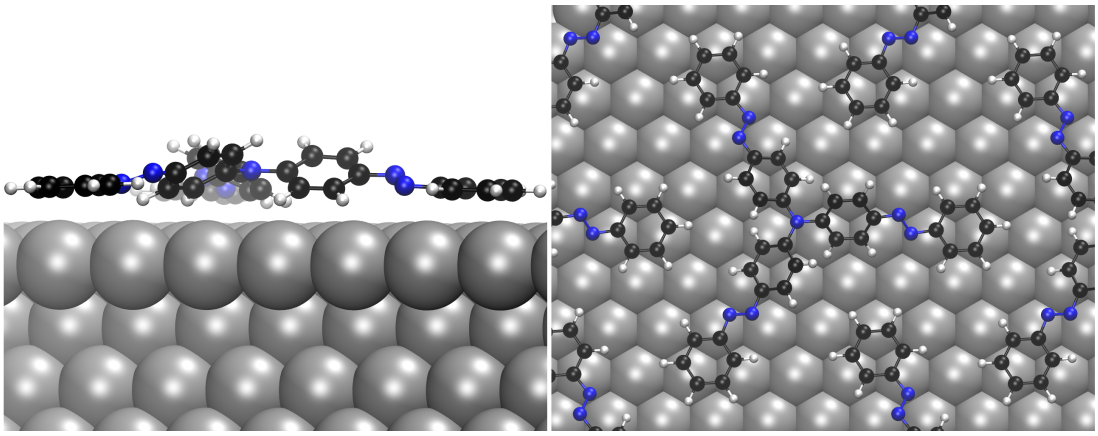

Figure A.3: Optimized structure of all-*trans*-TPAPA as viewed along the Ag(111) surface (left) and orthogonal to the surface (right). The inner phenyl rings are tilted due to sterical hindrance, the outer phenyl rings adsorb flat on the surface. Black spheres correspond to Carbon, blue to Nitrogen, and white to Hydrogen.

Table A.1: Relative energies of different TPAPA structures referenced to all-*trans*-TPAPA adsorbed on Ag(111). Additionally shown are the average values of the vertical adsorption heights of the azo-bridges and the central dihedral angles around the Azo-bridges (CNNC).

TPAPA/Ag(111)	ΔE_{rel}[eV]	z_{AgN}[Å]	ω[deg]
all-*trans*	0.00	3.25	178
all-*cis*(a)	2.64	2.43	38
all-*cis*(b)	2.58	3.13	11
all-*cis*(c)	2.58	3.49	-13

molecules adsorbed on Ag(111) [143]. The outer phenyl rings are adsorbed lying flat on the surface, thereby maximizing the van-der-Waals interactions with the substrate. At the same time the inner phenyl rings are tilted due to sterical hindrance imposed by each other and the tripod arrangement around the amine center. This leads to the N–N azo-bridges of the azobenzene subunits being positioned asymetrically at a vertical adsorption height that is significantly higher than in the case of a single azobenzene adsorbed on Ag(111) (3.5 and 3.0 Å for the inner and outer nitrogen atom vs. 2.5 Å for AB/Ag(111) [206]). At this elevated adsorption height, the interaction between the metal and the azo-bridge is reduced, which is reflected in a central dihedral torsion (ω, see also Table A.1) that is almost equal to the value for the gas-phase molecule (180°) as opposed to the significantly bent AB molecule when directly adsorbed on Ag(111) (155°) [206].

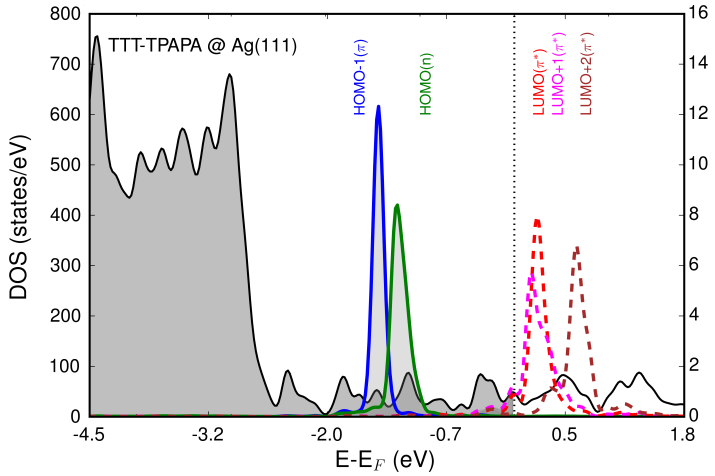

FIGURE A.4: Density-of-States of the Molecular Orbitals of all-*trans*-TPAPA projected from the Density-of-States (MOpDOS) of the combined all-*trans*-TPAPA/Ag(111) surface slab. Shaded areas below the Fermi level correspond to populated states, whereas unshaded areas correspond to unoccupied bands. The frontier molecular orbitals are only minimally broadened due to hybridization with the surface and no significant charge-transfer between substrate and molecule can be observed.

We conclude that the tripod arrangement leads to a geometrical and chemical decoupling of the individual N–N units from the surface.

Figure A.4 shows the corresponding density of states and the molecular orbitals of all-*trans*-TPAPA projected from the MOpDOS [207] of the combined all-*trans*-TPAPA/Ag(111) system. The molecular orbitals are only minimally broadened, suggesting no strong chemical interaction of any molecular subunit with the surface. All unoccupied orbitals are well above the Fermi level, indicating that no significant charge-transfer occurs between substrate and adsorbate. The average energies of HOMO-1, HOMO, LUMO, LUMO+1, and LUMO+2 levels are −1.46, −1.27, 0.17, 0.17, and 0.56 eV with respect to the Fermi level.

An explanation of the experimentally observed tunneling-induced switching could be a conformational *cis-trans* isomerization of the individual azobenzene-legs. To study this process, we investigated a variety of possible structures, where all three azobenzene legs are switched to the *cis* configuration (all-*cis*). Three distinct stable geometries could be identified and are shown in Fig. A.5 with a summary of relevant structural parameters given in Table A.1. The three geometries are between 0.86 and 0.88 eV per switched azobenzene unit less stable than all-*trans*-TPAPA. In comparison, *cis*-azobenzene in gasphase and when adsorbed on Ag(111) is 0.58 eV and 0.77 eV less stable than *trans*-azobenzene [119]. None of the above all-*cis*-TPAPA structures agrees with the experimental findings of (1) dominant STM bias induced changes to the STM topograph close to

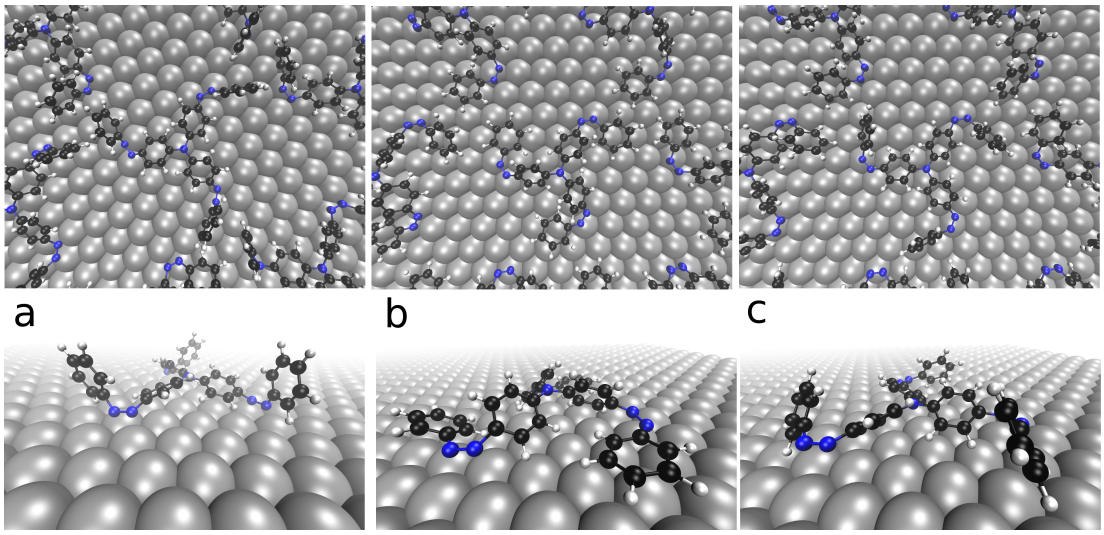

Figure A.5: Three metastable all-*cis*-TPAPA structures adsorbed on Ag(111). (a) Azo-bridge tightly bound to the surface and phenyl rings switched vertically upwards. (b) Phenyl rings flat on the surface, but switched sideways. (c) Both inner and outer phenyl rings tilted with respect to the surface and a thereby overall elevated azo-bridge.

the azo-bridge and almost no changes to the apparent height of outer and inner phenyl ring and (2) no discernible changes to the dI/dV spectrum. In the cases of all-*cis* (a) and (c) the highest protrusion above the surface would be visible far away from the center of the molecule at the position of the outer phenyl ring. Isomerization to all-*cis* (b) and (c) would be accompanied by a significant lateral movement of the STM protrusion associated with the outer phenyl ring, which is also not observed experimentally.

Furthermore, for all three all-*cis* geometries we find significant shifts of the frontier molecular orbitals with respect to all-*trans*-TPAPA (see Table A.2). Notwithstanding the deviations in absolute peak positions between the here calculated ground state Kohn-Sham states and experimentally measured molecular resonances, we find relative peak shifts beyond 0.2 eV in magnitude for HOMO and LUMO states of all-*cis*(a) and (c), which contradicts the minute changes in the dI/dV spectra. These shifts can be understood in terms of the drastic changes in vertical adsorption height and therewith associated change in interaction strength between the molecular resonance and the underlying image charge in the substrate.

Having excluded the possibility of a *trans*-*cis* isomerization, we turn to another potential mechanism of bias-induced molecular switching. Surface adsorption imposes a potential barrier to molecular motion that would otherwise only lead to indistinguishable rotamers in the gas-phase, such as dihedral torsion of the phenyl rings around C–N bonds in AB. For the surface adsorbed all-*trans*-TPAPA

TABLE A.2: Averaged energies of frontier molecular orbitals for different TPAPA isomers adsorbed to a Ag(111) surface. Energies are referenced to the Fermi level.

ϵ-ϵ_F in eV	HOMO-1	HOMO	LUMO	LUMO+1
all-*trans*	-1.46	-1.27	0.17	0.17
all-*cis*(a)	-1.64	-0.92	-0.14	0.22
all-*cis*(b)	-1.43	-1.19	0.11	0.22
all-*cis*(c)	-1.25	-0.87	0.50	0.50

TABLE A.3: Relative energy and vertical adsorption heights for RRR- and RRS-TPAPA. Vertical adsorption heights of azo-nitrogen atoms are shown for each azobenzene group. The first value corresponds to the inner, the second one to the outer nitrogen. In addition, the averaged energies of frontier molecular orbitals is shown for both TPAPA configurations on Ag(111). Energies in eV are referenced to the Fermi level.

all-*trans*-TPAPA	ΔE_{rel}[eV]	$z_{AgN,1}$[Å]	$z_{AgN,2}$[Å]	$z_{AgN,2}$[Å]
RRR	0.00	3.46/3.05	3.46/3.05	3.46/3.05
RRS	-0.03	3.50/3.04	3.66/3.09	2.89/3.09
ϵ-ϵ_F in eV	HOMO-1	HOMO	LUMO	LUMO+1
RRR	-1.46	-1.27	0.17	0.17
RRS	-1.49	-1.32	0.12	0.13

species, the inner phenyl rings can be tilted with the elevated side to the left or to the right of the AB molecular axis. This gives rise to two different types of islands observed in the STM, islands where the inner rings are either oriented clockwise or counterclockwise. In addition, for each of these chiral species, the outer phenyl ring can be either situated to the left (S) or to the right (R) of the plane defined by the molecular axis and the surface normal, giving rise to two distinguishable enantiomers (compare Fig. A.3 and see also Fig. A.6). Up to now we have only considered structures where the outer phenyl rings are all in R position (RRR-all-*trans*-TPAPA). In the following we omit the prefix 'all-*trans*' and only refer to TPAPA. Figure A.6 shows RRR-TPAPA and RRS-TPAPA.

The geometrical and electronic changes of molecular isomerization between R and S configurations of the AB units are in accordance with experimental observations. In the case of the S configuration of the outer phenyl group with respect to the clockwise-rotated inner phenyl rings, the nitrogen atom bound to the inner phenyl ring ('inner nitrogen atom') is adsorbed at about 0.6 Å reduced

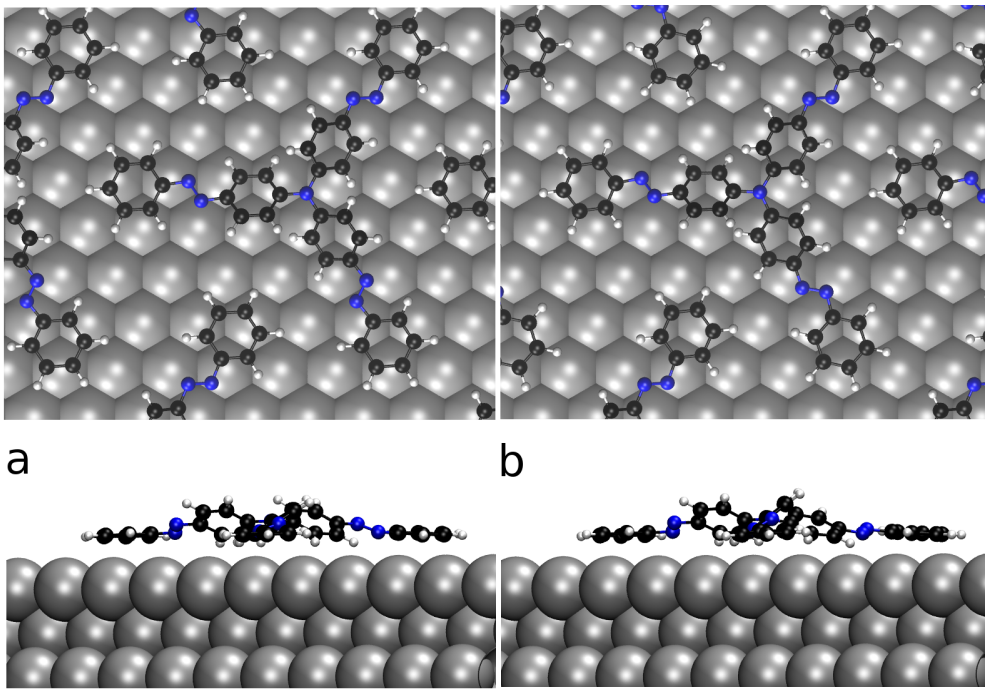

Figure A.6: All-*trans*-TPAPA adsorbed on Ag(111) surface in two chiral configurations viewed orthogonal to (top) and along the surface (bottom). In the left configuration (RRR, a), all outer phenyl rings lie to the right of the azo-bridge of the corresponding AB unit. In the right configuration (RRS, b), the bottom right phenyl group is switched to the left of the azo bridge. As a result, the corresponding azo-nitrogens are adsorbed at a different height from the surface.

vertical height when compared to the R configuration. At the same time the vertical adsorption height of the outer nitrogen atom of the azo bridge lies almost at the same height (cf. Table A.3). This highly localized geometrical change will result in a strongly reduced apparent height around the azo-bridge that will appear as a depression in STM topographs. At the same time the molecular resonances of the RRS configuraton as shown in Table A.3 are almost unchanged when compared to the RRR configuration. While the S state is slightly favored the difference in stability of 0.03 eV between both states is negligible considering the accuracy of the underlying density functional approximation. Furthermore the energies of the states with respect to the Fermi level are almost unchanged by an R/S isomerization, which is in accordance with measured dI/dV curves.

These two stable structures can be transformed into each other by two different pathways. One is a pedalling motion of the azo-bridge, where the nitrogen atoms twist around each other and the outer phenyl ring is dragged laterally across the surface. We have calculated a minimum energy path for this motion using the NEB method (see Fig. A.7). The two Nitrogen atoms twist around each other during this transformation. The corresponding barrier is 0.47 eV. The second

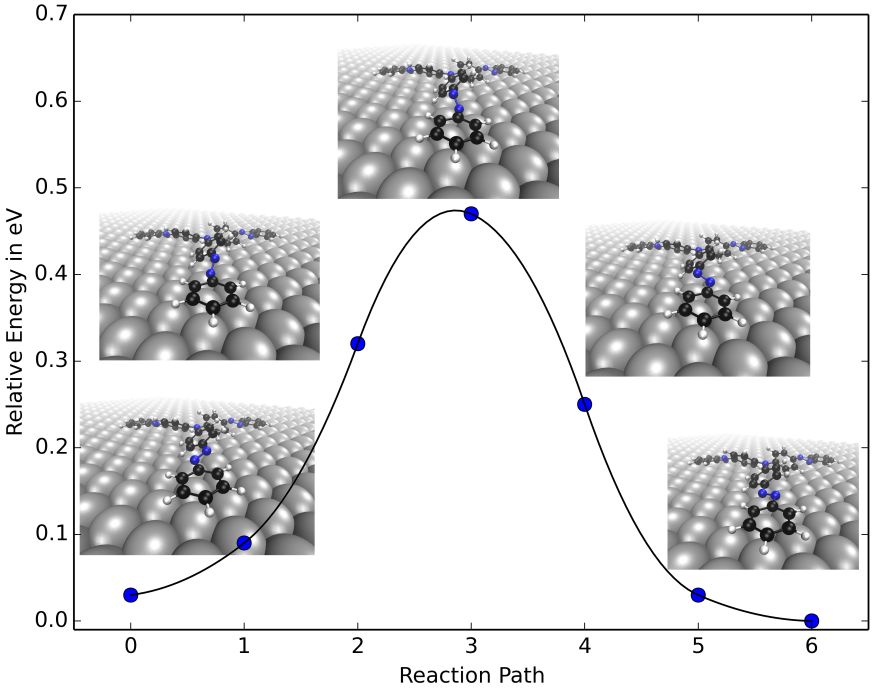

FIGURE A.7: Minimum energy path between RRR-TPAPA (left) and RRS-TPAPA (right) calculated with the NEB method. Shown as insets are intermediate structures along the path.

possible reaction involves an out-of-plane rotation of the outer phenyl ring. We expect this process to involve a higher barrier due to the additional penalty of lifting the phenyl ring from the surface and loosing the dispersion interactions between them. This is supported by a single energy evaluation for a distorted structure in which the outer phenyl ring is twisted 90° with respect to the surface. The corresponding structure is 0.8 eV less stable than RRS-TPAPA.

We conclude that the experimentally observed unswitched groundstate structure corresponds to an SSS-TPAPA molecule, where the outer phenyl rings are rotated counterclockwise from the inner phenyl rings. The S configuration corresponds to the outer phenyl rings being on the opposite side of the AB plane formed by the molecular axis and the surface normal than the upwards-tilted side of the inner phenyl ring. In contrast, in the R configuration, both lie at the same side of the azo-bridge, resulting in an increased height of the azo-bridge. The STM-induced switching of this SSS state leads to a sequential pedalling rotation of the azo-bridge and configurational isomerization to SSR, SRR, and finally RRR states. The switching is accompanied by geometrical changes that increase the apparent height around the azo-bridge including a minor lateral shift of the outer phenyl ring.

A.2 Adatom Coadsorption with Three-Dimensional Cyclophanes on Ag(111)

A.2.1 Density Functional Theory Calculations

Ab initio calculations have been performed in the framework of density functional theory as implemented in the VASP code [170]. Wave functions have been expanded using a plane wave basis set with an energy cutoff of 400 eV. We have used the projector augmented wave method [208] to treat the core electrons and the PBE form of the generalized gradient approximation for the exchange and correlation functional [140]. Van der Waals interactions have been treated using the method by Tkachenko and Scheffler [171]. The experimental supercell is $6 \times 2\sqrt{3}R30°$. We use this cell of 24 atoms per layer to for a periodic system using 5 atomic layers in the perpendicular direction. The k-point sampling is $1 \times 3 \times 1$ for initial adsorption geometries and Tersoff-Hamann images [62, 172]. The two topmost layers and the supported atoms and molecules to relax until forces were smaller than 0.02 eV/Å.

Molecular Overlayer

The molecule is composed of two aromatic platforms, one being a stilbene and the other the NTCDI molecules. The two platforms are bound covalently at their edges via 3-membered aliphatic chains including one S atom (see figure of the 3D molecule). The two S atoms can adopt *cis* or *trans* configuration with respect to the platforms and we found the cis conformer to be 0.2 eV more stable. The distance between the parallel platforms is of the order of 3.6 Å. Upon adsorption we have compared two opposite orientations: the first one with NTCDI being the lower platform and the second with stilbene being the lower platform. By comparing their calculated STM contrast with the experimental image at low bias we determine that NTCDI is linked to the surface. The molecule (the NTCDI platform) binds via the pi-stacking of the aromatic perylene and mesomeric forms of NTCDI hint at two radical oxygens interacting with the closest Ag atom. ($d_{O-Ag} = 2.8$ Å and $d_{O-Ag} = 3.0$ Å). We define the adsorption energy as follows:

$$\epsilon = (E_{ads} - E_{gas} - E_{Ag111}) \tag{A.1}$$

with E_{ads}, E_{gas} and E_{Ag111}, being the energy of the full adsorbed system, of the molecule in gas phase and of the bare surface respectively. The computed adsorption energy per molecule ϵ is -2.56 eV.

Energies of Adatoms in the Molecular Layer

We have studied several structures that could give rise to adatoms within the molecular layer. We find that adatoms adsorbed at the FCC hollow site reduce the system's energy if they are placed between two S atoms of adjacent molecules. Other configurations such as an atom on the next HCP hollow site, or bridge and top sites are systematically of higher energy. Among them, the next lowest one is the HCP hollow site but it is still 450 meV higher than the FCC hollow site between S atoms.

Once an atom is stable on the FCC hollow site between S atoms, a second adatom can be added in the empty space between 4 molecules. Occupying the other FCC hollow site is energetically favorable, but the minimum of energy is found for the next HCP hollow site, in such a way that a substrate atom lies in between the two adatoms. This configuration is 120 meV more stable than the one with two FCC hollow sites. The adsorption energy for the second atom, taking the energy reference as the energy of the system with a FCC-hollow adatom between two S atoms is -2.71 eV. The addition of a third adatom in the metallic area among molecules is hindered by steric forces and is not energetically stable.

A.2.2 Phases with Adatoms in the Molecular Layer

To estimate the number of adatoms that are thermodynamically stable within the molecular layer, we compute the change in Gibbs free energy per unit area [209], $\Delta G(\Delta\mu(T,P))$ for one and two Ag adatoms, as a function of the Ag gas chemical potential (Fig. 4.4 in Chapter 4). The physical picture is that there are four regions of the crystal; (*i*) one with only adatoms, (*ii*) the molecular layer without adatoms (*zero adatoms* in Fig. 4.4), (*iii*) the molecular layer with one adatom (*one* in Fig. 4.4), and (*iv*) the molecular layer with two adatoms (*two adatoms* in Fig. 4.4). These two regions are in equilibrium with a gas reservoir of Ag atoms at a temperature T and pressure P. Then the chemical potential $\mu(T,P)$ of this gas is going to determine which phase is favorable.

To simplify, let us assume that in ultra-high vacuum the changes in chemical potential $\Delta\mu(T,P)$ are due to the adsorption or desorption of Ag adatoms into a very dilute gas, and we disregard zero-point motion and vibrational contributions to the free energy. Hence:

$$\Delta\mu(T,P) \approx E(Ag/Ag(111)) - E_{Ag} - E(Ag(111)). \tag{A.2}$$

In the approximation, the change of chemical potential is the adsorption energy of Ag adatoms on the clean Ag (111) surface [210], given by the difference between the energy of the system with adsorbed atoms ($E(Ag/Ag(111))$) and the sum of the energies of gas atoms (E_{Ag}) and clean surface ($E(Ag(111))$. Using the above

DFT calculations, we obtain that the adsorption energy is $-2.52\,\text{eV}$ per adatom in the unit cell of the calculation. With the above approximations, we obtain:

$$\Delta G(\Delta\mu) \approx \frac{m}{A}(\epsilon - \Delta\mu(T,P)). \tag{A.3}$$

$\Delta G(\Delta\mu(T,P))$ is evaluated as a function of the number of adatoms, m, per unit-cell area, A. Besides the change in chemical potential, the change in free energy depends on the energy gained during the adsorption process per adatom, ϵ. This energy is defined as:

$$\epsilon = (E_{adatoms} - E_{mol} - m \times E_{Ag})/m. \tag{A.4}$$

This equation can be rewritten to express it in the energies of each of the sequential adsorption steps. Let us call E_2 the energy of the full system with two adatoms, and E_1 the energy of the full system with one adatom. We also have E_{mol} which is the energy of the adsorbed overlayer without adatoms and E_{Ag} that is the energy of one Ag atom in the gas phase. Then Eq. (A.4) can be rewritten as:

$$\epsilon = \frac{1}{2}((E_2 - E_1 - E_{Ag}) + (E_1 - E_{mol} - E_{Ag})) \tag{A.5}$$

which is the average of the adsorption energy per adatom, namely the sum of the adsorption energies of the first adatom and of the second one divided by two. Table A.4 displays the computed values of each quantity.

Quantity	Energy (eV)
E_{Ag}	-0.04
$E(Ag(111))$	-348.449
$E(Ag/Ag(111))$ (FCC)	-351.009
$E(Ag/Ag(111))$ (HCP)	-351.004
E_{gas}	-456.14
E_{mol}	-807.1515
E_1	-810.294
E_2	-813.04

Table A.4: Energies of the different substrate, molecule and adatom configurations needed to evaluate the adsorption energies and the phase diagram, Fig. 4.4 in Chapter 4.

A.2.3 Upside-Down Model Compared to Symmetric NDI-Cyclophane

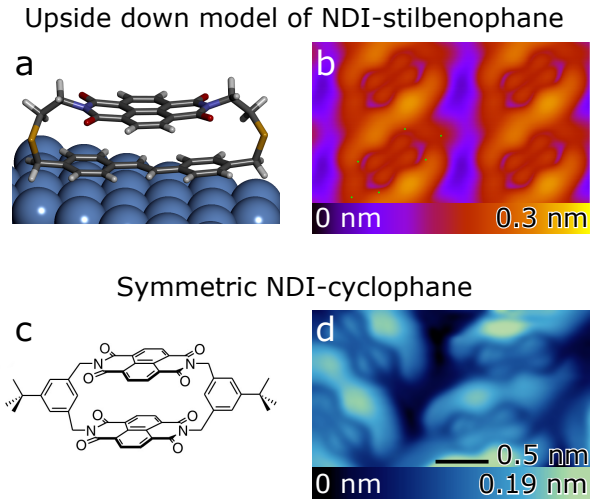

FIGURE A.8: (a) Optimized structure of upside down NDI-stilbenophane with the stilben moiety towards the surface. (b) Simulated constant current topograph of the upside down NDI-stilbenophane model at 1.5 V. (c) Lewis structure of symmetric NDI-cyclophane which comprise two identical NDI subunits. (d) Constant current topograph of symmetric NDI-cyclophane molecules acquired at 3 V.

A.2.4 AFM Frequency Shift of an NDI-Azobenzenophane Island.

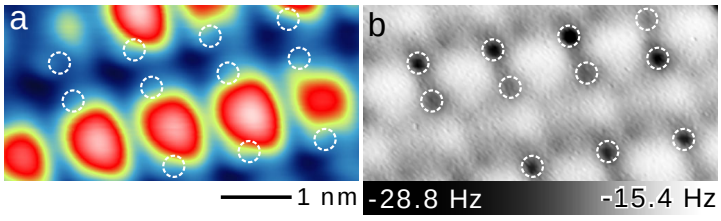

FIGURE A.9: (a) Constant current topograph (550 mV, 16 pA) of an NDI-azobenzenophane island. The dashed circles mark the positions of highest frequency shift extracted from (b). (b) AFM frequency shift data of the same area measured at constant height with an amplitude of $A = 0.8$ Å. The The feedback loop was disabled at $V = 550$ mV and $I = 16$ pA. From the corresponding tip–sample distance the tip was brought closer to the sample by 220 pm.

A.2.5 Orbitals of Gas-Phase NDI-Cyclophane Molecules

Calculations of the gas-phase NDI-cyclophane molecules were performed with Gaussian [211]. The hybrid functional B3LYP and basis sets 6-31+G and 6-311+G were used due to the good performance for organic molecules [212]. Van der Waals interaction was accounted for with D3 dispersion correction by Grimme [213]. The energies obtained with both basis sets differ less then 50 meV. Three energy minima with different positions of the sulfur atoms were found for both molecules. The energy differences between these geometries are within the uncertainty range of the used method and the corresponding orbitals are nearly identical. Figures A.10 (a–d) show the resulting LUMO and LUMO+1.

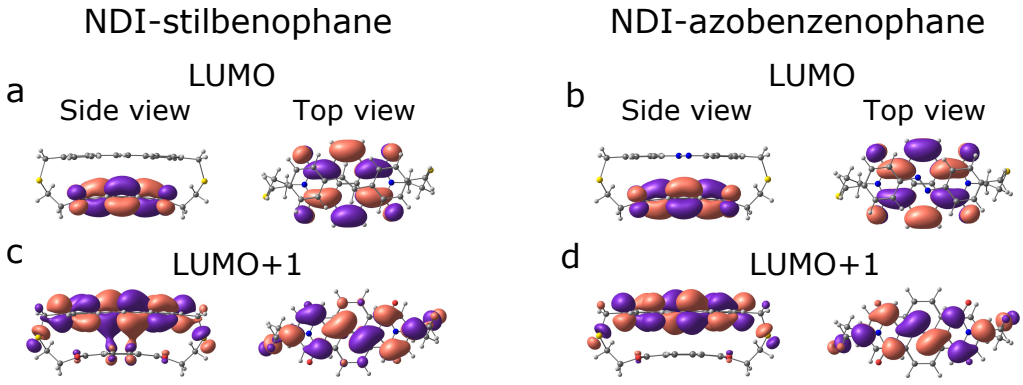

Figure A.10: Molecular orbitals of isolated NDI-stilbenophane and NDI-azobenzenophane. (a, b) The LUMO is localized to the NDI platform. (c, d) The LUMO+1 extends over the functional moiety. Gas-phase calculations were performed with Gaussian 09 [211] using the B3LYP functional with a 6-311+g basis set.

A.2.6 Charging of NDI-Cyclophane Molecules

Besides the spectral features of NDI-cyclophane molecules (Fig. 4.5 (a) and (b) in Chapter 4) some molecules exhibit additional sharp peaks in dI/dV spectra either at positive or negative sample voltage. Such peaks are assigned to charging processes [214–217]. Figure A.11 (a) shows a sharp peak at a sample voltage of $V = 810\,\mathrm{mV}$. A constant height dI/dV map at the corresponding voltage of the area around the molecule is shown in Fig. 4.5 (b). A scaled model indicates the molecule's position. Around the molecule a ring structure is observed. Similar ring structures are reported for impurities in semiconductors [218–221], single atoms in molecular monolayers [214, 222], molecules on insulating layers [223] as well as bulky molecules on metal surfaces [224].

Figure 4.5 (c) shows dI/dV spectra acquired at another molecule. Depending on the position at the molecule a sharp peak (red curve) or a dip (black curve) occurs. Figure 4.5 (d) shows a constant height dI/dV map of the corresponding molecule at the voltage of the dip in Fig. 4.5 (c). A model of the stilbene moiety is overlaid. The map reveals areas of high differential conductance close to the phenyl rings and decreased and slightly negative differential conductance at the center of the stilbene moiety.

A peak in the dI/dV spectra is caused by a stepped increase of the tunneling current. The present case might be explained with a double-barrier tunneling junction model [214–216, 224]. One barrier is provided by the vacuum between tip and molecule, another by the molecule. Molecular levels can be shifted with respect to the Fermi levels of the tip and substrate by changing the voltage applied to the junction. If a molecular level is aligned with either the Fermi energy of tip or sample, tunneling from one electrode through the molecular level to the other electrode becomes feasible and the conductance through the junction increases.

The dip in the dI/dV spectra implies that the tunneling current is reduced. So far it is not clear what causes the reduced conduction. It is likely that due to the bulky three-dimensional double-decker structure of the NDI-cyclophane molecules the charge transport through the molecule might vary depending on the tip position at the molecule. Transport calculations could contribute to understand the effect[1].

It has to be noted that only some molecules (not more than $\approx 10\,\%$) showed additional peaks and ring structures and no straightforward connection between the molecule's appearance or position in the island and the occurrence of additional peaks were found.

[1] private correspondence with Nicolás Lorente

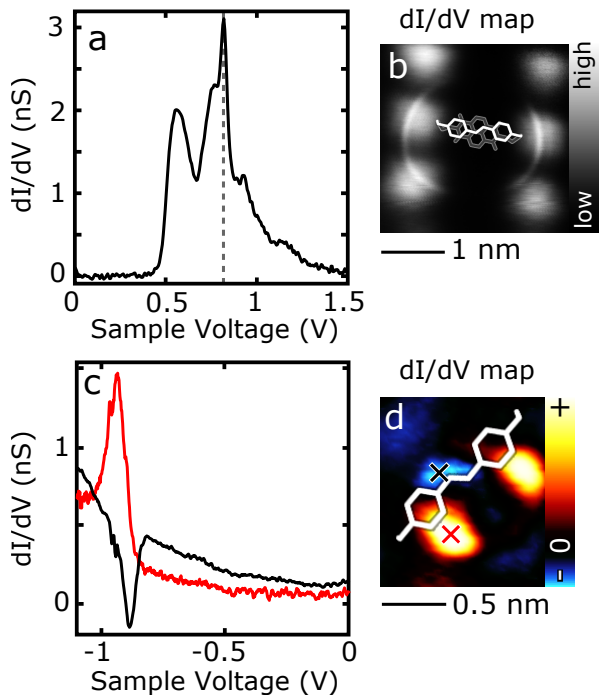

Figure A.11: (a) dI/dV spectra of a NDI-stilbenophane molecule with a sharp peak at $V = 810\,\mathrm{mV}$ (dashed line) in addition to the typical sequence of equidistant peaks. Current feedback loop was opened at $V = 1.6\,\mathrm{V}$ and $I = 1\,\mathrm{nA}$. (b) dI/dV signal acquired at constant height with a sample voltage of $V = 810\,\mathrm{mV}$ over the molecule which features the sharp peak in (a). A model of the calculated molecular structure is overlaid. Segments of a circle are visible around the molecule. (c) dI/dV spectra of a NDI-stilbenophane molecule with the feedback opened at $V = -1.1\,\mathrm{V}$ and $I = 300\,\mathrm{pA}$. Colored crosses in (d) indicate the positions of measurement. Spectra acquired close to the phenyl rings (red) exhibit a peak ($V = -930\,\mathrm{mV}$) whereas spectra measured at the center (black) show a dip ($V = -890\,\mathrm{mV}$). (d) Constant height dI/dV signal recorded at $V = -900\,\mathrm{mV}$. A scaled model of the stilbene subunit is overlaid.

A.3 Force Spectroscopy on Iron Tetraphenylporphyrin Molecules and Transfer of Cl Ligands

A.3.1 Computational Details

Density-functional-theory (DFT) calculations shown in Chapter 5 were performed by Dr. Martin Ondráček using the DFT method as implemented in the Vienna Ab-initio Simulation Package (VASP) [225]. There was an on-site Coulombic term (U) introduced on the Fe atom. A simplified version of LDA+U by Dudarev et al. [226] was used, in which only the difference $U - J$ is significant, rather than the individual parameters U and J. They were set to $U = 4\,\mathrm{eV}$ and $J = 1\,\mathrm{eV}$, as recommended in Ref. [227], so $U - J = 3\,\mathrm{eV}$. The exchange-correlation functional was the generalized gradient approximation (GGA) in the Perdew-Burke-Ernzerhof (PBE) variant [140]. A projector-augmented wave (PAW) method [228] with a plane-wave basis was used. The number of basis functions was specified by a kinetic-energy cutoff of 400 eV. The calculation was spin polarized. The initial magnetic moment was set to 2.0 or 2.5 μ_B (Bohr magneton) on the Fe atom and zero elsewhere. In most cases, the initial value 2.0 μ_B was tried first and if it had converged to a non-magnetic state, 2.5 μ_B was used to obtain the magnetic state (the total energy of which was always found to be below that of the non-magnetic state). The cycle for electronic self-consistency was considered converged when the total energy changed by less than 1 μeV between iterations. The geometric structure was considered converged when forces on any free atom were below $0.01\,\mathrm{eV/Å}$. The method of density-of-states integration (used to determine the Fermi level) was to apply a Gaussian smearing of the discrete energy levels with $\sigma = 0.1\,\mathrm{eV}$. The Brillouin zone was sampled by a mesh of $3 \times 3 \times 1$ k-points. Van der Waals (London dispersion) forces were included using a correction by Tkatchenko and Scheffler [171]. To reduce computational cost, the geometries of FeTPP or FeTPPCl were first optimized on the Au(111) surface in the absence of a tip. The Au slab representing the surface consisted of 4 atomic layers. Only the bottom atomic layer of gold was kept immobile during the search for optimal geometry. The optimized geometries were then fixed and only Fe in the case of FeTPP and the Cl atom in the case of FeTPPCl could relax during the approach of the tip. From the pyramidal tip (20 atoms), only the outermost gold atom at the apex was allowed to move, unless the tip was terminated with Cl, in which case both the Au and the Cl atom were allowed to relax. Bader analysis has been done for the optimized geometry of FeTPP or FeTPPCl at the atop site on the Au(111) surface (i.e. Fe atom of the molecule positioned directly above a Au atom), without the tip.

Bibliography

[1] I. L. Markov. *Limits on fundamental limits to computation.* Nature **512**, 147 (2014).

[2] D. Xiang, X. Wang, C. Jia, T. Lee, and X. Guo. *Molecular-scale electronics: From concept to function.* Chem. Rev. **116**, 4318 (2016).

[3] C. Wang, A. S. Batsanov, M. R. Bryce, S. Martín, R. J. Nichols, S. J. Higgins, V. M. García-Suárez, and C. J. Lambert. *Oligoyne single molecule wires.* J. Am. Chem. Soc. **131**, 15647 (2009).

[4] P. Moreno-García, M. Gulcur, D. Z. Manrique, T. Pope, W. Hong, V. Kaliginedi, C. Huang, A. S. Batsanov, M. R. Bryce, C. Lambert, and T. Wandlowski. *Single-molecule conductance of functionalized oligoynes: Length dependence and junction evolution.* J. Am. Chem. Soc. **135**, 12228 (2013).

[5] A. Aviram and M. A. Ratner. *Molecular rectifiers.* Chem. Phys. Lett. **29**, 277 (1974).

[6] G. J. Ashwell, J. Ewington, and K. Moczko. *Orientation-induced molecular rectification and nonlinear optical properties of a squaraine derivative.* J. Mater. Chem. **15**, 1154 (2005).

[7] G. Ho, J. R. Heath, M. Kondratenko, D. F. Perepichka, K. Arseneault, M. Pézolet, and M. R. Bryce. *The first studies of a tetrathiafulvalene-σ-acceptor molecular rectifier.* Chem. Eur. J. **11**, 2914 (2005).

[8] H. Park, J. Park, A. K. L. Lim, E. H. Anderson, A. P. Alivisatos, and P. L. McEuen. *Nanomechanical oscillations in a single-C_{60} transistor.* Nature **407**, 57 (2000).

[9] H. Song, Y. Kim, Y. H. Jang, H. Jeong, M. A. Reed, and T. Lee. *Observation of molecular orbital gating.* Nature **462**, 1039 (2009).

[10] J. Henzl, M. Mehlhorn, H. Gawronski, K.-H. Rieder, and K. Morgenstern. *Reversible cis-trans isomerization of a single azobenzene molecule.* Angew. Chem. Int. Edit. **45**, 603 (2006).

[11] M. Alemani, M. V. Peters, S. Hecht, K.-H. Rieder, F. Moresco, and L. Grill. *Electric field-induced isomerization of azobenzene by STM.* J. Am. Chem. Soc. **128**, 14446 (2006).

[12] B.-Y. Choi, S.-J. Kahng, S. Kim, H. Kim, H. W. Kim, Y. J. Song, J. Ihm, and Y. Kuk. *Conformational molecular switch of the azobenzene molecule: A scanning tunneling microscopy study.* Phys. Rev. Lett. **96**, 156106 (2006).

[13] G. Pace, V. Ferri, C. Grave, M. Elbing, C. von Hanisch, M. Zharnikov, M. Mayor, M. A. Rampi, and P. Samori. *Cooperative light-induced molecular movements of highly ordered azobenzene self-assembled monolayers.* P. Natl. Acad. Sci. USA **104**, 9937 (2007).

[14] M. J. Comstock, N. Levy, A. Kirakosian, J. Cho, F. Lauterwasser, J. H. Harvey, D. A. Strubbe, J. M. J. Fréchet, D. Trauner, S. G. Louie, and M. F. Crommie. *Reversible photomechanical switching of individual engineered molecules at a metallic surface.* Phys. Rev. Lett. **99**, 038301 (2007).

[15] Y. L. Huang, Y. Lu, T. C. Niu, H. Huang, S. Kera, N. Ueno, A. T. S. Wee, and W. Chen. *Reversible single-molecule switching in an ordered monolayer molecular dipole array.* Small **8**, 1423 (2012).

[16] J. L. Zhang, J. L. Xu, T. C. Niu, Y. H. Lu, L. Liu, and W. Chen. *Reversible switching of a single-dipole molecule imbedded in two-dimensional hydrogen-bonded binary molecular networks.* J. Phys. Chem. C **118**, 1712 (2014).

[17] T. Miyamachi, M. Gruber, V. Davesne, M. Bowen, S. Boukari, L. Joly, F. Scheurer, G. Rogez, T. K. Yamada, P. Ohresser, E. Beaurepaire, and W. Wulfhekel. *Robust spin crossover and memristance across a single molecule.* Nature Commun. **3**, 938 (2012).

[18] T. G. Gopakumar, F. Matino, H. Naggert, A. Bannwarth, F. Tuczek, and R. Berndt. *Electron-induced spin crossover of single molecules in a bilayer on gold.* Angew. Chem. Int. Edit. **51**, 6262 (2012).

[19] S. W. Wu, N. Ogawa, and W. Ho. *Atomic-scale coupling of photons to single-molecule junctions.* Science **312**, 1362 (2006).

[20] Y.-S. Fu, T. Zhang, S.-H. Ji, X. Chen, X.-C. Ma, J.-F. Jia, and Q.-K. Xue. *Identifying charge states of molecules with spin-flip spectroscopy.* Phys. Rev. Lett. **103**, 257202 (2009).

[21] T. Leoni, O. Guillermet, H. Walch, V. Langlais, A. Scheuermann, J. Bonvoisin, and S. Gauthier. *Controlling the charge state of a single redox molecular switch.* Phys. Rev. Lett. **106**, 216103 (2011).

[22] F. Mohn, J. Repp, L. Gross, G. Meyer, M. S. Dyer, and M. Persson. *Reversible bond formation in a gold-atom–organic-molecule complex as a molecular switch.* Phys. Rev. Lett. **105**, 266102 (2010).

[23] J. E. Green, J. W. Choi, A. Boukai, Y. Bunimovich, E. Johnston-Halperin, E. DeIonno, Y. Luo, B. A. Sheriff, K. Xu, Y. S. Shin, H.-R. Tseng, J. F. Stoddart, and J. R. Heath. *A 160-kilobit molecular electronic memory patterned at 1011 bits per square centimetre.* Nature **445**, 414 (2007).

[24] S. Loth, S. Baumann, C. P. Lutz, D. M. Eigler, and A. J. Heinrich. *Bistability in atomic-scale antiferromagnets.* Science **335**, 196 (2012).

[25] J. L. Zhang, J. Q. Zhong, J. D. Lin, W. P. Hu, K. Wu, G. Q. Xu, A. T. S. Wee, and W. Chen. *Towards single molecule switches.* Chem. Soc. Rev. **44**, 2998 (2015).

[26] S. J. van der Molen and P. Liljeroth. *Charge transport through molecular switches.* J. Phys. Condens. Matt. **22**, 133001 (2010).

[27] J. Henzl, T. Bredow, and K. Morgenstern. *Irreversible isomerization of the azobenzene derivate methyl orange on Au(111).* Chem. Phys. Lett. **435**, 278 (2007).

[28] P. Liljeroth, J. Repp, and G. Meyer. *Current-induced hydrogen tautomerization and conductance switching of naphthalocyanine molecules.* Science **317**, 1203 (2007).

[29] E. R. McNellis, G. Mercurio, S. Hagen, F. Leyssner, J. Meyer, S. Soubatch, M. Wolf, K. Reuter, P. Tegeder, and F. S. Tautz. *Bulky spacer groups – a valid strategy to control the coupling of functional molecules to surfaces?* Chem. Phys. Lett. **499**, 247 (2010).

[30] B. Baisch, D. Raffa, U. Jung, O. M. Magnussen, C. Nicolas, J. Lacour, J. Kubitschke, and R. Herges. *Mounting freestanding molecular functions onto surfaces: The platform approach.* J. Am. Chem. Soc. **131**, 442 (2009).

[31] H. Jacob, S. Ulrich, U. Jung, S. Lemke, T. Rusch, C. SchÃ¼tt, F. Petersen, T. Strunskus, O. Magnussen, R. Herges, and F. Tuczek. *Monitoring the reversible photoisomerization of an azobenzene-functionalized molecular triazatriangulene platform on Au(111) by IRRAS.* Phys. Chem. Chem. Phys. **16**, 22643 (2014).

[32] F. Matino, G. Schull, F. Köhler, S. Gabutti, M. Mayor, and R. Berndt. *Electronic decoupling of a cyclophane from a metal surface.* Proc. Natl. Acad. Sci. USA **108**, 961 (2011).

[33] L. Bartels, G. Meyer, and K.-H. Rieder. *Basic steps of lateral manipulation of single atoms and diatomic clusters with a scanning tunneling microscope tip.* Phys. Rev. Lett. **79**, 697 (1997).

[34] D. M. Eigler and E. K. Schweizer. *Positioning single atoms with a scanning tunnelling microscope.* Nature **344**, 524 (1990).

[35] S.-W. Hla, K.-F. Braun, B. Wassermann, and K.-H. Rieder. *Controlled low-temperature molecular manipulation of sexiphenyl molecules on Ag(111) using scanning tunneling microscopy.* Phys. Rev. Lett. **93**, 208302 (2004).

[36] M. Ternes, C. P. Lutz, C. F. Hirjibehedin, F. J. Giessibl, and A. J. Heinrich. *The force needed to move an atom on a surface.* Science **319**, 1066 (2008).

[37] D. M. Eigler, C. P. Lutz, and W. E. Rudge. *An atomic switch realized with the scanning tunnelling microscope.* Nature **352**, 600 (1991).

[38] I.-W. Lyo and P. Avouris. *Field-induced nanometer- to atomic-scale manipulation of silicon surfaces with the STM.* Science **253**, 173 (1991).

[39] L. Bartels, G. Meyer, and K.-H. Rieder. *Controlled vertical manipulation of single CO molecules with the scanning tunneling microscope: A route to chemical contrast.* Appl. Phys. Lett. **71**, 213 (1997).

[40] G. Dujardin, A. Mayne, O. Robert, F. Rose, C. Joachim, and H. Tang. *Vertical manipulation of individual atoms by a direct STM tip-surface contact on Ge(111).* Phys. Rev. Lett. **80**, 3085 (1998).

[41] H. J. Lee. *Single-bond formation and characterization with a scanning tunneling microscope.* Science **286**, 1719 (1999).

[42] S.-W. Hla. *Scanning tunneling microscopy single atom/molecule manipulation and its application to nanoscience and technology.* J. Vac. Sci. Technol. B **23**, 1351 (2005).

[43] J. Repp, G. Meyer, S. M. Stojković, A. Gourdon, and C. Joachim. *Molecules on insulating films: Scanning-tunneling microscopy imaging of individual molecular orbitals.* Phys. Rev. Lett. **94**, 026803 (2005).

[44] K.-F. Braun and S.-W. Hla. *Probing the conformation of physisorbed molecules at the atomic scale using STM manipulation.* Nano Lett **5**, 73 (2005).

[45] G. Schull, T. Frederiksen, M. Brandbyge, and R. Berndt. *Passing current through touching molecules.* Phys. Rev. Lett. **103**, 206803 (2009).

[46] L. Gross, F. Mohn, N. Moll, P. Liljeroth, and G. Meyer. *The chemical structure of a molecule resolved by atomic force microscopy.* Science **325**, 1110 (2009).

[47] T. G. Gopakumar, H. Tang, J. Morillo, and R. Berndt. *Transfer of Cl ligands between adsorbed iron tetraphenylporphyrin molecules.* J. Am. Chem. Soc. **134**, 11844 (2012).

[48] J. Repp. *Imaging bond formation between a gold atom and pentacene on an insulating surface.* Science **312**, 1196 (2006).

[49] P. Liljeroth, I. Swart, S. Paavilainen, J. Repp, and G. Meyer. *Single-molecule synthesis and characterization of metal-ligand complexes by low-temperature STM.* Nano Lett. **10**, 2475 (2010).

[50] W. Auwärter, K. Seufert, F. Bischoff, D. Ecija, S. Vijayaraghavan, S. Joshi, F. Klappenberger, N. Samudrala, and J. V. Barth. *A surface-anchored molecular four-level conductance switch based on single proton transfer.* Nat. Nanotechnol. **7**, 41 (2011).

[51] B. C. Stipe, M. A. Rezaei, and W. Ho. *Coupling of vibrational excitation to the rotational motion of a single adsorbed molecule.* Phys. Rev. Lett. **81**, 1263 (1998).

[52] V. Iancu, A. Deshpande, and S.-W. Hla. *Manipulating kondo temperature via single molecule switching.* Nano Lett. **6**, 820 (2006).

[53] R. Wiesendanger. *Scanning probe microscopy and spectroscopy - Methods and applications* (Cambridge University Press, 1994).

[54] D. A. Bonnell. *Scanning tunneling microscopy and spectroscopy: Theory, techniques, and applications* (VCH, 2001).

[55] S. Morita, F. Giessibl, and R. Wiesendanger. *Noncontact atomic force microscopy*, vol. 2 (Springer, 2002).

[56] F. J. Giessibl. *Advances in atomic force microscopy.* Rev. Mod. Phys. **75**, 949 (2003).

[57] A. Foster and W. Hofer. *Scanning probe microscopy* (Springer-Verlag New York Inc., 2006).

[58] E. Meyer, H. J. Hug, and R. Bennewitz. *Scanning Probe Microscopy: The Lab on a tip* (Springer, 2004).

[59] Y. Seo and W. Jhe. *Atomic force microscopy and spectroscopy.* Rep. Prog. Phys. **71**, 016101 (2007).

[60] C. Chen. *Introduction to scanning tunneling microscopy* (Oxford University Press, New York, 2008), 2 ed.

[61] J. G. Simmons. *Electric tunnel effect between dissimilar electrodes separated by a thin insulating film.* J. Appl. Phys. **34**, 2581 (1963).

[62] J. Tersoff and D. R. Hamann. *Theory and application for the scanning tunneling microscope.* Phys. Rev. Lett. **50**, 1998 (1983).

[63] J. Tersoff and D. R. Hamann. *Theory of the scanning tunneling microscope.* Phys. Rev. B **31**, 805 (1985).

[64] N. D. Lang. *Theory of single-atom imaging in the scanning tunneling microscope.* Phys. Rev. Lett. **56**, 1164 (1986).

[65] N. D. Lang. *Apparent size of an atom in the scanning tunneling microscope as a function of bias.* Phys. Rev. Lett. **58**, 45 (1987).

[66] V. A. Ukraintsev. *Data evaluation technique for electron-tunneling spectroscopy.* Phys. Rev. B **53**, 11176 (1996).

[67] T. R. Albrecht, P. Grütter, D. Horne, and D. Rugar. *Frequency modulation detection using high-Q cantilevers for enhanced force microscope sensitivity.* J. Appl. Phys. **69**, 668 (1991).

[68] F. J. Giessibl. *Forces and frequency shifts in atomic-resolution dynamic-force microscopy.* Phys. Rev. B **56**, 16010 (1997).

[69] *Nano Surf operating instructions easyPLL plus*, 3 ed. (2004).

[70] B. Gotsmann, C. Seidel, B. Anczykowski, and H. Fuchs. *Conservative and dissipative tip-sample interaction forces probed with dynamic AFM.* Phys. Rev. B **60**, 11051 (1999).

[71] U. Dürig. *Extracting interaction forces and complementary observables in dynamic probe microscopy.* Appl. Phys. Lett. **76**, 1203 (2000).

[72] U. Dürig. *Interaction sensing in dynamic force microscopy.* New J. Phys. **2**, 5 (2000).

[73] H. Hölscher, W. Allers, U. D. Schwarz, A. Schwarz, and R. Wiesendanger. *Determination of tip–sample interaction potentials by dynamic force spectroscopy.* Phys. Rev. Lett. **83**, 4780 (1999).

[74] F. J. Giessibl. *A direct method to calculate tip–sample forces from frequency shifts in frequency-modulation atomic force microscopy.* Appl. Phys. Lett. **78**, 123 (2001).

[75] J. E. Sader and S. P. Jarvis. *Accurate formulas for interaction force and energy in frequency modulation force spectroscopy.* Appl. Phys. Lett. **84**, 1801 (2004).

[76] J. Welker, E. Illek, and F. J. Giessibl. *Analysis of force-deconvolution methods in frequency-modulation atomic force microscopy.* Beilstein J. Nanotech. **3**, 238 (2012).

[77] N. Hauptmann. *Force and Conductance in Molecular Junctions.* Ph.D. thesis, CAU Kiel (2013).

[78] H. Hamaker. *The london–van der waals attraction between spherical particles.* Physica **4**, 1058 (1937).

[79] J. N. Israelachvili. *Intermolecular & surface forces* (Academic Press, London, 1992), 2 ed.

[80] S. Sadewasser and T. Glatzel. *Kelvin Probe Force Microscopy, Measuring and Compensating Electrostatic Forces* (Springer, 2012).

[81] W. Demtröder. *Experimentalphysik 2* (Springer, 2004).

[82] W. Melitz, J. Shen, A. C. Kummel, and S. Lee. *Kelvin probe force microscopy and its application.* Surf. Sci. Rep. **66**, 1 (2011).

[83] L. Gross, F. Mohn, P. Liljeroth, J. Repp, F. J. Giessibl, and G. Meyer. *Measuring the charge state of an adatom with noncontact atomic force microscopy.* Science **324**, 1428 (2009).

[84] G. Teobaldi, K. Lämmle, T. Trevethan, M. Watkins, A. Schwarz, R. Wiesendanger, and A. L. Shluger. *Chemical resolution at ionic crystal surfaces using dynamic atomic force microscopy with metallic tips.* Phys. Rev. Lett. **106**, 216102 (2011).

[85] M. Schneiderbauer, M. Emmrich, A. J. Weymouth, and F. J. Giessibl. *CO tip functionalization inverts atomic force microscopy contrast via short-range electrostatic forces.* Phys. Rev. Lett. **112**, 166102 (2014).

[86] L. Gross, B. Schuler, F. Mohn, N. Moll, N. Pavliček, W. Steurer, I. Scivetti, K. Kotsis, M. Persson, and G. Meyer. *Investigating atomic contrast in atomic force microscopy and kelvin probe force microscopy on ionic systems using functionalized tips.* Phys. Rev. B **90**, 155455 (2014).

[87] J. H. Jeans. *The mathematical theory of electricity and magnetism* (Cambridge: Univeristy Press, 1911).

[88] L. Kantorovich, A. Foster, A. Shluger, and A. Stoneham. *Role of image forces in non-contact scanning force microscope images of ionic surfaces.* Surf. Sci. **445**, 283 (2000).

[89] L. N. Kantorovich, A. I. Livshits, and M. Stoneham. *Electrostatic energy calculation for the interpretation of scanning probe microscopy experiments.* J. Phys. Condens. Matter **12**, 795 (2000).

[90] S. Kuhn and P. Rahe. *Discriminating short-range from van der waals forces using total force data in noncontact atomic force microscopy.* Phys. Rev. B **89**, 235417 (2014).

[91] M. A. Lantz, R. Hoffmann, A. S. Foster, A. Baratoff, H. J. Hug, H. R. Hidber, and H.-J. Güntherodt. *Site-specific force-distance characteristics on NaCl(001): Measurements versus atomistic simulations.* Phys. Rev. B **74**, 245426 (2006).

[92] M. Ternes, C. González, C. P. Lutz, P. Hapala, F. J. Giessibl, P. Jelínek, and A. J. Heinrich. *Interplay of conductance, force, and structural change in metallic point contacts.* Phys. Rev. Lett. **106**, 016802 (2011).

[93] A. Sweetman and A. Stannard. *Uncertainties in forces extracted from non-contact atomic force microscopy measurements by fitting of long-range background forces.* Beilstein J. Nanotech. **5**, 386 (2014).

[94] D. Sawada, Y. Sugimoto, K. Morita, M. Abe, and S. Morita. *Simultaneous measurement of force and tunneling current at room temperature.* Appl. Phys. Lett. **94**, 173117 (2009).

[95] J. E. Sader and Y. Sugimoto. *Accurate formula for conversion of tunneling current in dynamic atomic force spectroscopy.* Appl. Phys. Lett. **97**, 043502 (2010).

[96] C. Loppacher, R. Bennewitz, O. Pfeiffer, M. Guggisberg, M. Bammerlin, S. Schär, V. Barwich, A. Baratoff, and E. Meyer. *Experimental aspects of dissipation force microscopy.* Phys. Rev. B **62**, 13674 (2000).

[97] F. J. Giessibl. *High-speed force sensor for force microscopy and profilometry utilizing a quartz tuning fork.* Appl. Phys. Lett. **73**, 3956 (1998).

[98] F. J. Giessibl. *Atomic resolution on Si(111)-(7×7) by noncontact atomic force microscopy with a force sensor based on a quartz tuning fork.* Appl. Phys. Lett. **76**, 1470 (2000).

[99] F. J. Giessibl, S. Hembacher, M. Herz, C. Schiller, and J. Mannhart. *Stability considerations and implementation of cantilevers allowing dynamic force microscopy with optimal resolution: the qPlus sensor.* Nanotechnology **15**, S79 (2004).

[100] J. Berger, M. Švec, M. Müller, M. Ledinský, A. Fejfar, P. Jelínek, and Z. Majzik. *Characterization of the mechanical properties of qPlus sensors.* Beilstein J. Nanotech. **4**, 1 (2013).

[101] S. Gao, Z. Zhang, Y. Wu, and K. Herrmann. *Towards quantitative determination of the spring constant of a scanning force microscope cantilever with a microelectromechanical nano-force actuator.* Meas. Sci. Technol. **21**, 015103 (2009).

[102] J. P. Cleveland, S. Manne, D. Bocek, and P. K. Hansma. *A nondestructive method for determining the spring constant of cantilevers for scanning force microscopy.* Rev. Sci. Instrum. **64**, 403 (1993).

[103] D. G. Cole. *Difficulties in fitting the thermal response of atomic force microscope cantilevers for stiffness calibration.* Meas. Sci. Technol. **19**, 125101 (2008).

[104] J. Lübbe, M. Temmen, P. Rahe, A. Kühnle, and M. Reichling. *Determining cantilever stiffness from thermal noise.* Beilstein J. Nanotech. **4**, 227 (2013).

[105] J. Lübbe, L. Doering, and M. Reichling. *Precise determination of force microscopy cantilever stiffness from dimensions and eigenfrequencies.* Meas. Sci. Technol. **23**, 045401 (2012).

[106] C. Chiutu, A. Stannard, A. M. Sweetman, and P. Moriarty. *Retracted article: Measuring Si-C_{60} chemical forces via single molecule spectroscopy.* Chem. Commun. **47**, 10575 (2011).

[107] A. Sweetman, S. Jarvis, R. Danza, J. Bamidele, S. Gangopadhyay, G. A. Shaw, L. Kantorovich, and P. Moriarty. *Toggling bistable atoms via mechanical switching of bond angle.* Phys. Rev. Lett. **106**, 136101 (2011).

[108] S. Hembacher, F. J. Giessibl, J. Mannhart, and C. F. Quate. *Revealing the hidden atom in graphite by low-temperature atomic force microscopy.* Proc. Nat. Acad. Sci. U.S.A. **100**, 12539 (2003).

[109] M. Tooley. *Electronic Circuits: Fundamentals and Applications* (Elsevier, 2006).

[110] K. Scheil. *Kombinierte Rasterkraft- und Rastertunnelmikroskopie an organischen Molekülen.* Master's thesis, Christian-Albrechts-Universität zu Kiel (2011).

[111] G. H. Simon, M. Heyde, and H.-P. Rust. *Recipes for cantilever parameter determination in dynamic force spectroscopy: spring constant and amplitude.* Nanotechnology **18**, 255503 (2007).

[112] C. Kittel. *Einführung in die Festkörper Physik*, vol. 10 (Oldenbourg Verlag, 1993).

[113] H. Rau. *Photoisomerization of azobenzenes.* In *Photochemistry and Photophysics*, vol. 2, pp. 119–121 (CRC Press, 1989).

[114] T. Schultz, J. Quenneville, B. Levine, A. Toniolo, T. J. Martínez, S. Lochbrunner, M. Schmitt, J. P. Shaffer, M. Z. Zgierski, and A. Stolow. *Mechanism and dynamics of azobenzene photoisomerization.* J. Am. Chem. Soc. **125**, 8098 (2003).

[115] S. Hagen, F. Leyssner, D. Nandi, M. Wolf, and P. Tegeder. *Reversible switching of tetra-tert-butyl-azobenzene on a Au(111) surface induced by light and thermal activation.* Chem. Phys. Lett. **444**, 85 (2007).

[116] E. R. McNellis, J. Meyer, and K. Reuter. *Azobenzene at coinage metal surfaces: Role of dispersive van der waals interactions.* Phys. Rev. B **80**, 205414 (2009).

[117] J. Cho, L. Berbil-Bautista, N. Levy, D. Poulsen, J. M. J. Fréchet, and M. F. Crommie. *Functionalization, self-assembly, and photoswitching quenching for azobenzene derivatives adsorbed on Au(111).* J. Chem. Phys. **133**, 234707 (2010).

[118] J. Henzl, P. Puschnig, C. Ambrosch-Draxl, A. Schaate, B. Ufer, P. Behrens, and K. Morgenstern. *Photoisomerization for a molecular switch in contact with a surface.* Phys. Rev. B **85**, 035410 (2012).

[119] R. J. Maurer and K. Reuter. *Bistability loss as a key feature in azobenzene (non-)switching on metal surfaces.* Angew. Chem. Int. Edit. **51**, 12009 (2012).

[120] G. L. Hallett-Tapley, C. D'Alfonso, N. L. Pacioni, C. D. McTiernan, M. González-Béjar, O. Lanzalunga, E. I. Alarcon, and J. C. Scaiano. *Gold nanoparticle catalysis of the cis–trans isomerization of azobenzene.* Chem. Commun. **49**, 10073 (2013).

[121] E. Titov, L. Lysyakova, N. Lomadze, A. V. Kabashin, P. Saalfrank, and S. Santer. *Thermal cis-to-trans isomerization of azobenzene-containing molecules enhanced by gold nanoparticles: An experimental and theoretical study.* J. Phys. Chem. C **119**, 17369 (2015).

[122] N. Néel, J. Kröger, L. Limot, T. Frederiksen, M. Brandbyge, and R. Berndt. *Controlled contact to a C_{60} molecule.* Phys. Rev. Lett. **98**, 065502 (2007).

[123] H. Vazquez, R. Skouta, S. Schneebeli, M. Kamenetska, R. Breslow, L. Venkataraman, and M. Hybertsen. *Probing the conductance superposition law in single-molecule circuits with parallel paths.* Nat. Nanotechnol. **7**, 663 (2012).

[124] A detailed comparison of data from different derivatives is difficult because varying bias voltages and currents have been used. For instance, for AB on Au(111) a switching yield per electron $Y \sim 10^{-18}$ at -1.5 V and 0.5 nA was reported [12], for anilino-nitro AB on Au(111) $Y \sim 10^{-9}$ at 2.5 V and 0.5 nA [126], for 4-(4-Nitrophenylazo)aniline on Au(111) $Y \sim 10^{-8}$ at 0.7 V [10], for *trans–cis* isomerisation of di-hydroxy-AB adsorbed on NaCl the yield is $Y \sim 10^{-8}$ at 0.7 V [127] and for tetra-tert-butyl AB on Au(111) $Y \sim 10^{-8}$ at 1.6 V, 0.5 nA, increasing to $Y \sim 10^{-7}$ at 1.6 V, 2 nA.[125].

[125] M. Alemani, S. Selvanathan, F. Ample, M. V. Peters, K.-H. Rieder, F. Moresco, C. Joachim, S. Hecht, and L. Grill. *Adsorption and switching properties of azobenzene derivatives on different noble metal surfaces: Au(111), Cu(111), and Au(100).* J. Phys. Chem. C **112**, 10509 (2008).

[126] J. Henzl and K. Morgenstern. *An electron induced two-dimensional switch made of azobenzene derivatives anchored in supramolecular assemblies.* Phys. Chem. Chem. Phys. **12**, 6035 (2010).

[127] A. Safiei, J. Henzl, and K. Morgenstern. *Isomerization of an azobenzene derivative on a thin insulating layer by inelastically tunneling electrons.* Phys. Rev. Lett. **104**, 216102 (2010).

[128] T. Takahashi, T. Tanino, H. Ando, H. Nakano, and Y. Shirota. *Surface relief grating formation using a novel azobenzene-based photochromic amorphous molecular material, tris[4-(phenylazo)phenyl]amine.* Mol. Cryst. Liq. Cryst. **430**, 9 (2005).

[129] J. Bahrenburg, C. M. Sievers, J. B. Schönborn, B. Hartke, F. Renth, F. Temps, C. Näther, and F. D. Sönnichsen. *Photochemical properties of multi-azobenzene compounds.* Photochem. Photobiol. Sci. **12**, 511 (2013).

[130] T. G. Gopakumar, T. Davran-Candan, J. Bahrenburg, R. J. Maurer, F. Temps, K. Reuter, and R. Berndt. *Broken symmetry of an adsorbed molecular switch determined by scanning tunneling spectroscopy.* Angew. Chem. Int. Edit. **52**, 11007 (2013).

[131] C. Bronner, G. Schulze, K. J. Franke, J. I. Pascual, and P. Tegeder. *Switching ability of nitro-spiropyran on Au(111): electronic structure changes as a sensitive probe during a ring-opening reaction.* J. Phys. Condens. Matter **23**, 484005 (2011).

[132] F. Jäckel, U. G. E. Perera, V. Iancu, K.-F. Braun, N. Koch, J. P. Rabe, and S.-W. Hla. *Investigating molecular charge transfer complexes with a low temperature scanning tunneling microscope.* Phys. Rev. Lett. **100**, 126102 (2008).

[133] S. Karan, N. Li, Y. Zhang, Y. He, I.-P. Hong, H. Song, J.-T. Lü, Y. Wang, L. Peng, K. Wu, G. S. Michelitsch, R. J. Maurer, K. Diller, K. Reuter, A. Weismann, and R. Berndt. *Spin manipulation by creation of single-molecule radical cations.* Phys. Rev. Lett. **116**, 027201 (2016).

[134] N. Henningsen, R. Rurali, K. J. Franke, I. Fernández-Torrente, and J. I. Pascual. *Trans to cis isomerization of an azobenzene derivative on a Cu(100) surface.* Appl. Phys. A **93**, 241 (2008).

[135] Y. Wang, J. Kröger, R. Berndt, and W. A. Hofer. *Pushing and pulling a sn ion through an adsorbed phthalocyanine molecule.* J. Am. Chem. Soc. **131**, 3639 (2009).

[136] Y. Wang, X. Ge, G. Schull, R. Berndt, H. Tang, C. Bornholdt, F. Koehler, and R. Herges. *Switching single azopyridine supramolecules in ordered arrays on Au(111).* J. Am. Chem. Soc. **132**, 1196 (2010).

[137] U. G. E. Perera, F. Ample, H. Kersell, Y. Zhang, G. Vives, J. Echeverria, M. Grisolia, G. Rapenne, C. Joachim, and S.-W. Hla. *Controlled clockwise and anticlockwise rotational switching of a molecular motor.* Nat. Nanotechnol. **8**, 46 (2012).

[138] M. Weinelt and F. von Oppen. *Molecular switches at surfaces.* J. Phys. Condens. Matter **24**, 390201 (2012).

[139] B. K. Pathem, S. A. Claridge, Y. B. Zheng, and P. S. Weiss. *Molecular switches and motors on surfaces.* Annu. Rev. Phys. Chem. **64**, 605 (2013).

[140] J. P. Perdew, K. Burke, and M. Ernzerhof. *Generalized gradient approximation made simple.* Phys. Rev. Lett. **77**, 3865 (1996).

[141] V. G. Ruiz, W. Liu, E. Zojer, M. Scheffler, and A. Tkatchenko. *Density-functional theory with screened van der waals interactions for the modeling of hybrid inorganic-organic systems.* Phys. Rev. Lett. **108**, 146103 (2012).

[142] S. J. Clark, M. D. Segall, C. J. Pickard, P. J. Hasnip, M. I. J. Probert, K. Refson, and M. C. Payne. *First principles methods using CASTEP.* Z. Kristallog. - Cryst. Mater. **220**, 567 (2005).

[143] E. McNellis, J. Meyer, A. D. Baghi, and K. Reuter. *Stabilizing a molecular switch at solid surfaces: A density functional theory study of azobenzene on Cu(111), Ag(111), and Au(111).* Phys. Rev. B **80**, 035414 (2009).

[144] A. Vilan, D. Aswal, and D. Cahen. *Large-area, ensemble molecular electronics: Motivation and challenges.* Chem. Rev. **117**, 4248 (2017).

[145] A. B. Zrimsek, N. Chiang, M. Mattei, S. Zaleski, M. O. McAnally, C. T. Chapman, A.-I. Henry, G. C. Schatz, and R. P. Van Duyne. *Single-molecule chemistry with surface- and tip-enhanced raman spectroscopy.* Chem. Rev. **117**, 7583 (2017).

[146] R. J. Maurer, V. G. Ruiz, J. Camarillo-Cisneros, W. Liu, N. Ferri, K. Reuter, and A. Tkatchenko. *Adsorption structures and energetics of molecules on metal surfaces: Bridging experiment and theory.* Prog. Surf. Sci. **91**, 72 (2016).

[147] M. Böhringer, R. Berndt, and W.-D. Schneider. *Transition from three-dimensional to two-dimensional faceting of Ag(110) induced by cu-phthalocyanine.* Phys. Rev. B **55**, 1384 (1997).

[148] M. Hinterstein, X. Torrelles, R. Felici, J. Rius, M. Huang, S. Fabris, H. Fuess, and M. Pedio. *Looking underneath fullerenes on Au(110): Formation of dimples in the substrate.* Phys. Rev. B **77**, 153412 (2008).

[149] W. W. Pai and C.-L. Hsu. *Ordering of an incommensurate molecular layer with adsorbate-induced reconstruction: C_{60}/Ag(100).* Phys. Rev. B **68**, 121403 (2003).

[150] W. W. Pai, H. T. Jeng, C.-M. Cheng, C.-H. Lin, X. Xiao, A. Zhao, X. Zhang, G. Xu, X. Q. Shi, M. A. Van Hove, C.-S. Hsue, and K.-D. Tsuei. *Optimal electron doping of a C_{60} monolayer on Cu(111) via interface reconstruction.* Phys. Rev. Lett. **104**, 036103 (2010).

[151] Y.-C. Xie, L. Tang, and Q. Guo. *Cooperative assembly of magic number C_{60}-Au complexes.* Phys. Rev. Lett. **111**, 186101 (2013).

[152] P. Maksymovych, O. Voznyy, D. B. Dougherty, D. C. Sorescu, and J. T. Yates Jr. *Gold adatom as a key structural component in self-assembled monolayers of organosulfur molecules on Au(111).* Prog. Surf. Sci. **85**, 206 (2010).

[153] P. Maksymovych, D. C. Sorescu, O. Voznyy, and J. T. Yates. *Hybridization of phenylthiolate- and methylthiolate-adatom species at low coverage on the Au(111) surface.* J. Am. Chem. Soc. **135**, 4922 (2013).

[154] L. Giovanelli, A. Savoyant, M. Abel, F. Maccherozzi, Y. Ksari, M. Koudia, R. Hayn, F. Choueikani, E. Otero, P. Ohresser, J.-M. Themlin, S. S. Dhesi, and S. Clair. *Magnetic coupling and single-ion anisotropy in surface-supported mn-based metal-organic networks.* J. Phys. Chem. C **118**, 11738 (2014).

[155] N. Lin, S. Stepanow, F. Vidal, J. V. Barth, and K. Kern. *Manipulating 2D metal-organic networks via ligand control.* Chem. Commun. pp. 1681–1683 (2005).

[156] A. Shchyrba, C. Wäckerlin, J. Nowakowski, S. Nowakowska, J. Björk, S. Fatayer, J. Girovsky, T. Nijs, S. C. Martens, A. Kleibert, M. Stöhr, N. Ballav, T. A. Jung, and L. H. Gade. *Controlling the dimensionality of on-surface coordination polymers via endo- or exoligation.* J. Am. Chem. Soc. **136**, 9355 (2014).

[157] M. Matena, M. Stöhr, T. Riehm, J. Björk, S. Martens, S. Dyer, Matthew, M. Persson, J. Lobo-Checa, K. Müller, M. Enache, H. Wadepohl, J. Zegenhagen, T. A. Jung, and L. H. Gade. *Aggregation and contingent metal/surface reactivity of 1,3,8,10-tetraazaperopyrene (TAPP) on Cu(111).* Chem. Eur. J. **16**(7), 2079 (2010).

[158] M. Matena, J. Björk, M. Wahl, T.-L. Lee, J. Zegenhagen, L. H. Gade, T. A. Jung, M. Persson, and M. Stöhr. *On-surface synthesis of a two-dimensional porous coordination network: Unraveling adsorbate interactions.* Phys. Rev. B **90**, 125408 (2014).

[159] F. Bischoff, Y. He, K. Seufert, D. Stassen, D. Bonifazi, J. V. Barth, and W. Auwärter. *Tailoring large pores of porphyrin networks on Ag(111) by metal-organic coordination.* Chem. Eur. J. **22**, 15298 (2016).

[160] F. Buchner, K. Flechtner, Y. Bai, E. Zillner, I. Kellner, H.-P. Steinrück, H. Marbach, and J. M. Gottfried. *Coordination of iron atoms by tetraphenylporphyrin monolayers and multilayers on Ag(111) and formation of iron-tetraphenylporphyrin.* J. Phys. Chem. C **112**, 15458 (2008).

[161] T. R. Umbach, M. Bernien, C. F. Hermanns, A. Krüger, V. Sessi, I. Fernandez-Torrente, P. Stoll, J. I. Pascual, K. J. Franke, and W. Kuch. *Ferromagnetic coupling of mononuclear Fe centers in a self-assembled metal-organic network on Au(111).* Phys. Rev. Lett. **109**, 267207 (2012).

[162] Q. Fan, C. Wang, Y. Han, J. Zhu, J. Kuttner, G. Hilt, and J. M. Gottfried. *Surface-assisted formation, assembly, and dynamics of planar organometallic macrocycles and zigzag shaped polymer chains with C-Cu-C bonds.* ACS Nano **8**, 709 (2014).

[163] A. Wander, M. A. Van Hove, and G. A. Somorjai. *Molecule-induced displacive reconstruction in a substrate surface: Ethylidyne adsorbed on Rh(111) studied by low-energy-electron diffraction.* Phys. Rev. Lett. **67**, 626 (1991).

[164] V. Humblot, A. Vallé, A. Naitabdi, F. Tielens, and C.-M. Pradier. *Drastic Au(111) surface reconstruction upon insulin growth factor tripeptide adsorption.* J. Am. Chem. Soc. **134**, 6579 (2012).

[165] P. Guaino, D. Carty, G. Hughes, O. McDonald, and A. A. Cafolla. *Long-range order in a multilayer organic film templated by a molecular-induced surface reconstruction: Pentacene on Au(110).* Appl. Phys. Lett. **85**, 2777 (2004).

[166] D. J. Lavrich, S. M. Wetterer, S. L. Bernasek, and G. Scoles. *Physisorption and chemisorption of alkanethiols and alkyl sulfides on Au(111).* J. Phys. Chem. B **102**, 3456 (1998).

[167] S. Sek, J. Breczko, M. E. Plonska-Brzezinska, A. Z. Wilczewska, and L. Echegoyen. *STM-based molecular junction of carbon nano-onion.* ChemPhysChem **14**, 96 (2012).

[168] Y. Xu, M. D. Smith, J. A. Krause, and L. S. Shimizu. *Control of the intramolecular [2+2] photocycloaddition in a bis-stilbene macrocycle.* J. Org. Chem. **74**, 4874 (2009).

[169] W. A. Velema, M. van der Toorn, W. Szymanski, and B. L. Feringa. *Design, synthesis, and inhibitory activity of potent, photoswitchable mast cell activation inhibitors.* J. Med. Chem. **56**, 4456 (2013).

[170] G. Kresse and J. Furthmüller. *Efficiency of ab-initio total energy calculations for metals and semiconductors using a plane-wave basis set.* Comput. Mater. Sci. **6**, 15 (1996).

[171] A. Tkatchenko and M. Scheffler. *Accurate molecular van der waals interactions from ground-state electron density and free-atom reference data.* Phys. Rev. Lett. **102**, 073005 (2009).

[172] M.-L. Bocquet, H. Lesnard, S. Monturet, and N. Lorente. *Theory of Elastic and Inelastic Electron Tunneling*, chap. 11, pp. 199–219 (Wiley-VCH, Weinheim, Germany, 2009).

[173] P. C. Hess. *NDI-Phanes with Tailor-Made Optical Properties.* Ph.D. thesis, Universität Basel (2015).

[174] L. M. Wesoloski, A. Z. Stieg, M. Kunitake, S. C. Dultz, and J. K. Gimzewski. *Observations of image contrast and dimerization of decacyclene by low temperature scanning tunneling microscopy.* J. Chem. Phys. **127**, 174703 (2007).

[175] F. Calleja, A. Arnau, J. J. Hinarejos, A. L. Vázquez de Parga, W. A. Hofer, P. M. Echenique, and R. Miranda. *Contrast reversal and shape changes of atomic adsorbates measured with scanning tunneling microscopy.* Phys. Rev. Lett. **92**, 206101 (2004).

[176] N. L. Schneider, F. Matino, G. Schull, S. Gabutti, M. Mayor, and R. Berndt. *Light emission from a double-decker molecule on a metal surface.* Phys. Rev. B **84**, 153403 (2011).

[177] V. I. Minkin. *Glosaary of terms used in theoretical organic chemistry.* Pure Appl. Chem. **71**, 1919 (1999).

[178] S. J. Loeb and B. de Groot. *Encapsulation of silver(I) by the crown thioether ligand 1,3,6,9,11,14-hexathiacyclohexadecane (16S6). synthesis and structure of [Ag(16S6)][ClO_4].* Inorg. Chem. **30**, 3103 (1991).

[179] A. J. Blake, R. O. Gould, A. J. Holder, T. I. Hide, and M. Schröder. *Silver thioether chemistry: Synthesis, X-ray crystal structure and redox properties of [Ag([18]aneS_6)]+ ([18]aneS_6 = 1,4,7,10,13,16-hexathiacyclooctadecane).* Polyhedron **8**, 513 (1989).

[180] R. Alberto, W. Nef, A. Smith, T. A. Kaden, M. Neuburger, M. Zehnder, A. Frey, U. Abram, and P. A. Schubiger. *Silver(I) complexes of the derivatized crown thioether ligands 3,6,9,12,15,18-hexathianonadecanol and 3,6,9,13,16,19-hexathiaicosanol. determination of stability constants and the crystal structures of [Ag(19-aneS_6-OH)][CF_3SO_3] and [Ag(20-aneS_6-OH)][BF_4].* Inorg. Chem. **35**, 3420 (1996).

[181] R. B. L. Limot, J. Kröger, A. Garcia-Lekue, and W. A. Hofer. *Atom transfer and single-adatom contacts.* Phys. Rev. Lett. **94**, 126102 (2005).

[182] R. Stomp, Y. Miyahara, S. Schaer, Q. Sun, H. Guo, P. Grutter, S. Studenikin, P. Poole, and A. Sachrajda. *Detection of single-electron charging in an individual InAs quantum dot by noncontact atomic-force microscopy.* Phys. Rev. Lett. **94**, 056802 (2005).

[183] T. König, G. H. Simon, H.-P. Rust, G. Pacchioni, M. Heyde, and H.-J. Freund. *Measuring the charge state of point defects on MgO/Ag(001).* J. Am. Chem. Soc. **131**, 17544 (2009).

[184] R. Bennewitz, A. S. Foster, L. N. Kantorovich, M. Bammerlin, C. Loppacher, S. Schär, M. Guggisberg, E. Meyer, and A. L. Shluger. *Atomically resolved edges and kinks of NaCl islands on Cu(111): Experiment and theory.* Phys. Rev. B **62**, 2074 (2000).

[185] R. Bennewitz, O. Pfeiffer, S. Schär, V. Barwich, E. Meyer, and L. Kantorovich. *Atomic corrugation in nc-AFM of alkali halides.* Appl. Surf. Sci. **188**, 232 (2002).

[186] C. Barth, A. S. Foster, M. Reichling, and A. L. Shluger. *Contrast formation in atomic resolution scanning force microscopy on CaF2(111): experiment and theory.* J. Phys. Condens. Matter **13**, 2061 (2001).

[187] R. Hoffmann, L. N. Kantorovich, A. Baratoff, H. J. Hug, and H.-J. Güntherodt. *Sublattice identification in scanning force microscopy on alkali halide surfaces.* Phys. Rev. Lett. **92**, 146103 (2004).

[188] F. J. Giessibl. *Theory for an electrostatic imaging mechanism allowing atomic resolution of ionic crystals by atomic force microscopy.* Pys. Rev. B **45**, 13815 (1992).

[189] F. Bocquet, L. Nony, and C. Loppacher. *Polarization effects in noncontact atomic force microscopy: A key to model the tip-sample interaction above charged adatoms.* Phys. Rev. B **83**, 035411 (2011).

[190] A. Sadeghi, A. Baratoff, and S. Goedecker. *Electrostatic interactions with dielectric samples in scanning probe microscopies.* Phys. Rev. B **88**, 035436 (2013).

[191] M. Turner, O. P. H. Vaughan, G. Kyriakou, D. J. Watson, L. J. Scherer, A. C. Papageorgiou, J. K. M. Sanders, and R. M. Lambert. *Deprotection, tethering, and activation of a one-legged metalloporphyrin on a chemically active metal surface: NEXAFS, synchrotron XPS, and STM study of [SAc]P-Mn(III)Cl on Ag(100).* J. Am. Chem. Soc. **131**, 14913 (2009).

[192] D. van Vörden, M. Lange, J. Schaffert, M. C. Cottin, M. Schmuck, R. Robles, H. Wende, C. A. Bobisch, and R. Möller. *Surface-induced dechlorination of FeOEP-cl on Cu(111).* ChemPhysChem **14**, 3472 (2013).

[193] N. V. Smith, C. T. Chen, and M. Weinert. *Distance of the image plane from metal surfaces.* Phys. Rev. B **40**, 7565 (1989).

[194] E. Chulkov, V. Silkin, and P. Echenique. *Image potential states on metal surfaces: binding energies and wave functions.* Surf. Sci. **437**, 330 (1999).

[195] N. M. Caffrey, K. Buchmann, N. Hauptmann, C. Lazo, P. Ferriani, S. Heinze, and R. Berndt. *Competing forces during contact formation between a tip and a single molecule.* Nano Lett. **15**, 5156 (2015).

[196] R. Smoluchowski. *Anisotropy of the electronic work function of metals.* Phys. Rev. **60**, 661 (1941).

[197] D. Z. Gao, J. Grenz, M. B. Watkins, F. F. Canova, A. Schwarz, R. Wiesendanger, and A. L. Shluger. *Using metallic noncontact atomic force microscope tips for imaging insulators and polar molecules: Tip characterization and imaging mechanisms.* ACS Nano **8**, 5339 (2014).

[198] A. Schwarz, A. Köhler, J. Grenz, and R. Wiesendanger. *Detecting the dipole moment of a single carbon monoxide molecule.* Appl. Phys. Lett. **105**, 011606 (2014).

[199] B. B. Laud. *Electromagnetics* (New Age International, 1987).

[200] F. Cuadros, I. Cachadiña, and W. Ahumada. *Determination of lennard-jones interaction parameters using a new procedure.* Molecular Engineering **6**, 319 (1996).

[201] N. Hauptmann, L. Groß, K. Buchmann, K. Scheil, C. Schütt, F. L. Otte, R. Herges, C. Herrmann, and R. Berndt. *High-conductance surface-anchoring of a mechanically flexible platform-based porphyrin complex.* New J. Phys. **17**, 013012 (2015).

[202] T. Jasper-Tönnies, A. Garcia-Lekue, T. Frederiksen, S. Ulrich, R. Herges, and R. Berndt. *Conductance of a freestanding conjugated molecular wire.* Phys. Rev. Lett. **119**, 066801 (2017).

[203] Z. Sun, M. P. Boneschanscher, I. Swart, D. Vanmaekelbergh, and P. Liljeroth. *Quantitative atomic force microscopy with carbon monoxide terminated tips.* Phys. Rev. Lett. **106**, 046104 (2011).

[204] L. Gross, F. Mohn, N. Moll, B. Schuler, A. Criado, E. Guitian, D. Pena, A. Gourdon, and G. Meyer. *Bond-order discrimination by atomic force microscopy.* Science **337**, 1326 (2012).

[205] G. Henkelman and H. Jónsson. *Improved tangent estimate in the nudged elastic band method for finding minimum energy paths and saddle points.* J. Chem. Phys. **113**, 9978 (2000).

[206] R. Maurer. *First-Principles Description of the Isomerization Dynamics of Surface-Adsorbed Molecular Switches.* Ph.D. thesis, Technische Universität München (2014).

[207] R. J. Maurer and K. Reuter. *Excited-state potential-energy surfaces of metal-adsorbed organic molecules from linear expansion Δ-self-consistent field density-functional theory (ΔSCF-DFT).* J. Chem. Phys. **139**, 014708 (2013).

[208] G. Kresse and D. Joubert. *From ultrasoft pseudopotentials to the projector augmented-wave method.* Phys. Rev. B **59**, 1758 (1999).

[209] B. Wortmann, D. v. Vörden, P. Graf, R. Robles, P. Abufager, N. Lorente, C. A. Bobisch, and R. Möller. *Reversible 2D phase transition driven by an electric field: Visualization and control on the atomic scale.* Nano Lett. **16**, 528 (2016).

[210] F. Chaumeton, R. Robles, M. Pruneda, N. Lorente, B. Eydoux, X. Bouju, S. Gauthier, and D. Martrou. *Noncontact atomic force microscopy and density functional theory studies of the* (2×2) *reconstructions of the polar aln(0001) surface.* Phys. Rev. B **94**, 165305 (2016).

[211] M. J. Frisch, G. W. Trucks, H. B. Schlegel, G. E. Scuseria, M. A. Robb, J. R. Cheeseman, G. Scalmani, V. Barone, B. Mennucci, and G. A. e. a. Petersson. *Gaussian 09 Revision D.01* (2013). Gaussian Inc. Wallingford CT.

[212] J. Tirado-Rives and W. L. Jorgensen. *Performance of B3LYP density functional methods for a large set of organic molecules.* J. Chem. Theory Comput. **4**, 297 (2008).

[213] S. Grimme, S. Ehrlich, and L. Goerigk. *Effect of the damping function in dispersion corrected density functional theory.* J. Comput. Chem. **32**, 1456 (2011).

[214] G. V. Nazin, X. H. Qiu, and W. Ho. *Charging and interaction of individual impurities in a monolayer organic crystal.* Phys. Rev. Lett. **95**, 166103 (2005).

[215] G. V. Nazin, X. H. Qiu, and W. Ho. *Vibrational spectroscopy of individual doping centers in a monolayer organic crystal.* J. Chem. Phys. **122**, 181105 (2005).

[216] G. V. Nazin, S. W. Wu, and W. Ho. *Tunneling rates in electron transport through double-barrier molecular junctions in a scanning tunneling microscope.* P. Natl. Acad. Sci. U.S.A. **102**, 8832 (2005).

[217] I. Fernández-Torrente, D. Kreikemeyer-Lorenzo, A. Stróżecka, K. J. Franke, and J. I. Pascual. *Gating the charge state of single molecules by local electric fields.* Phys. Rev. Lett. **108**, 036801 (2012).

[218] F. Marczinowski, J. Wiebe, F. Meier, K. Hashimoto, and R. Wiesendanger. *Effect of charge manipulation on scanning tunneling spectra of single mn acceptors in InAs.* Phys. Rev. B **77**, 115318 (2008).

[219] K. Teichmann, M. Wenderoth, S. Loth, R. G. Ulbrich, J. K. Garleff, A. P. Wijnheijmer, and P. M. Koenraad. *Controlled charge switching on a single donor with a scanning tunneling microscope.* Phys. Rev. Lett. **101**, 076103 (2008).

[220] A. P. Wijnheijmer, J. K. Garleff, K. Teichmann, M. Wenderoth, S. Loth, and P. M. Koenraad. *Single Si dopants in GaAs studied by scanning tunneling microscopy and spectroscopy.* Phys. Rev. B **84**, 125310 (2011).

[221] H. Zheng, J. Kröger, and R. Berndt. *Spectroscopy of single donors at ZnO(0001) surfaces.* Phys. Rev. Lett. **108**, 076801 (2012).

[222] N. A. Pradhan, N. Liu, C. Silien, and W. Ho. *Atomic scale conductance induced by single impurity charging.* Phys. Rev. Lett. **94**, 076801 (2005).

[223] G. Mikaelian, N. Ogawa, X. W. Tu, and W. Ho. *Atomic scale control of single molecule charging.* J. Chem. Phys. **124**, 131101 (2006).

[224] N. Hauptmann, C. Hamann, H. Tang, and R. Berndt. *Switching and charging of a ruthenium dye on ag(111).* Phys. Chem. Chem. Phys. **15**, 10326 (2013).

[225] G. Kresse and J. Hafner. *Ab initio molecular dynamics for liquid metals.* Phys. Rev. B **47**, 558 (1993).

[226] S. L. Dudarev, G. A. Botton, S. Y. Savrasov, C. J. Humphreys, and A. P. Sutton. *Electron-energy-loss spectra and the structural stability of nickel oxide: An LSDA+U study.* Phys. Rev. B **57**, 1505 (1998).

[227] P. M. Panchmatia, B. Sanyal, and P. M. Oppeneer. *GGA+U modeling of structural, electronic, and magnetic properties of iron porphyrin-type molecules.* Chem. Phys. **343**, 47 (2008).

[228] P. E. Blöchl. *Projector augmented-wave method.* Phys. Rev. B **50**, 17953 (1994).

List of Abbreviations

AB	azobenzene
AFM	atomic force microscope / microscopy
CC	column chromatography
DFT	density functional theory
DMF	*N*,*N*-dimethyl-formamide
DMI	1,3-dimethyl-2-imidazolidinone
FCC	face-centered cubic
FeTPP	iron tetraphenylporphyrine
FeTPPCl	iron tetraphenylporphyrine chloride
FM-AFM	dynamic non-contact atomic force microscopy with frequency modulation
GGA	generalized gradient approximation
GPC	subsequent gel permeation chromatography
HCP	hexagonal close-packed
HOMO	highest occupied molecular orbital
KPFM	kelvin probe force microscopy
LDOS	Local Density of States
LUMO	lowest unoccupied molecular orbital
MO	molecular orbital
NDI	naphthalene diimide
NEB	nudged elastic band
NTCDI	naphthalenetetracarboxylic diimide
PAW	projector-augmented wave
PBE	Perdew-Burke-Ernzerhof
PDOS	projected density of states
PLL	phase locked loop
STM	scanning tunneling microscope / microscopy
STS	scanning tunneling spectroscopy
TPAPA	tris-[4-(phenylazo)-phenyl]-amine
UHV	ultra-high vacuum
VASP	Vienna Ab initio Simulation Package
vdW	van der Waals

Acknowledgments

I would never have got to the point of submitting this thesis without the help of many people. I would like to express my sincere gratitude to:

- Prof. Dr. Richard Berndt, for giving me the chance to work in his group, his many tips and fruitful discussions.
- Prof. Dr. Marcel Mayor, Dr. Pascal Hess, Prof. Dr. Friedrich Temps, Dr. Julia Bahrenburg for providing the molecules I have used during my measurements.
- Prof. Dr. Nicolás Lorente, Prof. Dr. Marie-Laure Bocquet, Prof. Dr. Karsten Reuter, Dr. Reinhard Maurer, Prof. Dr. Pavel Jelinek and Dr. Martin Ondráček for their extraordinary theoretical work.
- Prof. Dr. Rainer Herges and Dr. Thiruvancheril Gopakumar for helpful discussions.
- Dr. Christian Feiler for answering all my chemistry questions and for always cheering me up.
- Dr. Nadine Hauptmann for teaching me a lot about STM/AFM and for always helping me when I had questions.
- Dr. Manuel Gruber for working out the force model on FeTPPCl and encouraging me when I was disheartened.
- I dedicate a special thanks to all former and present group members in the ESI lab, especially Manuel, Nadine, Kristof Buchmann, Thomas Knaak, Alexander Köbke and Dr. Christian Hamann. It has been a great pleasure to work with you.
- Dr. Johannes Schöneberg for the path we walked together.
- My desk neighbor Torben Jasper-Tönnies for many fruitful discussions and an always friendly working atmosphere in our office.
- Manuel, Christian, Torben, Martin Scheil and Gesche Franzén for proofreading.
- Dr. Thomas Jürgens, Rene Woltmann, Jörg Neubauer, Hans-Joachim Neumann, Joost Jakobs for helping to keep the ESI running.
- Monika Seeger for always cheerful and competent help with the day to day paperwork.

- All my other colleagues and former coworkers for the very nice working atmosphere in the group and the many discussions in the coffee room which I really enjoyed.
- The financial support from Sonderforschungsbereich 677 is gratefully acknowledged.

To all others, who supported me outside of university, I am deeply grateful. I want to express my gratitude to all my friends. In particular, Anna, Melanie, Karim, Gesa and Christian. Our weekly 'Spieleabend' meant a lot to me. I am especially thankful to Lars for always being there. I am wholeheartedly thankful also to my family. Without their constant support and love, none of the described work would have been possible.

List of Publications

- N. Hauptmann, **K. Scheil**, T.G. Gopakumar, F.L. Otte, C. Schütt, R. Herges and R. Berndt,
  Surface Control of Alkyl Chain Conformations and 2D Chiral Amplification
  J. Am. Chem. Soc. **135**, 8814 (2013)

- N. Hauptmann, L. Groß, K. Buchmann, **K. Scheil**, C. Schütt, F.L. Otte, R. Herges, C. Herrmann and R. Berndt,
  High-Conductance Surface-Anchoring of a Mechanically Flexible Platform-Based Porphyrin Complex
  New J. Phys. **17**, 013012 (2015).

- **K. Scheil**, T.G. Gopakumar, J. Bahrenburg, F. Temps, R.J. Maurer, K. Reuter and R. Berndt,
  Switching of an Azobenzene-Tripod Molecule on Ag(111),
  J. Phys. Chem. Lett. **7**, 2080 (2016)

- **K. Scheil**, N. Lorente, M.-L. Bocquet, P.C. Hess, M. Mayor and R. Berndt,
  Adatom Coadsorption with Three-Dimensional Cyclophanes on Ag(111),
  J. Phys. Chem. C. **121**, 25303 (2017)